



Universität Hamburg  
DER FORSCHUNG | DER LEHRE | DER BILDUNG



CHyN  
Centre for Hybrid Nanostructures

**The Application of Polyelectrolyte Capsule in Sensor Development and  
Discussion of Nanoflare for Live Cell Message RNA Imaging  
Dissertation**

zur Erlangung des Doktorgrades

der Naturwissenschaften

(Dr.rer.nat)

dem

Fachbereich Chemie

der Universität Hamburg

vorgelegt von

**Yaofeng Zhou**

aus

Jiangxi province, China

Hamburg, 2023

The presented work conducted under the supervision under the supervision  
of Prof. Wolfgang J. Parak and Dr. Neus Feliu Torres at the center of Hybrid  
nanostructures (CHyN) of the Universität Hamburg, Germany (from  
November 2019 to March 2023)

Thesis Committee: Prof. Dr. Wolfgang J. Parak  
Prof. Dr. Neus Feliu Torres

Evaluation Committee: Prof. Dr. Wolfgang J. Parak  
Prof. Dr. Wolfgang Maison  
Prof. Dr. Tobias Beck

Disputation date: 17-03-2023



## List of publications

1. Semiconductor Nanoplatelets as Ultra-Bright Fluorophores for Two-Photon Absorption Cell Imaging. Gan Chen, Henry Halim, Huijie Yan, **Yaofeng Zhou**, Dingcheng Zhu, Wolfgang J. Parak, Andreas Riedinger,\* and Neus Feliu\*. J. Phys. Chem. C 2022, 126, 5658–5664.
2. Polyelectrolyte Capsule-Accelerated Enzyme Immobilization for the Establishment of an Enzyme-Based immunoassay. Yanna Shao, **Yaofeng Zhou (Co-first author)**, Nuo Chen, Wenxing Xu, Huan Zhou, Weihua Lai, Xiaolin Huang, Xinran Xiang, Qinghua Ye, Jumei Zhang, Juan Wang, Wolfgang J. Parak, Qingping Wu, Yu Ding\*. Submitted. ACS Applied Materials & Interfaces.
3. Viruses and chloroquine - recapitulating basic facts regarding the particulate nature of viruses. Gan Chen, Dingcheng Zhu, **Yaofeng Zhou**, Timothy K. Soh, Neus Feliu, Wolfgang J. Parak\*. ACS Nanoscience Au, in revision
5. Using Nanoflare for Live Cell Message RNA Imaging, Inside and Outside of Lysosome. **Yaofeng Zhou**, Dingcheng Zhu, Antonios G. Kanaras\*, Wolfgang J. Parak\*, Neus Feliu\*. In preparation
6. Nanotransducer-evoked revolution of cell Ca<sup>2+</sup> signaling manipulation. **Yaofeng Zhou**, Zherui Zhang, Haoye Huang, Sarodi Jonak, Dingcheng Zhu\*, Junqiu Liu\*, Wolfgang J. Parak\*, Neus Feliu. In preparation.
7. Design of Disintegrable Nano-assemblies to Release Multiple Small-Sized Nanoparticles. Dingcheng Zhu; Huijie Yan; **Yaofeng Zhou**; Leroy M. Nack; Junqiu Liu, Wolfgang J. Parak\*. Advanced Drug Delivery Reviews, submitted.

## Content

61	List of abbreviations .....	1
62	1. Submicron Polyelectrolyte Capsule-enhanced Enzyme Immobilization for	
63	Improving Enzyme-based Immunoassays .....	7
64	1.1 Introduction.....	7
65	1.2 Experimental section.....	11
66	1.2.1 Materials.....	11
67	1.2.2 Instrument and characterization .....	11
68	1.2.3 The synthesis of 500 nm CaCO <sub>3</sub> NPs and coprecipitation method.....	12
69	1.2.4 The preparation of SPCs .....	12
70	1.2.5 Measurement of the catalytic kinetics of soluble and PC-immobilized	
71	enzymes.....	13
72	1.2.6 Preparation of FITC-labeled HRP and RhB-labeled GOx .....	13
73	1.2.7 Biotin-labeling of detection antibodies .....	13
74	1.2.8 SA-labeled HRP@SPCs.....	14
75	1.2.9 Detection procedure of the HRP@SPCs-based ELISA .....	14
76	1.2.10 Bacteria culture .....	14
77	1.3 Results and discussion .....	16
78	1.3.1 Synthesis and characterization of enzyme-loaded SPCs.....	16
79	1.3.2 Catalytic kinetics of soluble and SPC-packed HRP.....	20
80	1.3.3 Protection performance of SPCs to HRP .....	23
81	1.3.4 SPCs-based enzyme cascade catalysis .....	24
82	1.3.5 Development of HRP@SPC-based ELISA for ultrasensitive detection of <i>E.</i>	
83	<i>coli</i> O157:H7 .....	28
84	1.4 Conclusion .....	33
85	2. Using Nanoflare for Live Cell Message RNA Imaging, Difference Between Inside	
86	and Outside of Endo/lysosome .....	34
87	2.1 Introduction.....	34
88	2.2 Results and discussion .....	37
89	2.2.1 Cell culture .....	37
90	2.2.2 Exposing nanoflare to HeLa cells .....	37
91	2.2.3 Injecting nanoflare into HeLa cells .....	37
92		

93	2.2.4 Imaging nanoflare exposed/injected HeLa cells .....	38
94	2.2.5 Protocol for colocalization .....	38
95	2.2.6 The measurement protocol for fluorescent intensities of nanoflare	
96	exposed/injected cells.....	39
97	2.3 Results and discussion .....	40
98	2.3.1 Proof of concept .....	40
99	2.3.2 Colocalization.....	41
100	2.3.2 Comparison of nanoflare-based mRNA imaging by injection and incubation	47
101	2.3.3 The amount of nanoflare in per cell by endocytosis .....	56
102	2.3.4 Amount of nanoflare in HeLa cells by injection .....	59
103	Method 1 .....	59
104	Method 2 .....	61
105	2.3.5 Calcein injection calibration curves .....	62
106	2.4 Conclusion .....	67
107	3. The development of Cl <sup>-</sup> microsensor for investigating proton sponge effect.....	69
108	3.1 Introduction.....	69
109	3.2 Experimental section.....	72
110	3.2.1 Materials.....	72
111	3.2.1 Preparation of PCQ .....	72
112	3.2.2 Preparation of PCQ-conjugated BSA and Cy5-conjugated BSA .....	73
113	3.2.3 Preparation of PCQ@BSA and Cy5@BSA co-loaded PCs.....	73
114	3.3 Results and discussion .....	75
115	3.3.1 Synthesis and characterization of PCQ .....	75
116	3.3.2 Synthesis and characterization of PCQ@BSA.....	76
117	3.3.3 Cl <sup>-</sup> sensibility examination of Cy5 .....	77
118	3.3.4 Preparation and characterization of PCQ@BSA and Cy5@BSA co-loaded	
119	PCs .....	78
120	3.3.5 Fluorescent properties of PSS and PAH .....	79
121	3.4 Conclusion .....	81
122	Reference .....	82
123	List of hazardous substances.....	90
124	Acknowledgements.....	96

125	Declaration on Oath .....	97
126		

**List of abbreviations**

<b>Name</b>	<b>Abbreviations</b>
Polyelectrolyte capsule	PC
Submicron polyelectrolyte capsule	SPC
Enzyme-linked immunosorbent assay	ELISA
<i>Escherichia coli</i> O157:H7	<i>E. coli</i> O157:H7
Layer by layer	LbL
Catalase	CAT
Horse radish peroxidase	HRP
Glucose oxidase	GOx
Nanoparticles	NPs
Gold nanoparticles	AuNPs
Rhodamine B	RhB
Fluorescein isothiocyanate	FITC
Streptavidin	SA
3,3',5,5'-tetramethylbenzidine	TMB
Phosphate buffer	PB
Phosphate buffer saline	PBS
20% Tween phosphate buffer saline	PBST
Laser scanning confocal microscope	LSM
Dynamic light scattering	DLS
Transmission electron microscopy	TEM
Scanning electron microscope	SEM
Sodium acetate	NaAc
Bovine serum albumin	BSA
Wheat germ agglutinin	WGA



Dulbecco's modified eagle medium	DMEM
Michaelis constant	$K_m$
Maximal rate	$V_{max}$
Turnover number	$K_{cat}$
Inductively coupled plasma mass spectrometry	ICP-MS
Cyanine 3	Cy3
Cyanine 5	Cy5
Excitation	$\lambda_{ex}$
Emission	$\lambda_{em}$
6-phenyl-N-(6-carboxyhexyl) quinolinium	PCQ

128

129

## Abstract

In the thesis, three projects are presented. The first one is the evaluation of submicron polyelectrolyte capsule (SPC, 500 nm) for enzyme immobilization. The influences of SPCs encapsulation on enzyme catalytic kinetics and stability were tested. The results indicated that SPCs encapsulation affected the affinities of enzymes and substrates but significantly enhanced their catalytic activity. Stability test indicates that SPCs-encapsulated horseradish peroxidase (HRP) exhibits ultrahigh resistance to external harsh conditions and has longer storage life than soluble HRP. In addition, SPCs encapsulation could accelerate the cascade reaction efficiency of HRP and glucose oxidase. Owing to SPCs could enhance catalytic activity of loaded enzyme, the HRP-loaded SPCs were employed to establish an amplified ELISA for the detection of *Escherichia coli* O157:H7. The detection sensitivity of SPCs-improved ELISA was found to be 280 times greater than that of conventional HRP-based ELISA.

Nanoflare, a gold nanoparticle (AuNP)-based fluorescently nanoprobe, fabricated by modifying DNA recognition strand on AuNP then hybridizing DNA flare strand. For single-cell level mRNA detection, the hybridization of the mRNA and the DNA recognition strand is used to displace the flare strand away from the AuNP to release fluorescent signal. Up to now, nanoflare has been broadly reported to detect mRNA in live cells by direct incubating with cells. However, a misgiving has been proposed recently because the internalized nanoflare by cell endocytosis should be placed at endo/lysosome. This means that nanoflare could not image mRNA in cytoplasm when there has no endosomal escape strategy participation. Herein, we used microinjection to direct inject nanoflare to cytoplasm thereby avoiding endo/lysosome encapsulation. The mRNA imaging results of endocytosed and injected nanoflare were systematically evaluated. The colocalization results showed that most of the detection signal released from injected nanoflare aggregated at nucleus, inversely, endocytosed nanoflare-released detection signal could not diffuse into cell nucleus. The fluorescent intensity analysis suggested that injected nanoflare-liberated detection signal is slightly stronger than endocytosed nanoflare. The analysis of control nanoflare (another nanoflare that can not work in HeLa cells) showed that control nanoflare could not liberate detection signal whether internalization by injection or endocytosis. The internalization amounts of nanoflare were measured. The endocytosed nanoflare is 100-times higher than injected nanoflare. On the basis of these results, we assumed that nanoflare could image mRNA by endocytosis, whereas the working efficiency is very low because of the endo/lysosome encapsulation.

Cationic polymers, such as polyethyleneimine (PEI), have been widely used for enhancing gene transfection and drug delivery through reinforcing endosomal escape under the support of proton sponger effect. Recently, increased works have reported that cationic polymers-enhanced gene transfection and drug delivery cannot be explained by the proton sponge effect. This increased the disputations for the proton sponge effect and has led to the exploration of how cationic polymers to enhance drug delivery and gene transfection efficiency. In the acidification of the endosome, cationic polymers with a buffering property to inhibit the acidizing, and triggering continue pumping protons and  $\text{Cl}^-$ . The increased osmotic pressure causes the swell and lysis of endo/lysosome. Therefore, dynamic monitoring  $\text{Cl}^-$  concentration in endo/lysosome is a promising strategy to verify the proton sponge effect. We here sought to prepare a microsensor for extracellular and intracellular  $\text{Cl}^-$  sensing. The microsensor was formed by loading 6-phenyl-N-(6-carboxyhexyl) quinolinium-conjugated bovine serum albumin (PCQ@BSA) into polyelectrolyte capsule (PC). In this sensor,

173 PCQ@BSA is the fluorescence probe for Cl<sup>-</sup> detection; PCs can efficiently load PCQ@BSA and  
174 PEI while allowing Cl<sup>-</sup> to access PCQ@BSA under low-barrier condition. We synthesized and  
175 characterized PCQ and PCQ@BSA. We also prepared PCQ@BSA and Cy5@BSA co-loaded PCs.  
176 However, we finally found that the emissions of PCQ@BSA and PCs have overlap, which intensely  
177 disturbs the sensing.  
178

## Zusammenfassung

In dieser Thesis werden drei Projekte präsentiert. Das erste Projekt ist die Evaluation von Submikron Polyelektrolyte-Kapseln (SPC, 500 nm) für Enzym Immobilisierung. Die Einflüsse der SPC-Einkapselung auf die katalytische Enzym Kinetik and Stabilität wurden getestet. Die Ergebnisse deuteten darauf hin, dass die SPC-Einkapselung die Affinität von Enzym und Substrat beeinflusste, aber ihre katalytische Aktivität signifikant stieg. Stabilitätstests demonstrieren, dass von SPCs eingekapselte Meerrettichperoxidase (HRP) eine extrem hohe Resistenz gegen äußere Einflüsse zeigt und eine höhere Lebenszeit als lösliche HRP hat. Außerdem konnte die SPC-Einkapselung die Kaskaden-Reaktionseffizienz von HRP und Glucose Oxidase erhöhen. Da SPCs die katalytischen Aktivitäten eingekapselter Enzyme erhöhen konnte, wurden mit HRP beladene SPCs genutzt, um eine verstärkte ELISA für die Detektion von *Escherichia coli* O157:H7 zu etablieren. Die Detektionssensitivität der SPC-verbesserten ELISA war 280-fach besser als die der konventionellen HRP basierten ELISA.

Nanoflare, ein Gold Nanopartikel (AuNP) basierte, fluoreszierende Nanosonde, wird hergestellt, indem DNA-Erkennungsstränge auf die AuNP modifiziert werden, und anschließend DNA Flare Stränge hybridisiert werden. Für die mRNA-Detektion auf Einzelzellebene, wird die Hybridisierung der mRNA und des DNA-Erkennungsstranges dazu genutzt, den Flare Strang von dem AuNP zu verdrängen um ein Fluoreszenz Signal auszulösen. Bis heute wurde umfassend berichtet, dass Nanoflares, über direkte Inkubation mit Zellen, die mRNA in lebenden Zellen abbilden können. Allerdings wurden kürzlich Bedenken gemeldet, da die über Endozytose internalisierten Nanopartikel in Endo-/Lysosomen platziert sein sollten. Das bedeutet, dass Nanoflares kein mRNA im Cytoplasma abbilden könnten, solange kein Endosomales Entkommen stattfindet. In diesem Projekt haben wir Mikroinjektion genutzt, um Nanoflares direkt in das Cytoplasma zu injizieren und eine Endo/Lysosomale Einkapselung zu umgehen. Die mRNA-Abbildungsergebnisse vom endozytisierten und injizierten Nanoflares wurden systematisch evaluiert. Die Kollokalisierungs-Ergebnisse haben gezeigt, dass ein Großteil des Erkennungssignal der injizierten Nanoflares am Nukleus aggregiert waren, während das Erkennungssignal der endozytisierten Nanoflares sich nicht in den Zellkern ausbreiten konnte. Die Fluoreszenzintensitätsanalyse deutet darauf hin, dass das von dem injizierten Nanoflares freigesetztes Erkennungssignal etwas stärker ist als das von den endozytisierten Nanoflares. Die Analyse eines Kontroll-Nanoflares (ein anderes Nanoflare, welches nicht in HeLa Zellen funktioniert) zeigte, dass die Kontroll-Nanoflares weder nach Aufnahme durch Injektion noch nach Aufnahme durch Endozytose ein Erkennungssignal freisetzen konnten. Die Internalisierungsmenge der Nanoflares wurden gemessen. Die Aufnahmemenge von endozytisierten Nanoflares ist 100-fach größer als die der injizierten Nanoflares. Auf der Basis dieser Ergebnisse, haben wir angenommen, dass endozytisiertes Nanoflare mRNA Abbilden kann, wobei die Arbeitseffizienz aufgrund der

Endo-/Lysosomalen Einkapselung sehr niedrig ist. Zur Verbesserung der Gentransfektion und drug delivery, werden vielfach kationische Polymere wie Polyethylenimin genutzt, die mit Unterstützung des Protonenschwammeffektes ein endosomales Entkommen verstärken. In letzter Zeit haben zunehmend Arbeiten berichtet, dass die durch kationische Polymere verbesserte Gentransfektion und drug delivery nicht durch den Protonenschwammeffekt erklärt werden können. Dies hat die Disputationen um den Protonenschwammeffekt verstärkt und zu der Erforschung, wie

222 kationische Polymere die Gentransfektion- und drug delivery Effizienz erhöhen, geführt. Bei der  
223 Säurebildung in den Endosomen, können kationische Polymere mit Puffer Eigenschaften, die  
224 Ansäuerung verhindern und ein kontinuierliches Reinpumpen von Protonen und  $\text{Cl}^-$  hervorrufen.  
225 Der erhöhte Osmotische Druck verursacht das Anschwellen und die Lysis der Endo-/Lysosomen.  
226 Deswegen ist das dynamische Überwachen der  $\text{Cl}^-$  Konzentration eine erfolgsversprechende  
227 Strategie, um den Protonenschwammeffekt zu verifizieren. Hier haben wir angestrebt einen  
228 Mikrosensor für Intra- und Extrazelluläres  $\text{Cl}^-$  Messungen zu präparieren. Der Mikrosensor wurde  
229 gestaltet indem an Bovin Serum Albumin konjugiertes Phenyl-N-(6-carboxyhexyl) chinolinium  
230 (PCQ@BSA) in Polyelektrolyt- Mikrokapseln (PC) geladen wurde. In diesem Sensor stellt  
231 PCQ@BSA den Fluoreszenzsensor für  $\text{Cl}^-$  dar. PCs können effizient PCQ@BSA und PEI laden,  
232 und gleichzeitig den  $\text{Cl}^-$  Zugang zu PCQ@BSA unter wenig hinderlichen Bedingungen ermöglichen.  
233 Wir synthetisierten und charakterisierten PCQ und PCQ@BSA. Wir haben zudem mit PCQ@BSA  
234 und Cy5@BSA gleichzeitig beladene PCs präpariert. Allerdings haben wir schlussendlich  
235 herausgefunden, dass die Emission von PCQ@BSA und den PCs überlappt, was Sensorfähigkeit  
236 stark beeinträchtigt hat.

237

## **1. Submicron Polyelectrolyte Capsule-enhanced Enzyme Immobilization**

### **for Improving Enzyme-based Immunoassays**

#### **1.1 Introduction**

Natural enzymes as the native biocatalysts have been broadly used in food<sup>[1]</sup>, environmental<sup>[2]</sup>, and biology fields<sup>[3]</sup> owing to their high catalytic efficiency<sup>[4]</sup>, low producing cost<sup>[5]</sup>, outstanding selectivity<sup>[6]</sup>, and mature preparation routes<sup>[7]</sup>. However, the industrial application of enzymes is usually limited by their weak structure stability, environmental tolerance, and difficulties of recovery and reuse<sup>[8]</sup>. On this basis, enzyme immobilization had been proposed to increase stability, reusability, catalytic activity, and continuous-flow production of natural enzymes<sup>[9]</sup>. Up to now, a series of nanomaterials have been developed to achieve enzyme immobilization, such as gold nanoparticles (AuNPs)<sup>[10]</sup>, magnetic nanoparticles<sup>[11]</sup>, carbon nanotubes<sup>[12]</sup>, silica-based materials<sup>[13]</sup>, polymer-based nanoparticles<sup>[14]</sup>, and resin nanomaterials<sup>[15]</sup>. Although enzyme immobilization provides opportunities to improve stability, half-life, catalytic activity of natural enzymes in enzyme engineering<sup>[16]</sup>, existing enzyme immobilization methods still confront significant challenges. For instance, rigidly labeled enzymes that rely on host nanomaterials have low conformational freedom, influencing molecular recognition<sup>[17]</sup>. Immobilizing an enzyme by encapsulation may affect the enzyme's catalytic activity due to the limited product or substrate mass transfer<sup>[18]</sup>. Traditional adsorption methods have low capacity and high leakage due to weak interactions or pore size mismatches<sup>[19]</sup>. Therefore, there is an urgent demand to explore mature nanoplatforms to overcome these obstacles so that enzyme immobilization can better serve those industries rely on enzyme engineering.

Polyelectrolyte capsule (PC) is prepared by adsorbing oppositely charged polyelectrolytes on the surface of colloidal particles layer by layer (LbL), followed by nuclear dissolution<sup>[20]</sup>. In general, there are two well-defined compartments in the preparation of PCs, including expendable core and polyelectrolyte shell<sup>[21]</sup>. Among them, the main function of expendable core is the regulation of size of PCs, which can be varied from 0.1 to 10  $\mu\text{m}$ <sup>[22]</sup>. In addition, the expendable core could also impact

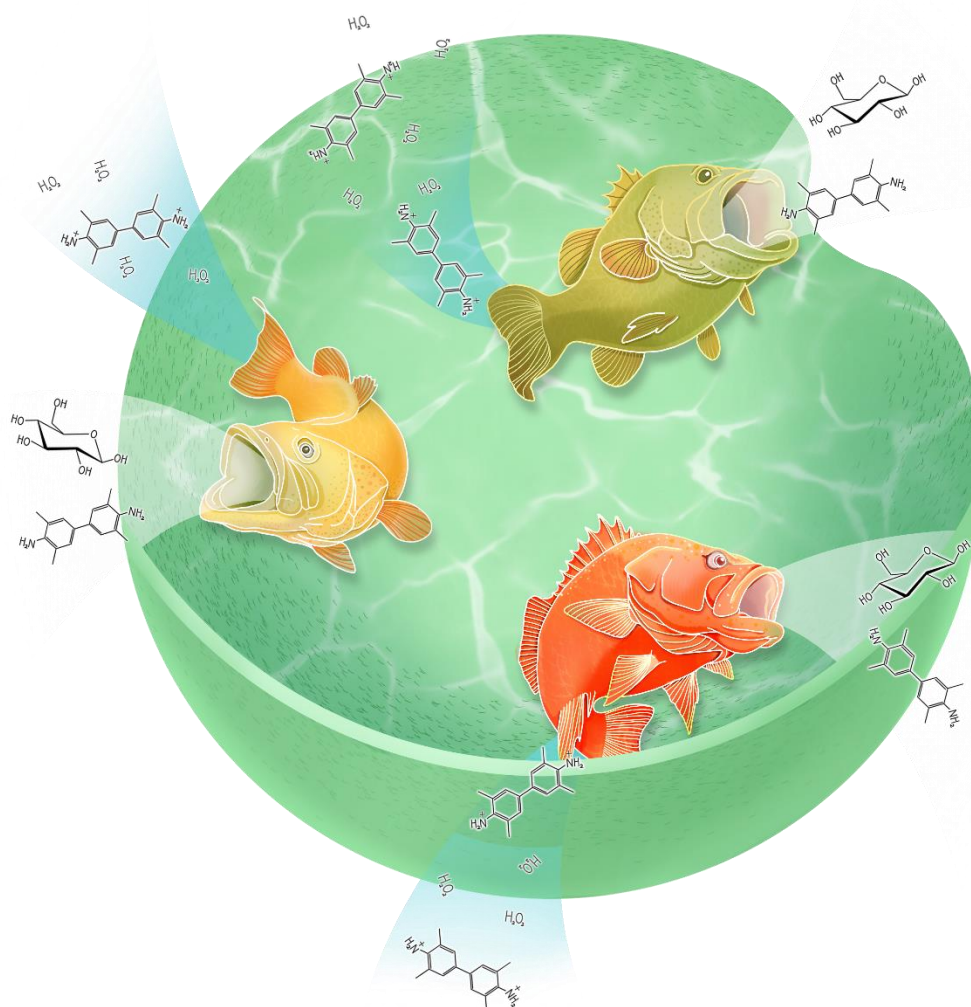
the loading efficiency of that cargo which needs be loaded into PCs by coprecipitation<sup>[23]</sup>. One of the most characters of PCs is the semi-permeability, which is permeable to small molecules, whereas macromolecular compounds are excluded in most conditions<sup>[24]</sup>. Up to now, PCs have been considered to immobilize enzyme due to the controlled semi-permeability could achieve the sustained drug release in target region and protect immobilized enzyme from external detriment without impact of substrate and product mass transfer<sup>[25]</sup>. It is worth to mention that PCs can provide capacious for enzyme conformational freedom (**Scheme 1**). More importantly, the biosafety of PCs could be managed by modulating natural and synthetic polyelectrolytes, which implies PCs could be used for biological applications<sup>[26]</sup>. Particularly, there are a number of polyelectrolytes have been designed to respond to biological factors and external energy fields, such as enzymes<sup>[27]</sup>, pH<sup>[28]</sup>, glutathione<sup>[29]</sup>, light irradiation<sup>[30]</sup>, and heating<sup>[31]</sup>, results in the promotion of development of remotely controlled enzyme release from PCs.

Up to now, many natural enzymes, including horseradish peroxidase (HRP)<sup>[32]</sup>, glucose oxidase (GOx)<sup>[33]</sup>, catalase (CAT)<sup>[34]</sup>,  $\alpha$ -galactosidase<sup>[35]</sup>, alkaline phosphatase<sup>[36]</sup>, malate dehydrogenase<sup>[37]</sup>, and so on, have been successfully immobilized in PCs, and these developed biocatalysts have also been broadly used in biosensing, heterogeneous catalysis, clinical medicine, and cell biology<sup>[38]</sup>. Sufficient research results prove that PCs can encapsulate a large number of different enzyme molecules to achieve enormous signal amplification, and can also provide protection for the encapsulated enzyme molecules to extend their storage and catalytic stability<sup>[39]</sup>. Although there are publications proven that the PCs encapsulation could enhance the catalytic activity of natural enzymes, systematic research about the impact of PCs encapsulation to enzyme catalytic activity is remain lacking. More importantly, in most cases, the size of PCs in enzyme immobilizations is micron scale, which limited the applications potential of these artificial biocatalysts<sup>[40]</sup>.

In this thesis, an investigation of the impact on PC encapsulation to enzyme catalytic activity, in particular, the catalytic kinetics of encapsulated enzymes were measured. Herein, 500 nm CaCO<sub>3</sub> nanoparticle (NPs) was used as expendable submicron core, the polyelectrolyte shell was formed by PSS and PAH. These SPCs are around a factor of 4~10 smaller than typically used PCs with diameters of a few micrometers. The introduction of the porous structure of CaCO<sub>3</sub> NPs as the sacrificial template can provide high loading of enzyme molecules, theoretically<sup>[41]</sup>. In order to

investigate the impact of encapsulation by SPCs on the enzymes' activity, we first encapsulated HRP and GOx into the PCs, to prepare HRP@PCs and GOx@PCs, respectively. The catalytic kinetic results indicate that the packing into PCs not only affects the enzymes' affinity to the substrate and their catalytic rate but also may amplify the catalytic signal of the enzymes. Testing of the stability of HRP@PCs showed that PCs can provide strong protection for packed HRP under harsh conditions. Subsequently, GOx and HRP were used as cascade catalysis combination to investigate the potential of PCs in enzymatic cascade reactions. In this combination, the intermediate product H<sub>2</sub>O<sub>2</sub> was readily consumed by hemin or CAT in biological samples. The results indicate that the microenvironment constructed by SPCs could effectively locally retain H<sub>2</sub>O<sub>2</sub> when CAT was present in the system, thereby maintaining a stable cascade reaction. Based on these results, we then used HRP-loaded SPCs to establish an ELISA for the detection of *E. coli* O157:H7. The results show that the detection sensitivity of the enzyme amplification ELISA was 280 times greater than that of the conventional HRP-based ELISA. In general, this work evaluated the potential of 500 nm SPCs as enzyme immobilizers in amplifying enzyme signals, improving enzyme stability, promoting the development of multi-enzyme cascade reaction catalysts, and enhancing the sensitivity of enzyme-based immunoassays.





**Scheme 1.** Schematic diagram of using PCs for enzyme immobilization. The PCs-encapsulated enzyme could achieve complete conformational freedom like fish living in fish tank since the capacious space provided by PCs. More importantly, the PCs as a classical semipermeability material allow highly effective mass transfer and provide protection to the enzymes against external environment.

## 1.2 Experimental section

### 1.2.1 Materials

Calcium chloride ( $\text{CaCl}_2$ ), sodium carbonate ( $\text{Na}_2\text{CO}_3$ ), polystyrene sodium sulfonate (PSS,  $M_w$ : 70000), polyallylamine hydrochloride (PAH,  $M_w$ : 15000), bovine serum albumin (BSA), glucose, ethylenediaminetetraacetic acid $\cdot$ 2Na (EDTA $\cdot$ 2Na), HRP, CAT, and GOx were purchased from Sigma-Aldrich Chemical (Shanghai, China).  $\text{H}_2\text{O}_2$ , 3,3',5,5'-tetramethylbenzidine (TMB), streptavidin (SA), sulfo-NHS-biotin, fluorescein isothiocyanate (FITC), and RhB isothiocyanate were purchased from Thermo Fisher Scientific Inc. (Shanghai, China). Purified Milli-Q water prepared from the Milli-Q system was used throughout this study (Millipore, Milford, MA, USA). Phosphate buffer (PB, pH 7.4, 0.01 M) was prepared by adding 290.10 mg of  $\text{Na}_2\text{HPO}_4\cdot 12\text{H}_2\text{O}$  and 68.05 mg of  $\text{NaH}_2\text{PO}_4\cdot 2\text{H}_2\text{O}$  in 1000 mL of Milli-Q water. Phosphate-buffered saline (PBS) solution was prepared by adding NaCl into PB at the concentration of 0.01 M. PBST (washing buffer) was prepared by adding 0.5% Tween-20 to the PBS solution. The pH was adjusted to 7.4 before use unless otherwise specified. All other analytical-grade chemicals were purchased from Sinopharm Chemical Corp. (Shanghai, China) and used without further purification.

### 1.2.2 Instrument and characterization

UV-visible absorbance spectra were collected on a UV-vis spectrophotometer (G10S, Thermo Fisher Scientific Inc., USA). Dynamic light scattering (DLS) analysis was conducted with a Malvern Nano-Z90 zetasizer (Malvern Panalytical Ltd., Worcestershire, UK). The concentration of PCs was measured by a nanoparticle tracking analysis machine (Nano Sight LM 14C, Malvern Panalytical Ltd.). The shape and size of the nanoparticles were determined with a JEOL transmission electron microscope (TEM; JEM 2100, Tokyo, Japan) and a Hitachi scanning electron microscope (SEM; S-4800, Tokyo, Japan). A commercial 96-well plate reader was obtained from Corning Inc. Technology company (Cytation 5, BioTek, USA).

### 1.2.3 The synthesis of 500 nm $\text{CaCO}_3$ NPs and coprecipitation method

To synthesize cargo loaded 500 nm  $\text{CaCO}_3$  NPs, a synthesis buffer was first prepared by adding 45 g glycol into 200 g freshly prepared Milli-Q water. Subsequently, 50 mg/mL PSS solution, 2 mg/mL  $\text{Na}_2\text{CO}_3$  solution, and 2 mg/mL  $\text{CaCl}_2$  solution were prepared by dissolving the corresponding chemical powder into the synthesis buffer. Then, 1 mL of  $\text{CaCl}_2$  solution, 50  $\mu\text{L}$  of cargo solution, and 250  $\mu\text{L}$  of PSS solution were added to a 5 mL beaker and stirred at 550 rpm for 10 min to fully form the  $\text{CaCO}_3@\text{PSS}$  complex. After that, 1 mL of  $\text{Na}_2\text{CO}_3$  solution was quickly added into the mixture and stirred at 550 rpm for 30 min. The cargo containing  $\text{CaCO}_3$  NPs with PSS ligand ( $\text{CaCO}_3@\text{PSS}$ ) was purified by centrifugation at 6000 rpm for 10 min, and the precipitate was washed two times with the synthesis buffer.

### 1.2.4 The preparation of SPCs

The PCs were formed by polyelectrolytes with opposite charge through a layer-by-layer process<sup>[42]</sup>. Next, a layer-by-layer process was carried out on the 500 nm  $\text{CaCO}_3@\text{PSS}$  containing the enzymes. First, the as-prepared  $\text{CaCO}_3@\text{PSS}$  was resuspended in 950  $\mu\text{L}$  of synthesis buffer, to reduce the aggregation, a short ultrasound treatment is needed for  $\text{CaCO}_3@\text{PSS}$ , and then 50  $\mu\text{L}$  PAH solution was added to this mixture and ultrasonicated for 5 min. The ultrasonically treated solution was then moved to a shaker and shaken for 15 min. The PAH-coated NPs ( $\text{CaCO}_3@\text{PSS}/\text{PAH}$ ) were then purified through centrifugation at 6000 rpm for 10 min. The precipitate was washed twice with the synthesis buffer. Similar procedures were applied to achieve subsequent additional PSS and PAH layers. Finally, the resulting  $\text{CaCO}_3@(\text{PSS}/\text{PAH})_n$  NPs were suspended in 1 mL of Milli-Q water and stored at 4 °C for further use. For loading nanomaterials between the layers of polyelectrolytes, the nanomaterials which have opposite surface charge with the last layer of SPCs, were added to react with SPCs via a same process of LbL.

Afterward, 5 mL of freshly prepared  $\text{EDTA}\cdot 2\text{Na}$  solution was then added into the above-prepared  $\text{CaCO}_3@(\text{PSS}/\text{PAH})_n$  NP solutions to dissolve the  $\text{CaCO}_3$  core. These mixtures were then moved to 4 °C and kept dissolving overnight. The capsules were purified by centrifugation at 8000 rpm for 15 min and resuspended in Milli-Q water.

### 1.2.5 Measurement of the catalytic kinetics of soluble and PC-immobilized enzymes

Kinetic measurements were carried out by following the enzymatic (i.e. HRP caused) conversion of TMB by monitoring the change in absorbance at 650 nm with 0.5 min intervals. Experiments were conducted using 11 pM HRP in 1.0 mL of 0.10 M sodium acetate (NaAc) buffer (pH 5.0) at 37 °C or 0.125 pM HRP@PCs in 1.0 mL of 0.10 M NaAc buffer (pH 5.0) at 37 °C. To investigate double reciprocal plots of the activity of HRP, assays were performed under standard reaction conditions as described above by varying the concentrations of TMB at a fixed concentration of H<sub>2</sub>O<sub>2</sub> or vice versa. The Michaelis-Menten constant was calculated using the Lineweaver Burk plot:  $1/V = K_m / (V_{\max}[S]) + 1/V_{\max}$ , where  $V$  is the initial velocity,  $V_{\max}$  is the maximal reaction velocity, and  $[S]$  corresponds to the substrate concentration. As reported by Zhang et al, the catalytic kinetics of GOx were measured by using a similar procedure via a HRP-coupled colorimetric assay<sup>[43]</sup>. In brief, GOx was used to catalyze glucose, the generated H<sub>2</sub>O<sub>2</sub> could be measured by HRP-carried out colorimetry assay.

### 1.2.6 Preparation of FITC-labeled HRP and RhB-labeled GOx

One milliliter of 1 mg/mL FITC solution was mixed with 20 mg/mL HRP solution at 0.13 M NaHCO<sub>3</sub> solution (pH 8.0) for 12 h to prepare FITC-labeled HRP. Then, the excess FITC was removed by a PD-10 chromatographic column (Global Life Sciences Solutions Operations UK Ltd, 17-0851-01). FITC-labeled HRP was recovered by freeze-drying for further use. RhB-labeled GOx was prepared by a similar procedure.

### 1.2.7 Biotin-labeling of detection antibodies

Four milligram of antibody were added to sulfo-NHS-biotin solution (0.05 mg/mL) dissolved in PBS solution (pH 7.4, 0.01 M). Reaction was carried out on a mixer for 4 h, followed by dialysis with PBS solution (0.01 M, pH 7.4) for 3 days, in order to get purified biotinylated antibodies.

### 1.2.8 SA-labeled HRP@SPCs

With reference to the method reported by Shao et al., we directly coupled SA and PCs through electrostatic interaction<sup>[44]</sup>. First, SA was added to 1 mL of PC solution (PBS, pH 6.5, 0.01 M) dropwise to a final concentration of 10 µg/mL and was reacted at 25 °C for 60 min. After the reaction, 100 µL of 1% (W/V) BSA solution was added to block the excess sites on the PCs by 30 min reaction. Excess antibodies were removed by centrifugation and discarding of the supernatant containing the free antibodies, and the precipitate containing the SA-labeled HRP@PCs was redissolved in 500 µL of PBS.

### 1.2.9 Detection procedure of the HRP@SPCs-based ELISA

First, 100 µL of antibody (5 µg/mL) used as capture antibody for the coating of the plates was dissolved in PBS buffer (0.01 M, pH 7.4) and the solution was added to a 96-well plate and reacted overnight at 4 °C. After the reaction, the plate was washed with PBST 3 times, and 300 µL BSA (10 mg/mL), used for blocking non-specific adsorption, was added to react at 37 °C for 2 h. Then, the 96-well plate was rewashed with PBST 3 times, and 100 µL of the standard samples to be tested with different concentrations were added and reacted at 37 °C for 1 h. Next, the 96-well plate was washed with PBST 3 times, and 100 µL biotin-labeled detection antibody (10 µg/mL) was added at 37 °C for 1 h. After the reaction, the 96-well plate was washed three times by PBST for removing the excess biotinylated detection antibodies. Afterward, 100 µL of SA-SPC (15 µg/mL) was added to the microplate and the 96-well plate was placed at 37 °C to connect HRP-loaded PCs and immunocomplex by the highly effective reaction of biotin and SA. Then, I washed the 96-well plate for three times for removing the unreacted SA-PCs. Finally, I added 100 µL of TMB substrate to per-well of the plate and placed the 96-well plate at 37 °C for 30 min. The absorbance at 650 nm was measured with a 96-well plate reader and photographed with a camera.

### 1.2.10 Bacteria culture

One hundred microliter of the bacterial solution was added to the Luria-Bertani (LB) broth and cultured for 12 h in a 37 °C shaker with noticeable turbidity. The bacteria were activated on the

416 nutrient agar plate and cultured for 12 h in a 37 °C constant temperature incubator. After colonies  
417 appeared, the inoculating loop was used to pick a single colony, inoculate it into the LB broth, and  
418 cultivate it overnight in a 37 °C shaker at 150 rpm. One milliliter of the bacterial solution was placed  
419 in a 1.5 mL sterile centrifuge tube and gradient diluted with sterile PBS solution (pH 7.4, 0.01 M).  
420 Then, 100 µL of the diluted bacterial solution was applied to the nutrient agar plate and placed in a  
421 37 °C incubator for counting. The high concentration of the bacterial solution was placed in water,  
422 boiled for 10 min, and then centrifuged at 8000 g for 5 min. The bacteria were washed 3 times with  
423 sterile PBS solution. The precipitate was stored at 4 °C for later use after being resuspended.

## 1.3 Results and discussion

### 1.3.1 Synthesis and characterization of enzyme-loaded SPCs

In the present work, the classical layer-by-layer technology was used to prepare SPCs by employing  $\text{CaCO}_3$  NPs as the sacrificial template (Figure 1a). HRP-loaded  $\text{CaCO}_3$  NPs (HRP@ $\text{CaCO}_3$  NPs) were first synthesized by a PSS-regulated method. As shown in Figure 1b, the synthesized HRP@ $\text{CaCO}_3$  NPs exhibited uniform sphericity with a diameter of  $530 \pm 57$  nm ( $n = 50$ ). The hydrodynamic diameter of HRP@ $\text{CaCO}_3$  NPs was measured as 497 nm (Figure 1c). Afterward, a polyelectrolyte layer coating was formed by a LbL assembly process<sup>[45]</sup>. In theory, more layers of PSS and PAH can provide higher stability to avoid unwanted leakage. However, as each additional layer requires a washing step, the increased number of washing steps also can lead to a loss of the encapsulated molecules. PSS and PAH layers may also restrict the catalytic activity of the packed enzymes, e.g. due to hindered transport of enzymatic substrates and products. Therefore, we first optimized the layer number of PSS and PAH layers by measuring the relative catalytic activity to obtain high catalytic activity and stability. As shown in Figure 2, the relative catalytic activity of HRP-loaded  $\text{CaCO}_3@(\text{PSS}/\text{PAH})_n$  decreases as the number of PSS/PAH layers increases before three PSS/PAH layers. Thus, the optimum layer number of PSS/PAH was found to be three. The results of zeta-potential measurements for each layer indicated that PSS and PAH were successfully coated on the surface of  $\text{CaCO}_3$  NPs (Figure 1d). Figure 1c shows a slight increase in size after dissolving the  $\text{CaCO}_3$  template cores. Subsequently, the saturated HRP loading amount was optimized. In the optimization, 0, 0.25, 0.50, 1.00, 2.00, and 4.00 mg/mL HRP solutions were used to synthesize  $\text{CaCO}_3@(\text{PSS}/\text{PAH})_3$ . Under the same  $\text{CaCO}_3@(\text{PSS}/\text{PAH})_3$  concentration,  $\text{CaCO}_3@(\text{PSS}/\text{PAH})_3$  prepared by 1 mg/mL HRP solution had the highest catalytic activity (Figure 3). Hence, 1 mg/mL HRP was used to prepare the HRP-loaded  $\text{CaCO}_3@(\text{PSS}/\text{PAH})_3$ . After preparing HRP-loaded  $\text{CaCO}_3@(\text{PSS}/\text{PAH})_3$ , the  $\text{CaCO}_3$  template was dissolved by  $\text{EDTA} \cdot 2\text{Na}$  to prepare HRP-loaded SPCs (HRP@SPCs) (Figure 1e). The catalytic properties of the HRP@SPCs were tested by catalyzing  $\text{H}_2\text{O}_2$  and TMB. As shown in Figure 4, HRP@ $\text{CaCO}_3$  NP- and HRP@SPC-catalyzed  $\text{H}_2\text{O}_2$  and TMB exhibited the same typical blue color as the HRP group. The

relevant UV absorbance spectrum (Figure 1f) shows that the maximum absorbance of the blue solution is 650 nm. All the above results confirmed that HRP was successfully loaded into the HRP@SPCs.

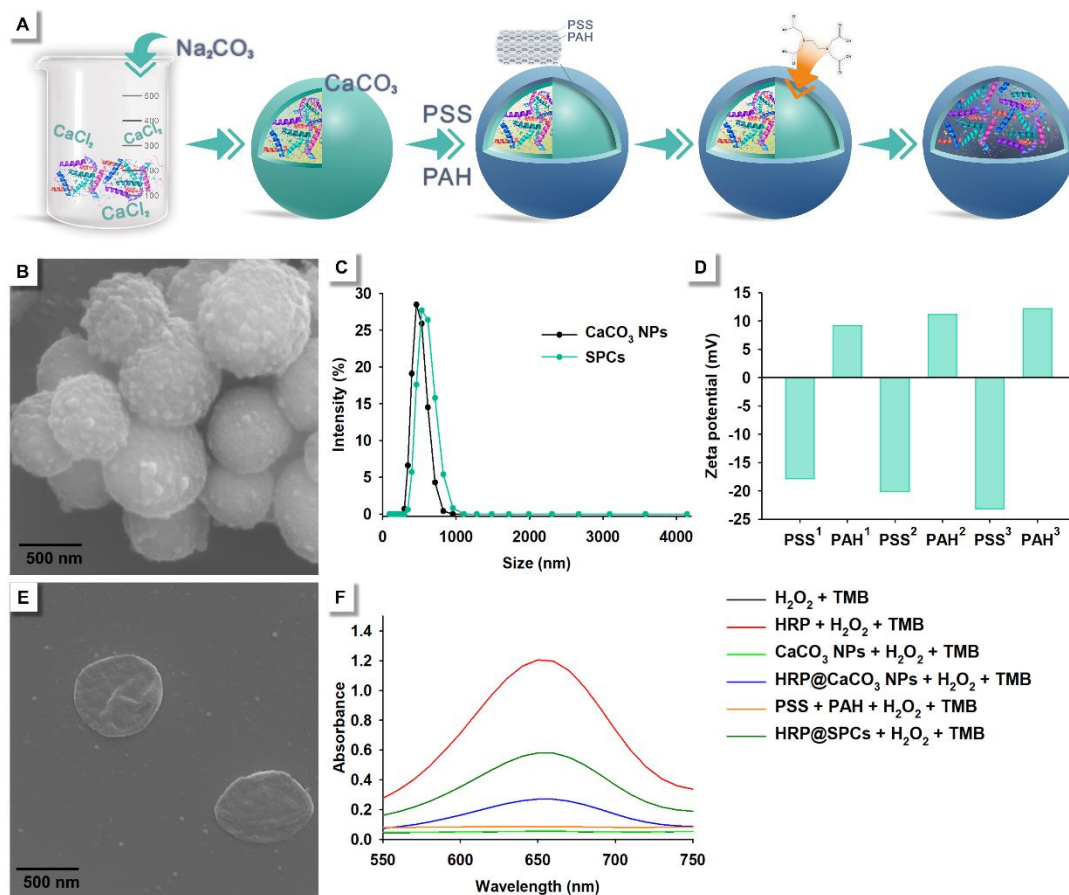


**Figure 1.** Synthesis and characterization of HRP-loaded submicron polyelectrolytes capsules (HRP@SPCs). **(A)** Schematic diagram of the synthesis of enzyme-loaded SPCs. Anion polyelectrolyte PSS was employed to regulate the  $\text{CaCO}_3$  synthesis. Then the prepared  $\text{CaCO}_3$  core was coated by PSS and cation polyelectrolyte PAH via layer-by-layer technology. The hollow SPCs were obtained by using  $\text{EDTA} \cdot 2\text{Na}$  to dissolve  $\text{CaCO}_3$ . **(B)** SEM of  $\text{CaCO}_3$  NPs. **(C)** DLS analysis of the hydrodynamic diameter of  $\text{CaCO}_3$  NPs and SPCs. **(D)** Zeta potentials of the  $\text{CaCO}_3$  NPs after the addition of subsequent polyelectrolyte double layers of PSS/PAH. DLS and zeta potential analyses were performed in ultrapure water. **(E)** SEM of the synthesized HRP@SPCs. **(F)** UV-vis absorbance spectra of the catalytic reaction of TMB and  $\text{H}_2\text{O}_2$  by serial catalysts.



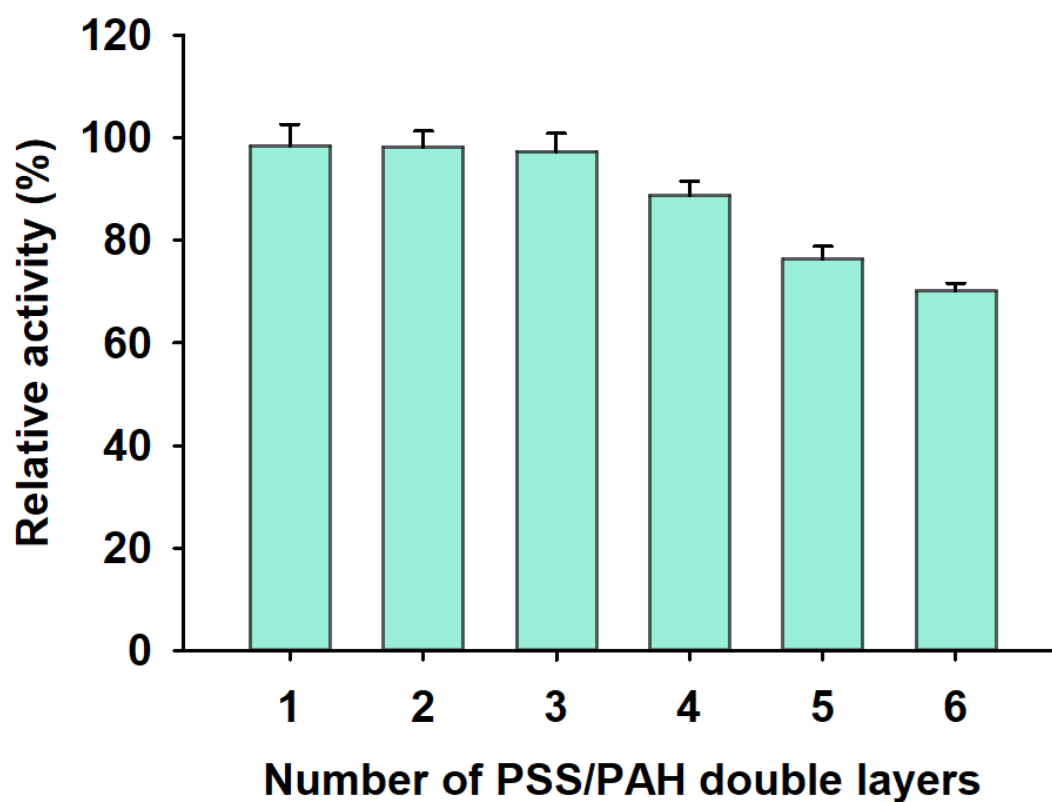


**Figure 2.** The optimization of the number of double-layers for the coating of  $\text{CaCO}_3$  NPs. In the optimization, the catalytic activities of HRP in the  $\text{CaCO}_3$  NPs with a coating of different numbers of PSS/PAH double-layers were measured to evaluate the influence of the PSS/PAH layers on the catalytic performance of HRP.

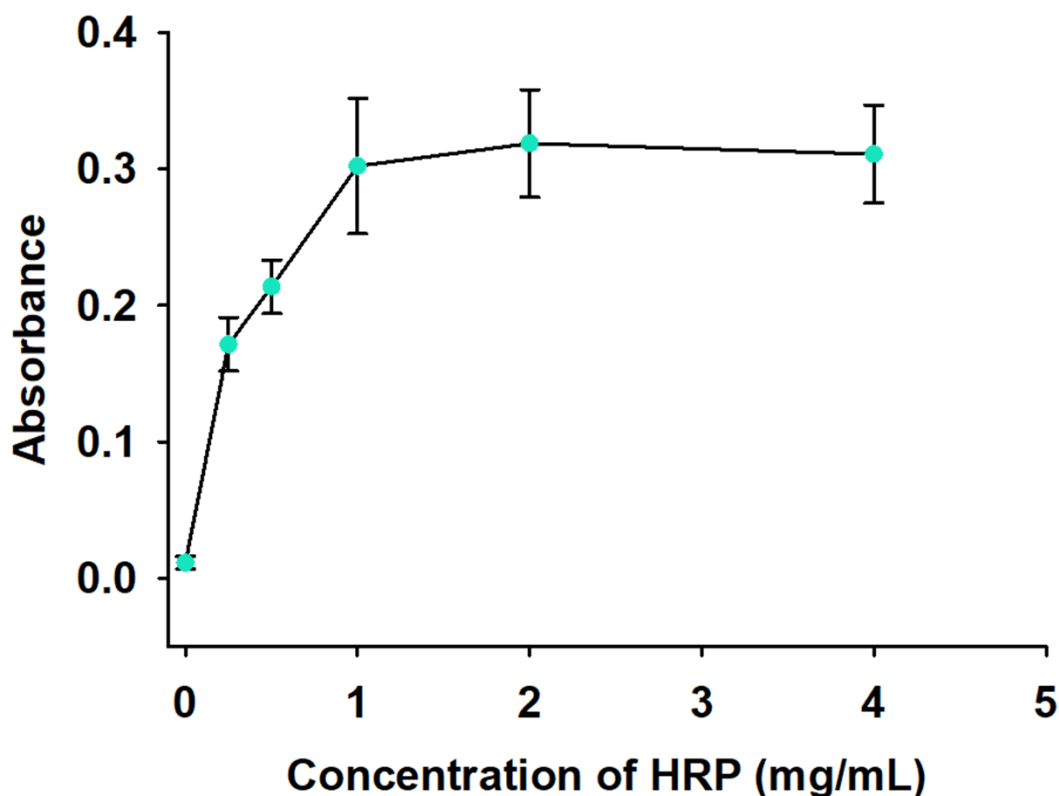


**Figure 3.** The loading ability of  $\text{CaCO}_3$  NPs with HRP. Different concentrations of HRP were used during the synthesis of  $\text{CaCO}_3$  NPs, and the catalytic activities of these synthesized  $\text{CaCO}_3$  NPs with integrated HRP were evaluated by catalyzing  $\text{H}_2\text{O}_2$  and TMB. The optical density at 650 nm of the solution after 10 min of reaction is plotted versus the concentration of HRP which has been used for the NP synthesis.

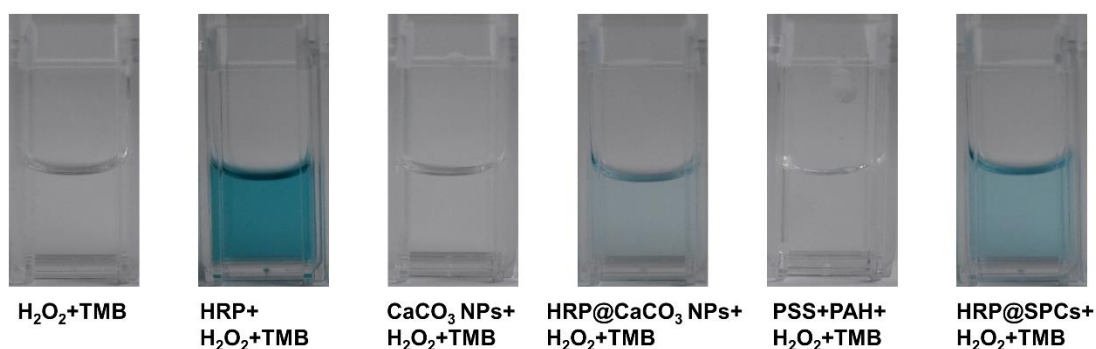


**Figure 4.** Photographs of HRP, HRP@ $\text{CaCO}_3$  NP-, SPC-, and HRP@SPC- catalyzed  $\text{H}_2\text{O}_2$  and TMB solutions.

### 1.3.2 Catalytic kinetics of soluble and SPC-packed HRP

After preparing the HRP@SPCs, the impact of SPCs on the catalytic kinetics of HRP was evaluated by a steady-state kinetics assay. By comparing the catalytic kinetics of HRP and HRP@SPCs, the signal amplification potential of SPC-based HRP immobilization and the effect of packing HRP into SPCs can be roughly understood. Before the evaluation, the catalytic conditions of HRP and HRP@SPCs, including reaction temperature,  $\text{H}_2\text{O}_2$  concentration, pH, and reaction time, were optimized. **Figure 5** shows that the optimum catalytic conditions of HRP@SPCs are 37 °C, 0.1 M  $\text{H}_2\text{O}_2$ , pH 5.0, and 30 min of catalytic reaction time; the optimum catalytic conditions of soluble HRP were 37 °C, 0.025 M of  $\text{H}_2\text{O}_2$ , pH 5.6, and 15 min of catalytic reaction time. After obtaining the optimum catalytic conditions, the parameters involving the Michaelis constant ( $K_m$ ), maximal rate ( $V_{\max}$ ), and turnover number ( $K_{\text{cat}}$ ) of HRP and HRP@SPCs were measured. Typical Michaelis-Menten equations were obtained by changing  $\text{H}_2\text{O}_2$  or TMB concentrations (**Figure 6**)<sup>[46]</sup>, and the results are summarized in **Table 1**. As shown in **Table 1**, regardless of whether  $\text{H}_2\text{O}_2$  or TMB was used as a substrate, the  $K_{\text{cat}}$  value of HRP@SPCs showed one order of magnitude enhancement compared to that of soluble HRP, indicating that SPC encapsulation is a potential signal amplification strategy for immunoassays.

In contrast, the  $V_{\max}$  value and affinity of the enzyme towards the substrate were weakened by SPC encapsulation. Of note, SPC encapsulation exhibited a weaker influence when using TMB as the substrate. These results indicate that SPC encapsulation might impact enzyme kinetics. To further prove this conclusion, we then used SPCs to load GOx (GOx@SPCs) and tested the catalytic kinetics of soluble GOx and GOx@SPCs using glucose as the substrate (**Figure 7**). The results in **Table 1** show that SPC encapsulation weakens the affinity of GOx and glucose, but promotes their catalytic rate. Thus, in general, SPC encapsulation reduced the affinity of enzyme and substrate. This result is probably due to the polyelectrolyte walls that hinder the mass transport of substrates and products. However, concerning catalytic rates, SPC encapsulation exhibited different effectiveness for HRP and GOx. This may explain the current debate about the effect of polyelectrolytes on enzyme activity. The inconsistency in previous reports suggests that the influence of polyelectrolytes on enzyme activity is likely to vary depending on the nature of enzymes and substrates.

**Table 1.** The catalytic kinetics of HRP, GOx, HRP@SPCs, and GOx@SPCs according to the Michaelis-Menten model. The concentrations of HRP, GOx, HRP@SPCs, and GOx@SPCs were 11 pM, 0.125 pM, 0.5 nM, and 1 nM, respectively.

E = Enzyme	[E] (M)	Substrate	$K_m$ (mM)	$V_{max}$ ( $10^{-8}$ M/s)	$K_{cat}$ ( $s^{-1}$ )
HRP	$1.10 \times 10^{-11}$	H <sub>2</sub> O <sub>2</sub>	2.39	3.21	$2.92 \times 10$
HRP	$1.10 \times 10^{-11}$	TMB	0.26	4.61	$4.18 \times 10^3$
HRP@SPCs	$1.25 \times 10^{-13}$	H <sub>2</sub> O <sub>2</sub>	51.80	1.15	$9.20 \times 10^4$
HRP@SPCs	$1.25 \times 10^{-13}$	TMB	0.20	0.71	$5.68 \times 10^4$
GOx	$5.00 \times 10^{-10}$	Glucose	4.23	253.66	$5.07 \times 10^3$
GOx@SPCs	$1.00 \times 10^{-11}$	Glucose	54.94	357.50	$3.58 \times 10^5$

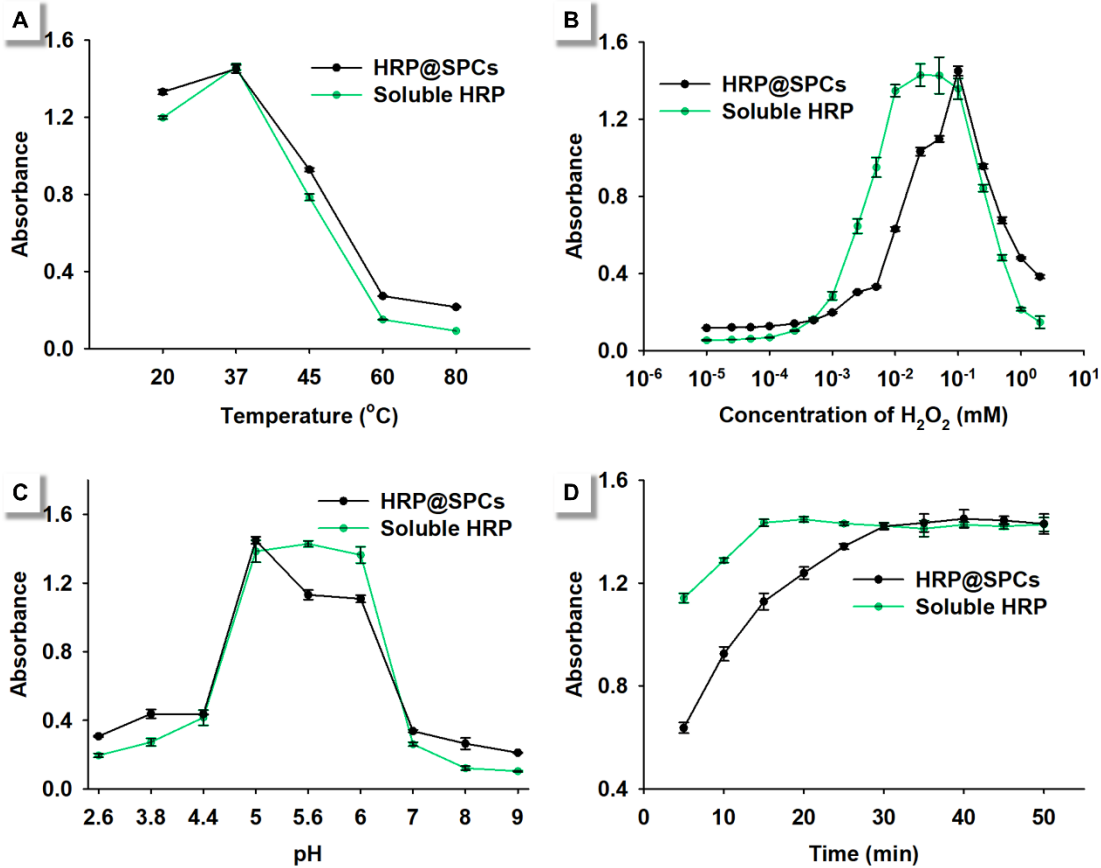


**Figure 5.** Optimization of the catalytic conditions of soluble HRP (red) and HRP@SPCs (black). (A) Concentration of H<sub>2</sub>O<sub>2</sub> were 0.05 mM and 0.1 mM for soluble HRP and HRP@SPCs, pH were 5.0 and 5.0 for soluble HRP and HRP@SPCs, Time of reaction before absorption measurement were 30 min and 30 min for soluble HRP and HRP@SPCs. (B) Temperatures were 37 °C, and 37 °C for

soluble HRP and HRP@SPCs, pH were 5.0 and 5.0 for soluble HRP and HRP@SPCs, Time of reaction before absorption measurement were 30 min and 30 min for soluble HRP and HRP@SPCs. (C) Temperatures were 37 °C and 37 °C for soluble HRP and HRP@SPCs, Concentration of H<sub>2</sub>O<sub>2</sub> were 0.025 mM and 0.1 mM for soluble HRP and HRP@SPCs, Time of reaction before absorption measurement were 30 min and 30 min for soluble HRP and HRP@SPCs. (D) Temperatures were 37 °C and 37 °C for soluble HRP and HRP@SPCs, Concentration of H<sub>2</sub>O<sub>2</sub> were 0.025 mM and 0.1 mM for soluble HRP and HRP@SPCs, pH were 5.6 and 5.0 for soluble HRP and HRP@SPCs.

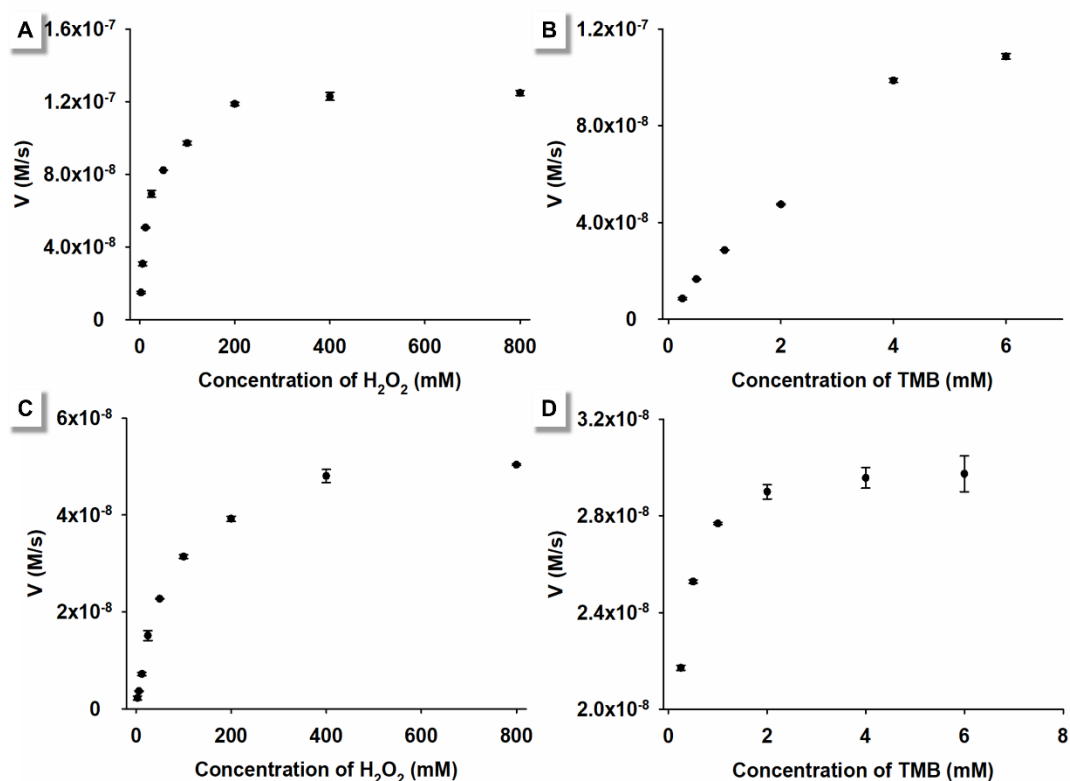


**Figure 6.** Steady-state kinetic assays of HRP and HRP@SPCs. The velocity ( $V$ ) of the reactions according to the Michaelis Menten model was measured using 11 pM HRP in 1.0 mL of 0.10 M sodium acetate buffer (pH 5.0) at 37 °C (A and B); 0.125 pM HRP@SPCs in 1.0 mL of 0.10 M sodium acetate buffer (pH 5.0) at 37 °C (C and D). (A and C) The concentration of TMB was 4.0 mM for HRP, and the H<sub>2</sub>O<sub>2</sub> concentrations were varied. (B and D) The concentration of H<sub>2</sub>O<sub>2</sub> was 1 mM, and the TMB concentration was varied. The error bars indicate the standard deviations of six independent measurements.

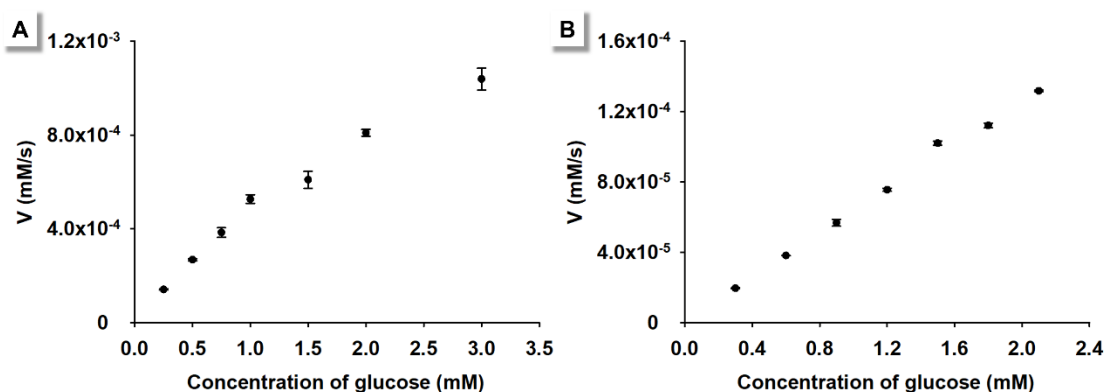


**Figure 7.** Steady-state kinetic assays of GOx and GOx@SPCs according to the Michaelis Menten model. The velocity (V) of the reactions was measured using 0.5 nM GOx and 5 nM HRP in 1.0 mL of PBS solution (pH 7.4) at 37 °C (A and B); 10 pM GOx@SPCs in 1.0 mL of PBS solution (pH 7.4) at 37 °C. The error bars indicate the standard deviations of six independent measurements.

### 1.3.3 Protection performance of SPCs to HRP

In addition to using SPCs to amplify the catalytic signal to enhance the detection sensitivity of enzyme-based immunoassays, the protection performance of SPCs to the loaded enzyme would also be essential for reducing transportation and storage costs. Herein, we used HRP@SPCs to investigate the environmental tolerance of SPC-packed and soluble HRP through 1 h of treatment under different pH values, NaCl solutions, and trypsin solutions (Figure 8A). The relative catalytic activities of packed HRP and free HRP were monitored through catalytic oxidation of TMB by H<sub>2</sub>O<sub>2</sub>. As shown in Figure 8B, soluble HRP exhibited a lower endurance capacity in alkaline and acidic conditions than packed HRP. Meanwhile, packed HRP gave strong endurance capacity in high concentrations of salt solution, which means that SPCs can provide preservation of the loaded HRP (Figure 8C).

On the other hand, soluble HRP lost its catalytic activity at a 10 mg/mL trypsin concentration. In contrast, the catalytic activity of packed HRP had no noticeable change after treatment with high concentrations of trypsin (Figure 8D). All these results proved that SPCs can increase the environmental tolerance of packed HRP. Furthermore, the storage stability of HRP@SPCs was further evaluated by monitoring the catalytic activity of HRP@SPCs and HRP every five days. The HRP and HRP@SPCs were dissolved in 0.01 M PBS solution and stored at 25 °C. As shown in Figure 8E, the catalytic activity of soluble HRP had a significant feebleness on the fifth day and

left only approximately 10% catalytic activity after 30 days, whereas HRP@SPCs retained almost 80% catalytic activity after being stored at 25 °C for 30 days. This finding indicated the excellent long-term storage stability and absence of significant leakage in HRP@SPCs during storage. Thus, SPCs can provide favorable protection to the loaded HRP. These results generally imply that SPC-based enzyme amplification has potential for commercial enzyme-based immunoassays, including improved detection sensitivity and reduced transportation and storage costs.

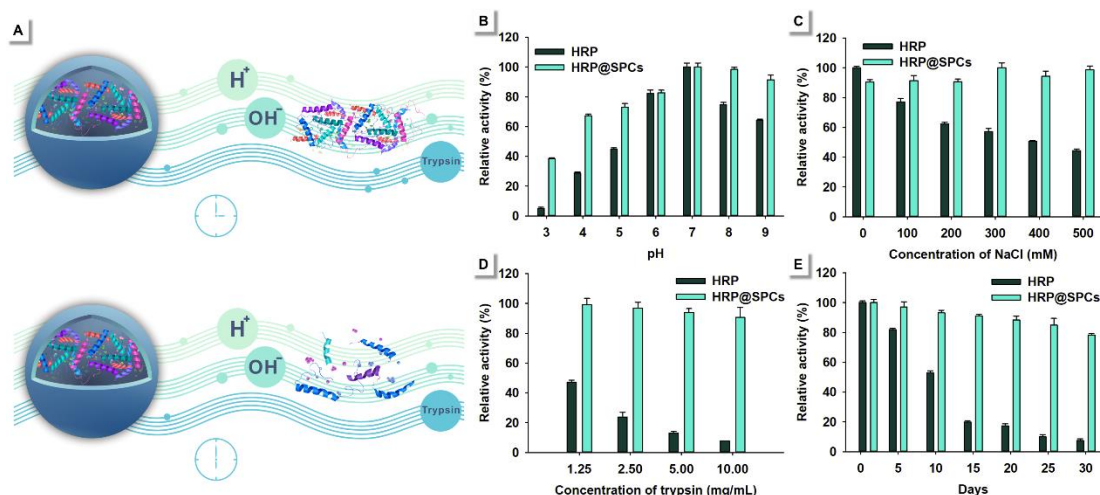


**Figure 8.** Evaluation of the stability of HRP@SPCs and free HRP. (A) Scheme of SPCs on the protection of encapsulated enzyme. Under the protection of SPCs, the immobilized enzyme shows higher harsh condition tolerance than soluble enzyme. (B) The catalytic activity of HRP@SPCs and free HRP after incubation in different pH soluble solutions for 1 h. (C) The effect of NaCl concentration on the activity of HRP@SPCs and soluble HRP. (D) The relative activity of HRP@SPCs and free HRP after exposure to protease trypsin. (E) Storage stability of HRP@SPCs and free HRP at 25 °C and pH 7.0 for one month. For each curve, the value for the maximal absorbance at 650 nm was set as 100% of relative activity. The relative activities of HRP@SPCs and HRP under different conditions were calculated according to the value of 100% of relative activity. All the error bars calculated by three repetitions.

### 1.3.4 SPCs-based enzyme cascade catalysis

To date, growing cascade biocatalysts have been developed. However, most of these cascade biocatalysts fail in practical applications because the complicated catalytic environment is always unamiable for intermediate products of cascade catalysis<sup>[47]</sup>. For example, GOx and HRP cascade

catalysis-based immunoassays for detecting human blood and living cell samples should consider that GOx-generated  $H_2O_2$  may be consumed by hemin or CAT enzymes in the biological environment<sup>[48]</sup>. However, if cascade catalysis can be completed in an independent microenvironment, the risk of intermediate product consumption could be minimized. Therefore, we hypothesized that SPC-based enzyme cascade catalysis amplification can circumvent this risk because the coloaded enzymes can complete cascade catalysis in SPC-provided microenvironments. To verify this hypothesis, GOx and HRP were chosen as model cascade combination to synthesize GOx and HRP coloaded SPCs (GOx@HRP@SPCs). As depicted in **Figure 9A**, GOx could catalyze glucose to generate gluconic acid and  $H_2O_2$ , which in turn is the substrate for the HRP-catalyzed oxidation of TMB. We used SPCs to encapsulate FITC-labeled HRP and RhB-labeled GOx to verify that GOx and HRP could be loaded into SPCs simultaneously. As shown in **Figure 10**, the synthesized GOx and HRP coloaded SPCs (GOx@HRP@SPCs) exhibited a uniform spherical shape with green (FITC) and red (RhB) fluorescence. Then, the catalytic activity of the prepared GOx@HRP@SPCs was evaluated by catalyzing a 250 mM glucose and 8 mM TMB mixture. Interestingly, only GOx@HRP@SPCs and simultaneous addition of GOx and HRP to glucose and TMB could catalyze the oxidation reaction of TMB (**Figure 9B**). Thus, GOx and HRP were successfully loaded into SPCs and exhibited their intrinsic catalytic activity. We then optimized the ratio of GOx and HRP in SPCs to ensure that the GOx@HRP@SPCs could exhibit the highest catalytic performance. The results in **Figure 9C** indicate that the optimum ratio of GOx and HRP in synthesizing GOx@HRP@SPCs was GOx:HRP = 4:6. We, however, want to point out that this is the enzyme ratio in the protein mix used for the encapsulation. As the encapsulation efficiency of GOx and HRP could be different, the resulting enzyme ratio in the SPCs could be somewhat different. Under the optimized synthesis conditions, the catalytic conditions, including pH, catalytic temperature, the concentration of glucose, catalytic time of GOx@HRP@SPCs, and GOx and HRP combinations, were optimized (**Figure 11**). In our concept, GOx and HRP-based cascade catalysis is confined in the SPC-protected microenvironment. The prepared GOx@HRP@SPCs were used to catalyze glucose and TMB mixtures in the presence of CAT to explore this concept. This well-known native enzyme can catalyze the breakdown of  $H_2O_2$  to generate  $O_2$  and  $H_2O$ , protecting cells from the oxidative damage caused by  $H_2O_2$ . For comparison, GOx and HRP combinations with the



same enzyme ratio (GOx:HRP = 4:6) and the same concentration of CAT were used. The results in **Figure 9D** demonstrated that the relative cascade catalysis efficiency of GOx@HRP@SPCs was maintained at 95% after adding CAT into the reaction. In contrast, the GOx and HRP combination (i.e. the enzymes without encapsulation) retained only 48% cascade catalysis efficiency upon the addition of CAT. These results prove that SPCs can provide an independent microenvironment for cascade catalysis and therefore assist cascade catalysis-based immunoassays in circumventing disturbance from samples.

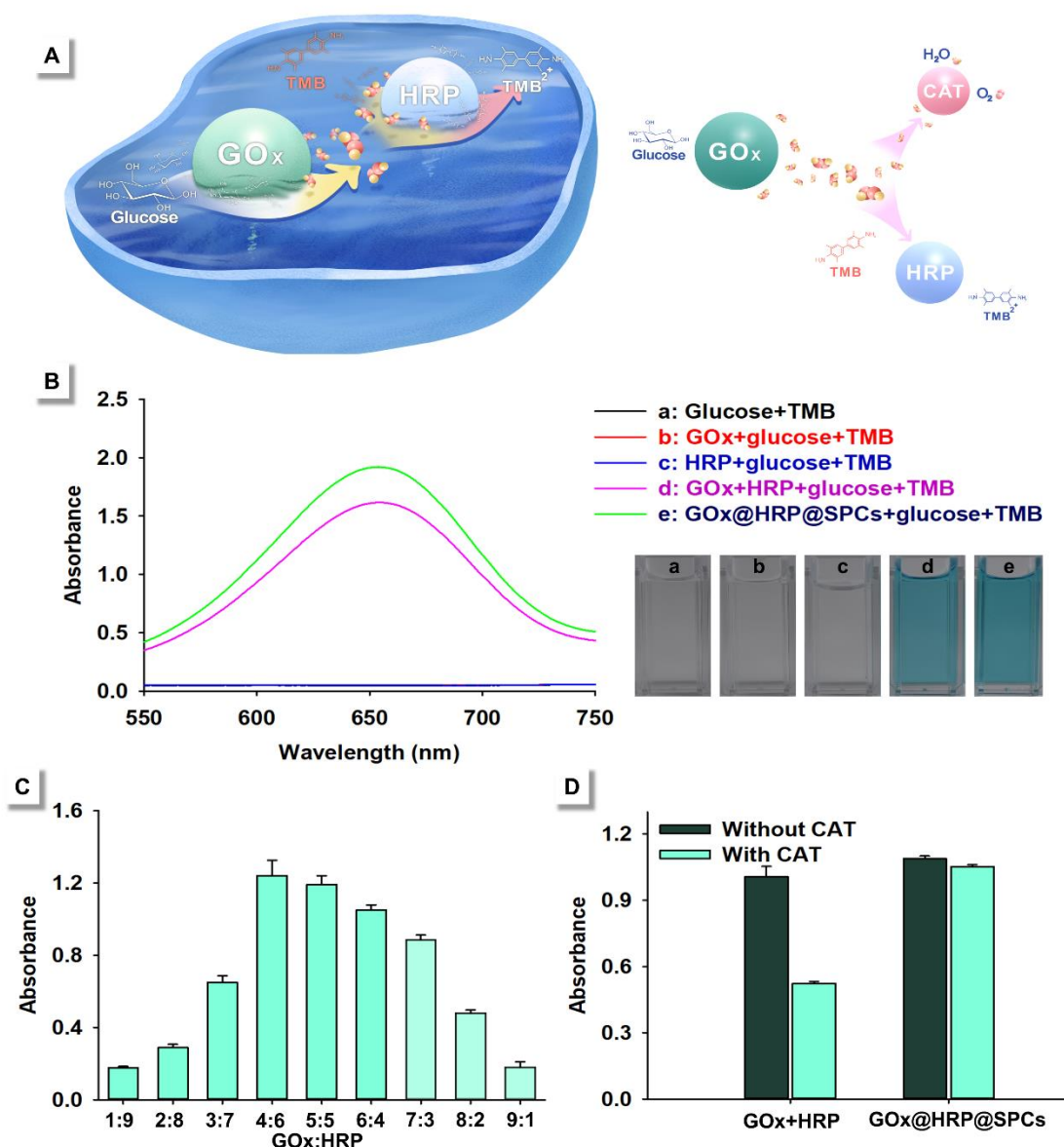
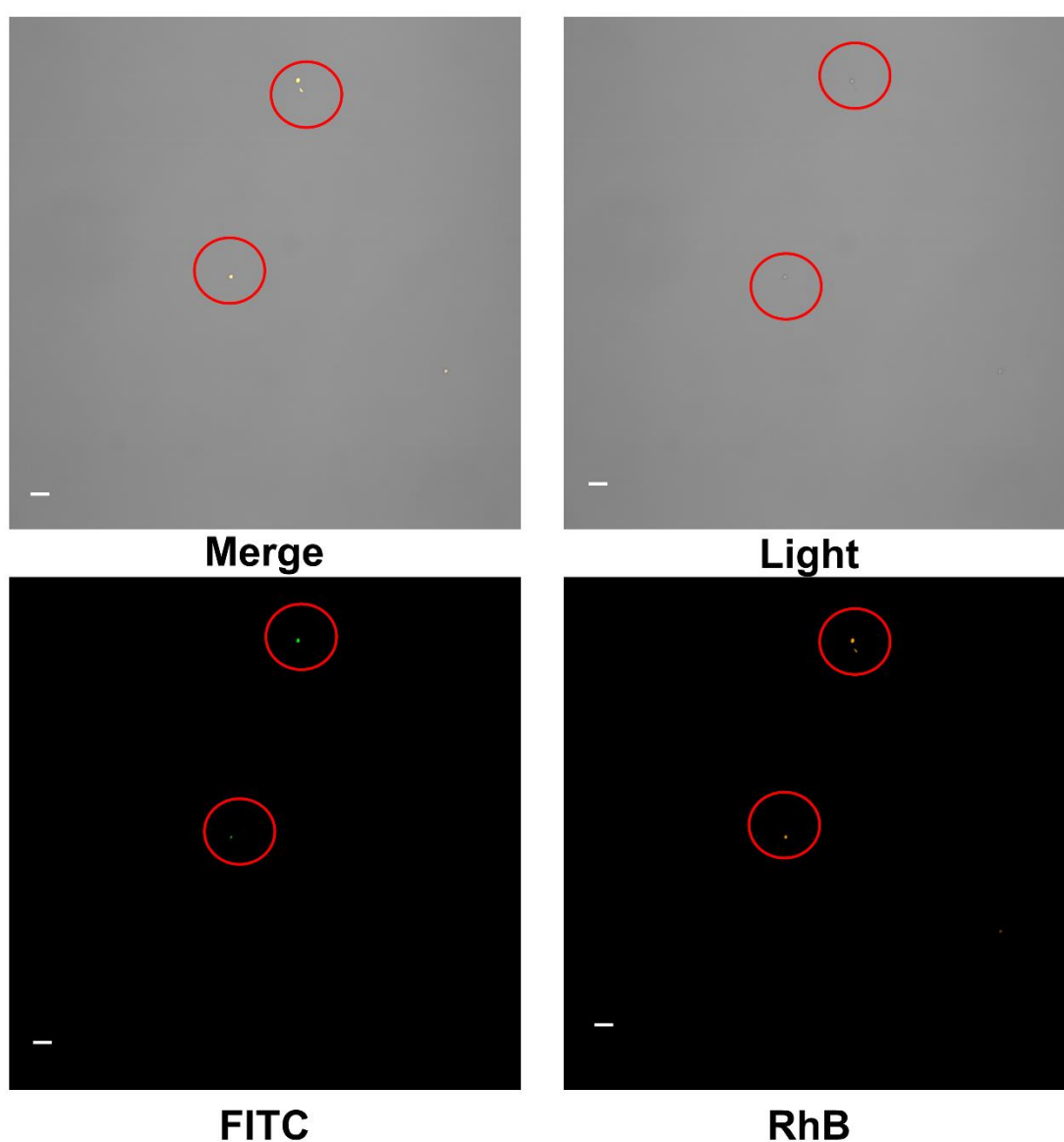


**Figure 9.** SPC-mediated cascade catalytic reaction. **(A)** Schematic diagram of the GOx@HRP@SPC-based cascade catalytic reaction. In theory, SPCs encapsulation enhances the

619 cascade catalytic reaction through promoting present  $\text{H}_2\text{O}_2$  (GOx catalyze glucose to generate  $\text{H}_2\text{O}_2$ )  
 620 to HRP and protecting the degradation of  $\text{H}_2\text{O}_2$  by external CAT. **(B)** GOx, HRP, GOx plus HRP  
 621 mixture, and GOx@HRP@SPCs catalyzed glucose and TMB, respectively. The inset is a  
 622 photograph of these catalytic reactions. **(C)** Optimization of the ratio of GOx and HRP in  
 623 synthesizing GOx@HRP@SPCs. **(D)** Effect of CAT participation on the activity of the GOx plus  
 624 HRP mixture and the GOx@HRP@SPC cascade system. All the error bars calculated by three  
 625 repetitions.



627 **Figure 10.** Laser scanning confocal microscopy (LSCM) images of GOx and HRP coloaded SPCs.  
 628 Scale bar = 20  $\mu\text{m}$ .  
 629

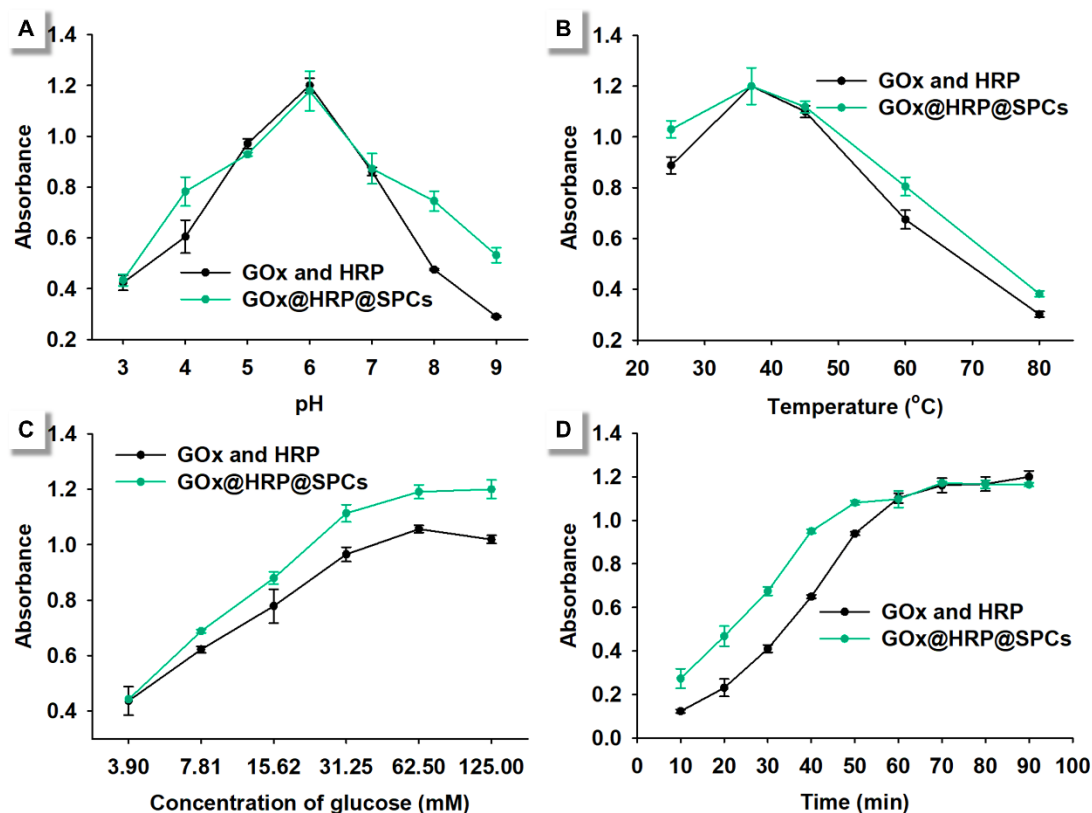


**Figure 11.** Effects of pH (A), temperature (B), the concentration of glucose (C), and catalytic time (D) on the catalytic ability of GOx and HRP mixtures (black line), or GOx@HRP@SPCs (red line). The optical density as recorded at 650 nm under presence of TMB is given. Experiments A, B, and D were carried out using 1.0 ng/mL GOx and 2.0 ng/mL HRP or 1.1 pM GOx&HRP@SPCs with 4 mM TMB and 50 mM glucose. In contract, experiment C was performed with 4 mM TMB and different concentrations of glucose. A) Temperature = 37 °C, Time after which reaction has been recorded = 50 min. B, D) pH = 6.0, Time after which reaction has been recorded = 50 min. C) Temperature = 37 °C, pH = 6.0, Time after which reaction has been recorded = 50 min.

### 1.3.5 Development of HRP@SPC-based ELISA for ultrasensitive detection of *E. coli* O157:H7

ELISA is one of the most common immunoassays for detecting biochemical targets and has been widely used in food safety<sup>[49]</sup>, environmental monitoring<sup>[50]</sup>, and clinical diagnosis<sup>[51]</sup>.

Nevertheless, the major drawback of conventional ELISA is the relatively low detection sensitivity when using HRP to label biorecognition molecules (*e.g.*, antibodies and aptamers)<sup>[50, 52]</sup>. Therefore, enzyme-based amplification technology is a promising strategy to increase the detection sensitivity of ELISA. Herein, we established a HRP@SPC-based ELISA to test SPC-based enzyme amplification for performing signal amplification in immunoassays. In this ELISA, *E. coli* O157:H7 was chosen as the model target analyte, because *E. coli* O157:H7 is a common pathogenic bacterium and requires a very low detection rate or no detection in the food safety standards of many countries<sup>[53]</sup>. The designed capsule-based strategy for the fabrication of highly efficient biocatalysts was then integrated into the ELISA platform with the help of a biotin-SA system to realize highly sensitive detection of *E. coli* O157:H7. In brief, *E. coli* O157:H7 in the sample solution bound to the capture antibodies that were immobilized on 96-well plates, to form immunocomplexes. The formed complexes could then capture biotinylated detection antibodies, and then the captured biotinylated detection antibodies were further linked to SA-labeled HRP@SPCs for detection. To gain the highest detection sensitivity, the coupling conditions of pH and the content of SA on the surface of the SPCs were optimized (Figure 12). Then, the detection conditions also were optimized by a checkerboard titration method at an *E. coli* O157:H7 concentration of  $1 \times 10^5$  CFU/mL. Table 2 shows that the optimal concentrations of biotinylated detection antibodies and capture antibodies were 1.25 and 5  $\mu$ g/mL, respectively. As a comparison, a conventional ELISA was established by a similar method.

Under these optimized conditions, standard curves of HRP@SPCs and HRP-based ELISA for detecting *E. coli* O157:H7 were generated by analyzing a series of *E. coli* O157:H7 spiked milk standard solutions. Using conventional HRP-based ELISA, the standard curve showed a linear detection range at *E. coli* O157:H7 concentrations from  $5 \times 10^4$  CFU/mL to  $5 \times 10^7$  CFU/mL, with a correlation coefficient ( $R^2 = 0.9926$ ; Figure 17A). After SPC amplification, the linear detection range of HRP@SPC-based ELISA was  $5 \times 10^1$  to  $5 \times 10^5$  CFU/mL ( $R^2 = 0.9932$ ; Figure 17A). Even at  $5 \times 10^1$  CFU/mL, the wells also exhibited a distinctive blue color, whereas no color changes appeared in the negative control well (Figure 17B). This result demonstrates the potential of the HRP@SPC-based ELISA in detecting ultralow concentrations of *E. coli* O157:H7, including a single bacterial cell in a 100  $\mu$ L sample solution.

To evaluate the specificity of the developed method, we also tested eight common pathogenic bacteria in spiked milk samples. A significantly increased optical density value in the *E. coli* O157:H7-spiked milk sample is shown in **Figure 17C**, whereas only minor changes were observed in all other samples, indicating excellent selectivity for *E. coli* O157:H7 determination. Recovery and coefficient of variation (CV) studies of *E. coli* O157:H7-spiked samples were conducted to evaluate the accuracy and precision of the proposed method. The results in **Table 3** indicate that our established HRP@SPC-based ELISA has high accuracy and precision and, therefore, could be used for practical applications.

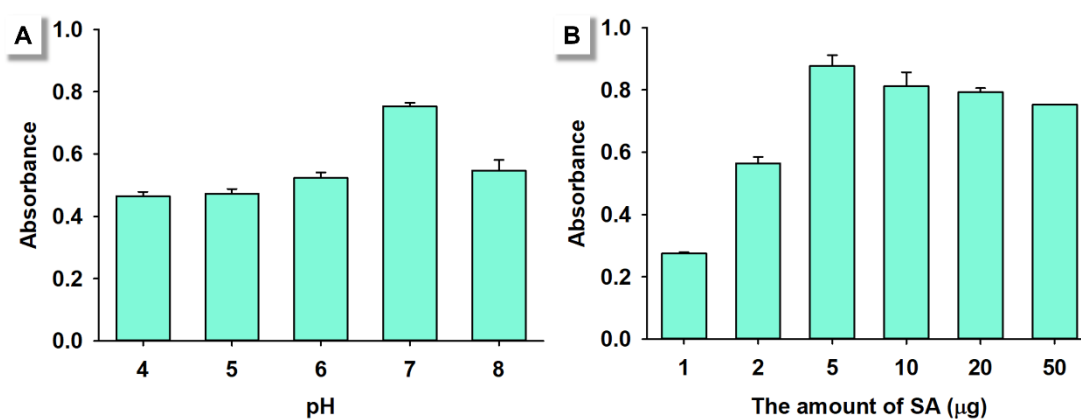


**Figure 12.** Optimization of the labeling conditions of pH (amount of SA = 10 μg) (A) and the content of SA (pH = 7) (B) on the surface of HRP@SPCs. The optical density of the reaction solution after 30 min of incubation was recorded at 650 nm.

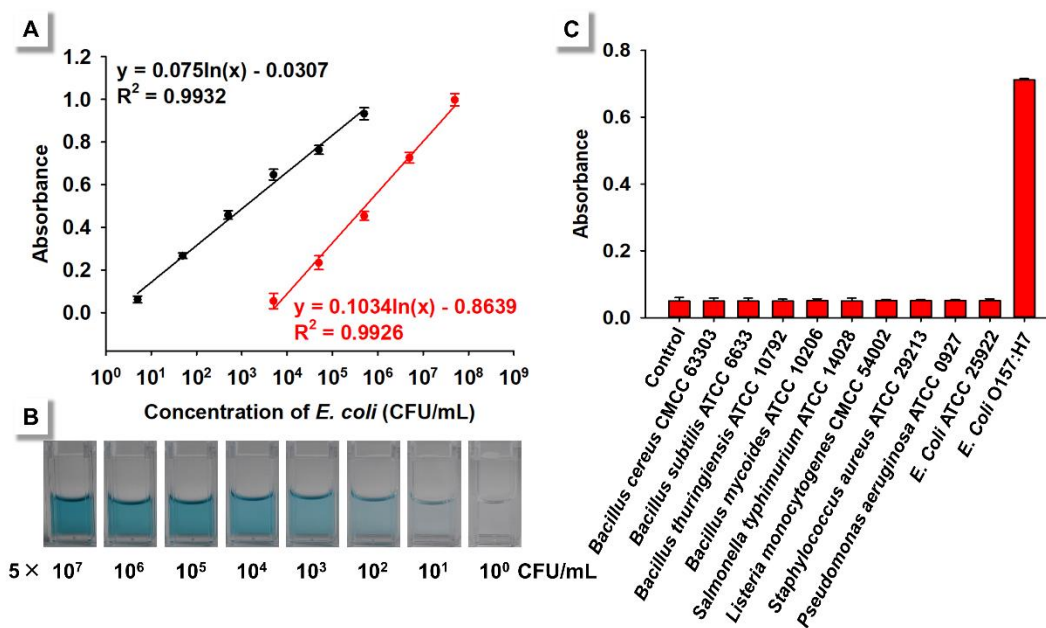


**Figure 13.** Performance of the SPC-based ELISA system on the detection of *Escherichia coli* O157:H7. **(A)** Calibration curves of HRP-based conventional ELISA (black line) and the proposed SPCs-based ELISA (red line). **(B)** Photos of the proposed HRP@PC-based ELISA in spiked PBS solution (0.01 M, pH 7.4) with different concentrations of *E. coli* O157:H7 ( $5 \times 10^0$  CFU/mL to  $5 \times 10^7$  CFU/mL). **(C)** Specificity of the proposed HRP@PC-based ELISA for other nontarget bacteria ( $1 \times 10^7$  CFU/mL). Each value represents the mean of three independent experiments (n=3). A negative control test was performed by adding a sterile PBS solution. The optical density of the reaction solution after 30 min of incubation was recorded at 650 nm.

**Table 2.** Checkerboard method for the concentration optimization of biotin@mAb and pAb.

Biotin@mAb ( $\mu\text{g/mL}$ )	pAb ( $\mu\text{g/mL}$ )					
	15	10	5	2.5	1.25	0.625
15	0.98	0.93	0.92	0.98	0.96	0.96
10	0.94	0.95	0.89	1.02	1.02	0.97
5	0.94	0.82	0.84	0.87	0.93	0.93
2.5	0.80	0.85	0.80	0.91	1.25	0.84
1.25	0.95	0.86	0.90	0.87	0.81	0.76
0.625	0.84	0.90	0.80	0.78	0.76	0.61

**Table 3.** Recoveries of *E. coli* O157:H7 spiked into milk detected by HRP@SPC-based ELISA.

Addition (CFU/mL)	Intra-assay precision			Inter-assay precision <sup>a</sup>		
	Mean <sup>b</sup>	Recovery (%)	CV (%)	Mean <sup>b</sup>	Recovery (%)	CV (%)
$1 \times 10^5$	$9.00 \times 10^4$	89.98	1.33	$9.57 \times 10^4$	95.66	6.60
$5 \times 10^4$	$4.15 \times 10^4$	82.98	0.48	$4.14 \times 10^4$	82.86	1.57
$1 \times 10^4$	$1.09 \times 10^4$	108.84	1.33	$9.03 \times 10^3$	90.30	17.94
$5 \times 10^3$	$5.32 \times 10^3$	106.37	2.17	$5.71 \times 10^3$	114.29	7.18
$1 \times 10^3$	$8.23 \times 10^2$	82.28	1.33	$8.43 \times 10^2$	84.30	3.42
$5 \times 10^2$	$4.17 \times 10^2$	83.35	7.26	$4.28 \times 10^2$	85.50	2.29

$1 \times 10^2$	$9.64 \times 10^1$	96.45	8.04	$1.16 \times 10^2$	116.27	14.89
$5 \times 10^1$	$4.18 \times 10^1$	83.53	2.20	$4.11 \times 10^1$	82.30	9.39

---

698 a, assay was completed every 1 days for 3 days continuously.

699 b, mean value of five replicates at each spiked concentration.

700

## 1.4 Conclusion

In this work, we used SPCs to encapsulate HRP or GOx to test the influence of nanoscale SPC encapsulation on the catalytic kinetics of HRP and GOx. The results indicate that the encapsulation can impact  $K_m$  and  $V_{max}$  of encapsulated enzymes, as well as significantly amplify the enzymes' catalytic signals. We then tested the protection ability of 500 nm SPCs for encapsulated HRP in harsh pH, NaCl, and trypsin conditions, as well as the storage stability. The stability study of HRP@SPCs and soluble HRP proved that SPCs could provide protection to packed enzymes in harsh conditions and increase the storage capability of HRP. Co-loaded GOx and HRP SPCs also exhibited superiority for cascade catalysis in biosamples. The ability of SPCs to enhance enzyme-based immunoassays was tested by establishing a HRP@SPC-based ELISA to detect *E. coli* O157:H7. SPC-based ELISA exhibited an approximately 280-fold improvement in detection sensitivity as compared with conventional ELISA. In summary, this work provides a systemic evaluation of 500 nm SPCs for enzyme immobilization and enhancing the detection performance of immunoassays.



## **2. Using Nanoflare for Live Cell Message RNA Imaging, Difference**

## **Between Inside and Outside of Endo/lysosome**

### **2.1 Introduction**

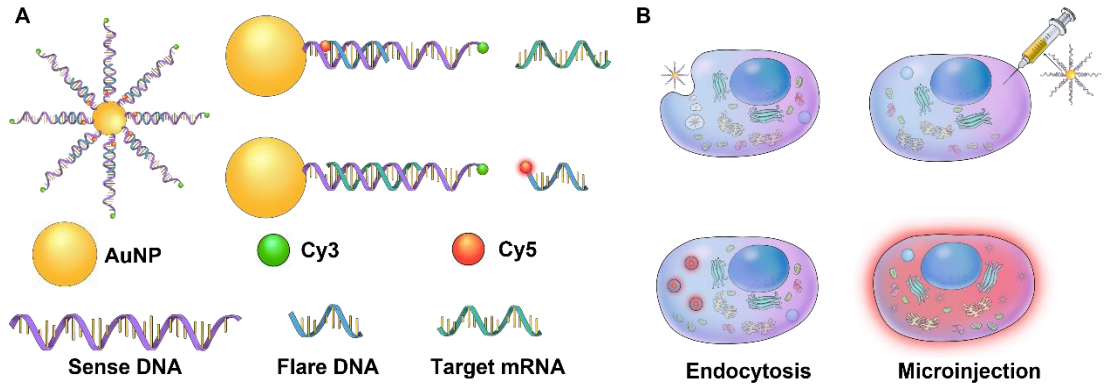
Rapid and precise visualization of gene expression provides rich information and valuable insights for disease diagnosis<sup>[54]</sup>, cancer therapy<sup>[55]</sup>, drug development<sup>[56]</sup>, and bioengineering<sup>[57]</sup>. RNA plays a key role in gene expression and regulation, in particular, message RNA (mRNA) is an important member of the RNA family<sup>[58]</sup>, which transfers genetic information from DNA to ribosomes to regulate protein synthesis<sup>[59]</sup>. Abnormal levels of mRNA are closely related to the occurrence and development of human diseases such as malignant tumors<sup>[60]</sup>. Therefore, in situ monitoring of mRNA could help to increase the understanding of their role and function in biological processes, thereby providing support for disease diagnosis and treatment<sup>[61]</sup>. However, mRNA itself does not emit specific signals, which has promoted the development of rationally constructed mRNA imaging probes for the purpose of specifically recognizing and illuminating intracellular mRNA. After more than forty years of development, a large number of advanced mRNA imaging techniques have been developed to in situ image mRNA in fixed and live cells<sup>[62]</sup>. Although imaging techniques for mRNA in fixed cells are well established, live cell mRNA imaging could advance the understanding of RNA working dynamics due to their excellent time resolution<sup>[63]</sup>. Recently, a variety of biosensors have been designed for live cell mRNA imaging including modified molecular beacons<sup>[64]</sup>, nanomaterials-enhanced nanobeacons<sup>[65]</sup> and nanoflares<sup>[66]</sup>. Among them, nanoflares have drawn incredible research and application interest in the past decade because the dense DNA on the surface of nanoparticle can enhance cellular uptake efficiency and resistance to nuclease degradation, and weaken the immunogenicity and cytotoxicity of nanoflare<sup>[67]</sup>.

In 2007, Prof. Dr. Chad Mirkin first reported the use of nanoflare as the tool to study mRNA in live cells<sup>[68]</sup>. Nanoflare is composed of a dense double-stranded DNA shell modified on the surface of AuNPs<sup>[69]</sup>. One of the DNA strands is the recognition strand and has base sequence complementary to the target mRNA. The other strand is usually modified with fluorophore. When

the flare strand and the recognition strand are combined, AuNPs can quench the fluorescence on the flare strand through Förster resonance energy transfer (FRET)<sup>[70]</sup>. Hybridization of the recognition strand to the target mRNA can displace the flare strand away from the surface of the AuNP and turn on fluorescence (**Scheme 2A**). As shown in **Scheme 2B**, traditional method is incubating nanoflare with live cells, the nanoflare could be internalized into live cells via cell endocytosis. Internalized nanoflares selectively recognize mRNA in live cells and release flare signals in situ for imaging. Although great progress has been made in situ imaging of mRNA in living cells by nanoflares, whether nanoflares can truly reflect mRNA level is still being questioned<sup>[71]</sup>. This is mainly because the internalization of nanoflares is achieved through endocytosis, but a large number of research results showed that the endocytic nanoflares were located in endo/lysosomes<sup>[72]</sup>. This means that without the introduction of an endosomal escape strategy, it is unclear how nanoflares enter the cytoplasm and enable the detection of mRNA. In fact, several studies in recent years have shown that nanoflares cannot truly reflect mRNA concentrations in living cells because endocytosed nanoflares are located in vesicular compartments in a subset of cells<sup>[73]</sup>.

Herein, we evaluated the working conditions of nanoflare in HeLa cells by endocytosis and microinjection. Unlike endocytosis, microinjection allows to directly inject nanoflare into cytoplasm resulting in the circumvention of endo/lysosome encapsulation<sup>[74]</sup>. In theory, the nanoflare internalized by endocytosis mainly aggregated in endo/lysosome, thus the released signals are also mainly in the trap of vesicles. On the contrary, injected nanoflares can be dispersed throughout the cell and thus enable selective release detection signals in the area of enriched mRNA (**Scheme 2B**). Therefore, we first observed nanoflare-exposed and nanoflare-injected HeLa cells. The results indicated that most of the detection signal was released by injected nanoflare aggregated at cell nucleus. Conversely, the detection signal released by endocytosed nanoflare can not diffuse into cell nucleus and disperse around the nucleus. Colocalization experiment showed that endocytosed nanoflare release detection signal predominantly in endo/lysosome. The further fluorescent intensity analysis results indicated that the injected nanoflare could release relatively stronger detection signals than endocytosed nanoflare at extremely low internalization concentrations. Accordingly, the working efficiency of endocytosed nanoflare were far lower than injected nanoflare. In addition, the investigation of control nanoflare showed that control nanoflare could not release detection

signal whether internalization by endocytosis or injection. Overall, the use of nanoflare for the imaging of mRNA in live cells strictly relies on the internalization pathways, in the other words, the escape of endo/lysosome encapsulation is the key factor for using nanoflare for mRNA imaging.



**Scheme 2.** A) The construction and working principles of nanoflare. B) Traditional incubation imaging model and microinjection-assisted imaging model.

## **2.2 Results and discussion**

### **2.2.1 Cell culture**

The culture with Human cervical cancer cells (HeLa cells) was cultured in Dulbecco's Modified Eagles Medium (DMEM, #11965092, Thermo Fisher) with 4.5 g/L glucose supplemented with 10% fetal bovine serum (FBS, Biochrom, Germany, #S0615), 5% penicillin/streptomycin (P/S, #15070063, Thermo Fisher Scientific) at 5% CO<sub>2</sub> and 37 °C.

### **2.2.2 Exposing nanoflare to HeLa cells**

30, 000 HeLa cells and nanoflare were dispersed into 2 mL of DMEM medium, the mixture was added to a 2.5 cm petri dish (I-bidi, #80136, 35 mm). Based on the experiment requirements, the concentration of nanoflare in the DMEM medium could be adjusted. The nanoflare-treated HeLa cells were incubated at 5% CO<sub>2</sub> and 37 °C for 18 h. After 18 h incubation, the dish was washed with PBS (0.01 M, pH 7.2-7.4) three times for removing the extra nanoflare. In order to identify the integrity of cells, nanoflare-exposed HeLa cells were stained by Hoechst 33342 (ThermoFisher, #62249) before imaging. The staining protocol could be found on ThermoFisher official website.

### **2.2.3 Injecting nanoflare into HeLa cells**

In order to achieve injection, HeLa cells were first seeded to a specific 2.5 cm petri dish (I-bidi, #80156, 35 mm, low grid-500). Unlike common petri dish, there are marked grids on the bottom of the specific dishes, which could help to locate the injected cells during imaging. To seed HeLa cells, 30, 000 HeLa cells were dispersed into 2 mL of DMEM medium, and the mixture was placed in a specific dish. These cells were incubated at 5% CO<sub>2</sub> and 37 °C for 18 h. After 18 h incubation, the dish was washed with PBS (0.01 M, pH 7.2-7.4) three times for removing suspending cells. The injection was performed by FemtoJet machine (Eppendorf) cooperating with microscope. The injection needles were purchased from Eppendorf, the internal diameter is 500 nm. The injection conditions were 110 hpa injection pressure, 54 hpa holding pressure, and 0.2 s injection time. Except for containing nanoflare, the injection solution also contains 5 mg/mL calcein for locating the

805 injected cells. The injected cells were placed at 37 °C for 10 min before imaging. After incipient  
806 imaging, these injected cells were then incubated at 5% CO<sub>2</sub> and 37 °C before next time imaging.

#### 807 **2.2.4 Imaging nanoflare exposed/injected HeLa cells**

808 Nanoflare injected/exposed HeLa cells were imaged by laser confocal scanning microscope  
809 (ZEISS LSM 880 mit Airyscan). For exposed cells, there should have three kinds of fluorescent  
810 dyes inside of HeLa cells including Cy5 on flare strand, Cy3 on target strand, and Hoechst 33342  
811 for cell nucleus staining. Thus, the imaging condition for nanoflare-exposed cells was set as Hoechst  
812 33342:  $\lambda_{\text{ex}} = 405 \text{ nm}$  and  $\lambda_{\text{em}} = 410\text{-}514 \text{ nm}$ ; cy3:  $\lambda_{\text{ex}} = 514 \text{ nm}$  and  $\lambda_{\text{em}} = 535\text{-}633 \text{ nm}$ ; cy5:  
813  $\lambda_{\text{ex}} = 633 \text{ nm}$  and  $\lambda_{\text{em}} = 637\text{-}759 \text{ nm}$ . For injection, there have also three kinds of fluorescent  
814 dyes inside of cells including Cy3, Cy5, and calcein. Therefore, the imaging conditions for  
815 injected HeLa cells were calcein:  $\lambda_{\text{ex}} = 488 \text{ nm}$  and  $\lambda_{\text{em}} = 493\text{-}556 \text{ nm}$ ; cy3:  $\lambda_{\text{ex}} = 514 \text{ nm}$  and  
816  $\lambda_{\text{em}} = 535\text{-}633 \text{ nm}$ ; cy5:  $\lambda_{\text{ex}} = 633 \text{ nm}$  and  $\lambda_{\text{em}} = 637\text{-}759 \text{ nm}$ .

#### 817 **2.2.5 Protocol for colocalization**

818 30,000 Hela cells were seeded in a petri dish with 2 mL of cell medium and then incubated at  
819 37 °C and 5% CO<sub>2</sub> for 18 h. Then the cells were stained by alexa fluor 488-labeled wheat germ  
820 agglutinin (WGA@Alexa fluor 488), lysotracker green, and Hoechst 33342. All of these dyes were  
821 purchased from ThermoFisher. The detailed stain protocol could fully refer to the protocols on  
822 ThermoFisher website. To stain nanoflare-treated cells, we used nanoflare-contained cell medium  
823 (0.1 nM) to culture Hela cells. Then, the cells were stained after three times washed with PBS (0.01  
824 M, pH 7.2~7.4) for further staining. Similarly, we used 0.2 nM nanoflare to inject the cultured cells,  
825 and then the injected cells were incubated 120 min for further staining. The stained cells were  
826 directly used to image (cy5:  $\lambda_{\text{ex}} = 633 \text{ nm}$  and  $\lambda_{\text{em}} = 638\text{-}759 \text{ nm}$ ; WGA@Alexa fluor 488:  $\lambda_{\text{ex}} =$   
827  $488 \text{ nm}$  and  $\lambda_{\text{em}} = 495\text{-}630 \text{ nm}$ ; lysotracker green:  $\lambda_{\text{ex}} = 561 \text{ nm}$  and  $\lambda_{\text{em}} = 566\text{-}628 \text{ nm}$ ; Hoechst  
828 33342:  $\lambda_{\text{ex}} = 405 \text{ nm}$  and  $\lambda_{\text{em}} = 410\text{-}495 \text{ nm}$ ). The Z-stack was started from bottom to top with  
829 0.79  $\mu\text{m}$  distance between each image.

## 2.2.6 The measurement protocol for fluorescent intensities of nanoflare exposed/injected cells

We used ImageJ to analyze the fluorescent intensities of the nanoflare exposed/injected cells<sup>[75]</sup>. Herein, we used an example to explain how we use ImageJ to analyze the fluorescent intensity. This example is 0.2 nM nanoflare and 0.5 mg/mL calcein co-injected HeLa cells. As shown in **Figure 14a**, light, cy3, cy5, and calcein field images were imported into ImageJ. The fluorescence of calcein could be used to point out the injected cells, then we can based on the light field draw out the outlines of cells with the freehand tool in ImageJ. Afterward, the cell outline was added to ROI manage system in ImageJ and saved for further use (**Figure 14b**). After obtaining all the outlines in one image, further analysis was performed and started by splitting the RGB channels of calcein, cy3, and cy5 field images (**Figure 14c**). Finally, the fluorescent intensities of cy3, cy5, and calcein in the image could be directly analyzed by the analysis tool in ImageJ (**Figure 14d**).

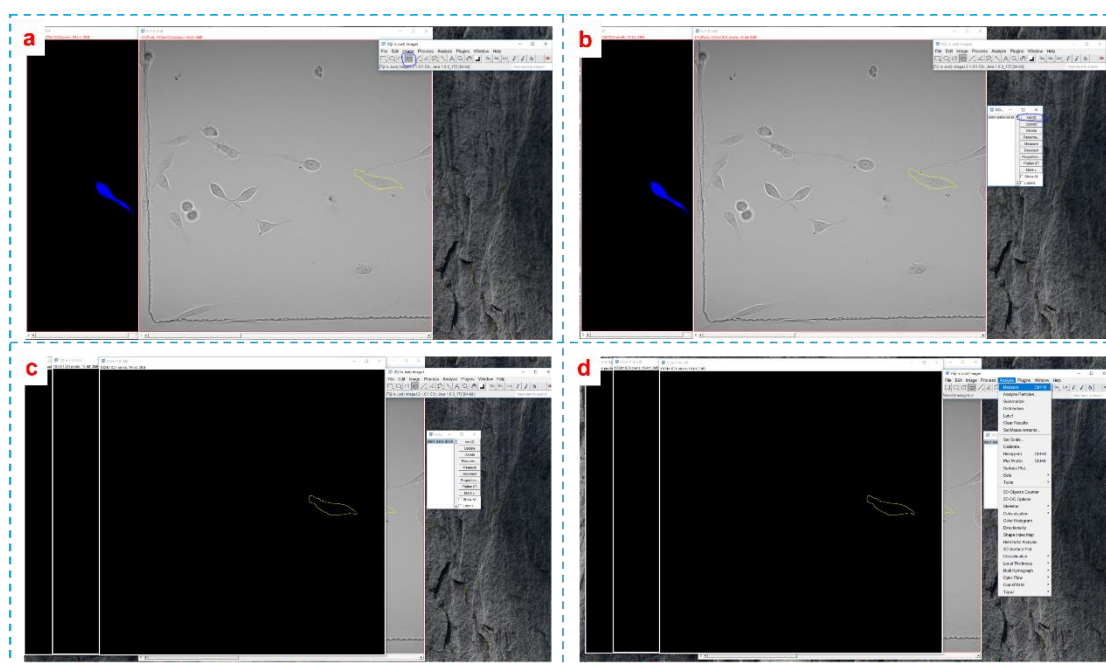


**Figure 14.** Analysis protocol for using ImageJ to measure fluorescent intensity of HeLa cells. A) First, using ImageJ to draw up the outline of cells. B) Second, adding the outline into ROI manage system. C) Third, using the saved ROI to point out the cells outline in the images which are needed to analyze. D) Forth, measuring the fluorescent intensities of pointed out cells.

## 2.3 Results and discussion

### 2.3.1 Proof of concept

A large number of researches have shown that nanoflare can achieve mRNA detection through incubating nanoflares with cells<sup>[76]</sup>, and the reports of introducing nanoflare through microinjection are still missing. Therefore, the sensing ability of injected nanoflare was first verified. We first prepared a injection solution contained 0.2 nM nanoflare and 0.5 mg/mL calcein. In this injection, calcein was used as a tracking dye to assist in localizing the injected cells and as the reference for ratiometric sensing. The injection solution was then injected into HeLa cells via FemtoJet machine (Eppendorf) with 110 hpa injection pressure, 54 hpa holding pressure, and 0.2 s injection time. After 10 min stabilizing, the injected cells were imaged via ZEISS LSM 880 mit Airyscan. The imaging conditions were calcein:  $\lambda_{\text{ex}} = 488 \text{ nm}$  and  $\lambda_{\text{em}} = 493\text{-}556 \text{ nm}$ , master gain: 500, cy3:  $\lambda_{\text{ex}} = 514 \text{ nm}$  and  $\lambda_{\text{em}} = 535\text{-}633 \text{ nm}$ , master gain 700; and cy5:  $\lambda_{\text{ex}} = 633 \text{ nm}$  and  $\lambda_{\text{em}} = 637\text{-}759 \text{ nm}$ , master gain 700. The images are shown in [Figure 15A](#), there were intense calcein signal could be observed, whereas no Cy3 and Cy5 signal could be detected. Afterward, the injected HeLa cells were incubated at 5% CO<sub>2</sub> and 37 °C. After 2 h incubation, the injected HeLa cells were then imaged at same condition again. The results in [Figure 15B](#) indicated that after 2 h incubation, the injected nanoflare released Cy5 signal without Cy3 signal. This suggested that the injection nanoflare could also detect mRNA in live HeLa cells.

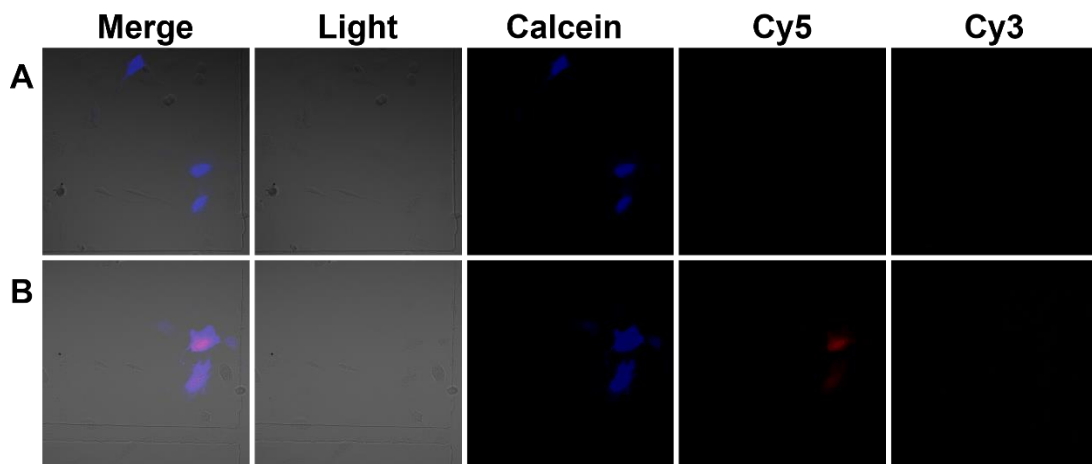


**Figure 15.** Images of injected HeLa cells. The injection solution contained 0.2 nM nanoflare and 0.5 mg/mL calcein. A) The images of the injected cells after injection 10 min. B) The images of injected cells. These images were taken after injection and then 2 h incubation.

### 2.3.2 Colocalization

During the proof of concept, we found that the Cy5 signal released by injected nanoflare was most aggregated in the cell nucleus. We therefore designed colocalization experiment to tracking the Cy5 signals in HeLa cells. Herein, Hoechst 33342 (ThermoFisher, #62249) was used for cell nucleus staining, WGA@Alexa fluor 488 (ThermoFisher, #W11261) was used for cell membrane staining, and lysotracker green DND-26 (ThermoFisher, #L7526 ) was used for lysosome staining. For cell staining, 30, 000 HeLa cells dispersed in 2 mL of DMEM medium were seeded in 2.5 cm petri-dish. The seeded HeLa cells were cultured at 5% CO<sub>2</sub> and 37 °C for 18 h. Subsequently, the cells were stained by Hoechst 33342, WGA@Alexa 488, and lysotracker green DND-26, orderly. The staining protocol could be found the website of ThermoFisher. The stained HeLa cells were then imaged via ZEISS LSM 880 mit Airyscan. The imaging conditions were Hoechst 33342:  $\lambda_{ex}$  = 405 nm,  $\lambda_{em}$  = 410-495 nm, master gain 600; WGA@Alexa fluor 488:  $\lambda_{ex}$  = 488 nm,  $\lambda_{em}$  = 495-630 nm, and master gain 700. cy5:  $\lambda_{ex}$  = 633 nm,  $\lambda_{em}$  = 638-759 nm, and master gain: 800; lysotracker green:  $\lambda_{ex}$  = 561 nm,  $\lambda_{em}$  = 566-628 nm, and master gain 600. The images of stained HeLa cells are shown in [Figure 16](#), the distance between each layer images was 0.79  $\mu$ m. Afterward, we further located the detection signals of endocytosed nanoflare. In this experiment, 30, 000 HeLa cells were seeded into 2 mL of DMEM with 0.1 nM nanoflare. After 18 h incubation, these cells were stained by Hoechst 33342 and WGA@Alexa fluor 488. The images of the stained cells in [Figure 17](#) suggested that the detection signals of endocytic nanoflares surround the peripheral of nucleus. The position of detection signal of endocytic nanoflare was further located through imaging Hoechst 33342, WGA@Alexa fluor 488, and lysotracker green DND-26 stained HeLa cells. As shown in [Figure 18](#), there has intense overlap between lysotracker green DND-26 signal and Cy5. The Cy5 signal of injected nanoflare was also located in HeLa cells. 0.2 nM nanoflare solution was injected into HeLa cells via FemtoJet machine (Eppendorf) with 110 hpa injection pressure, 54 hpa holding pressure, and 0.2 s injection time. As same as above, we prepared lysosome-unstained and



lysosome-stained cells. **Figure 18** and **19** demonstrated that most of injection nanoflare-released Cy5 signal were concentrated in the cell nucleus.

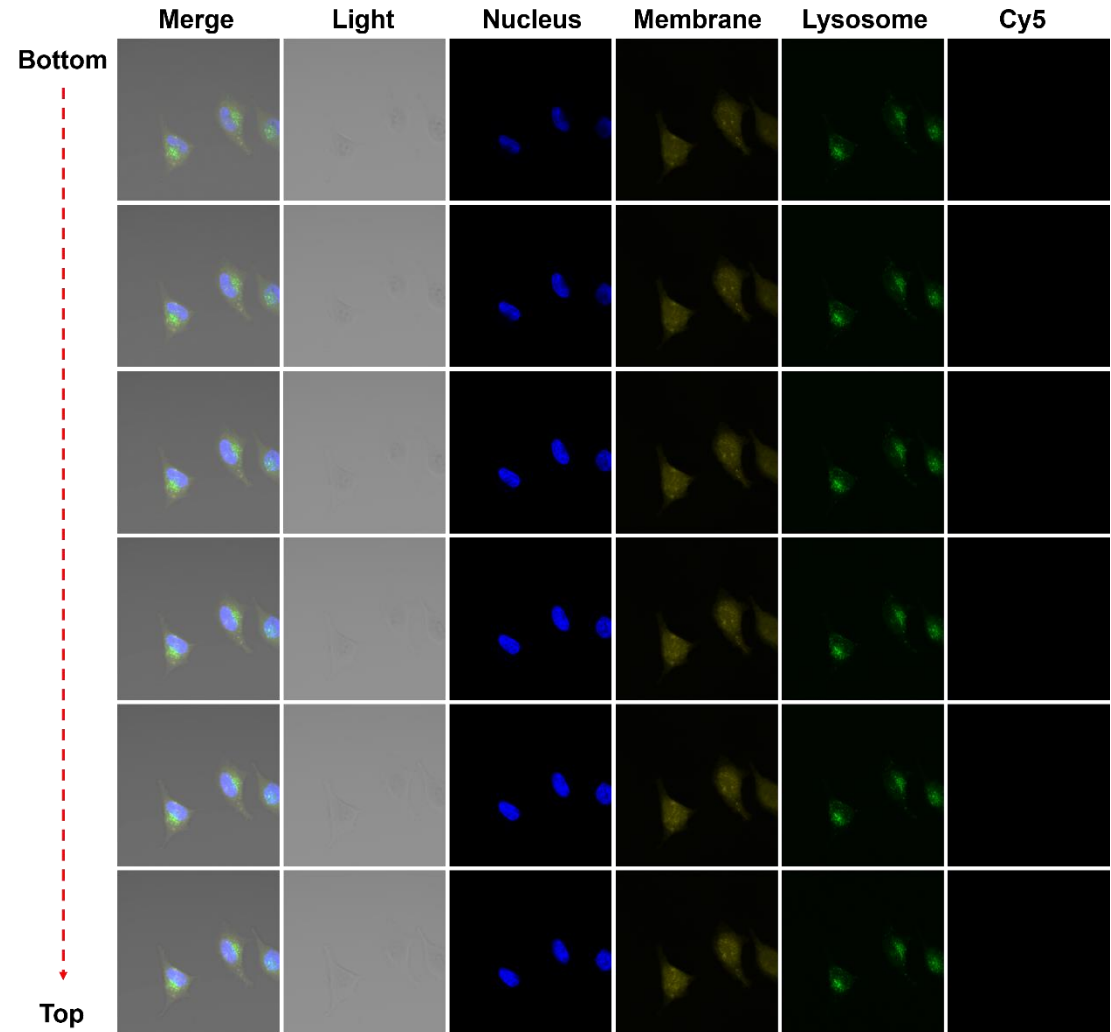


**Figure 16.** Cell staining reagents for HeLa cell staining. 30, 000 HeLa cells were added to a 2.5 cm petri dish with 2 mL of DMEM medium. These cells were incubated at 37 °C and 5% CO<sub>2</sub> for 24 h. Afterward, the cell medium was moved out and these cells were washed with PBS (0.01 M, pH 7.2~7.4) 2 times. After PBS washing, the cells were stained by Hoechst 33342, WGA Alexa fluor 488, and lysotracker green, orderly. The detailed stain protocols can be found on ThermoFisher website. The stained cells were imaged by two-photon machine, for the Z-stack, the z-distances were set as 0.79 μm per layer imaging.

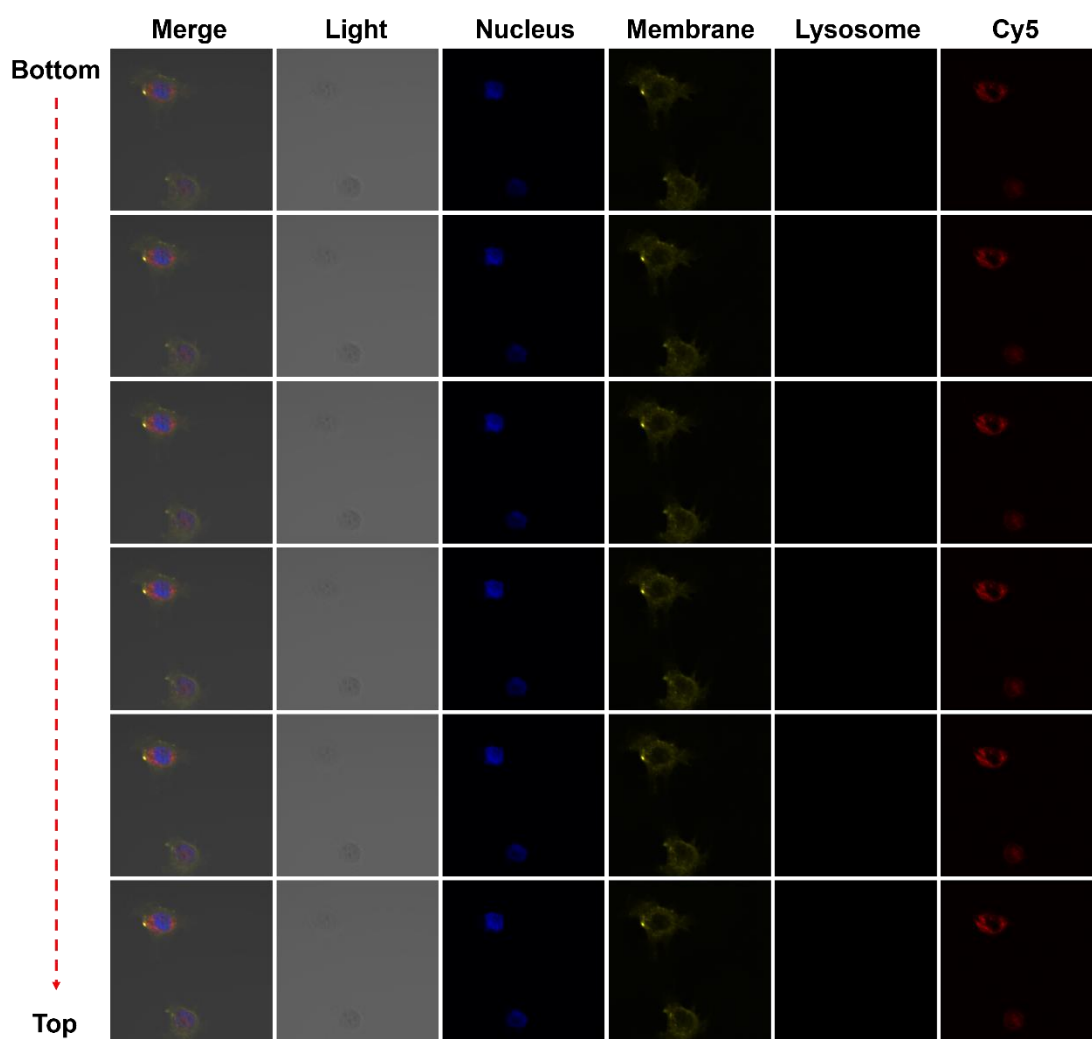


**Figure 17.** Images of nanoflare-exposed, Hoechst 33342 and WGA Alexa fluor 488-stained HeLa cells. 30, 000 HeLa cells were added to a 2.5 cm petri dish with 2 mL of DMEM medium. The DMEM medium contained 0.1 nM nanoflare. These cells were incubated at 37 °C and 5% CO<sub>2</sub> for 18 h. Afterward, the cell medium was moved out and these cells were washed with PBS (0.01 M, pH 7.2~7.4) 3 times. After PBS washing, the cells were stained by Hoechst 33342 and WGA@Alexa fluor 488, orderly. The stained cells were imaged by two-photon machine, for the Z-stack, the z-distances were set as 0.79 μm per layer imaging.

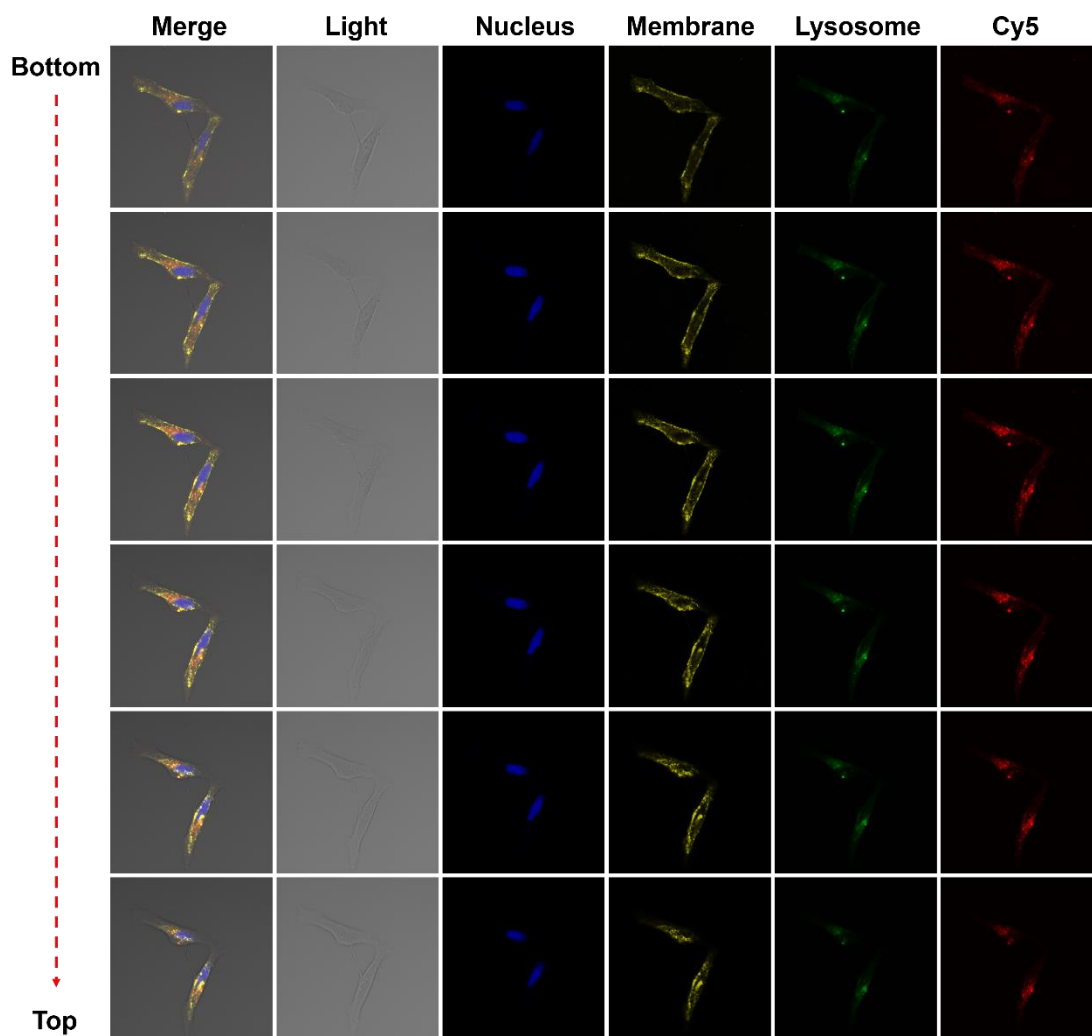
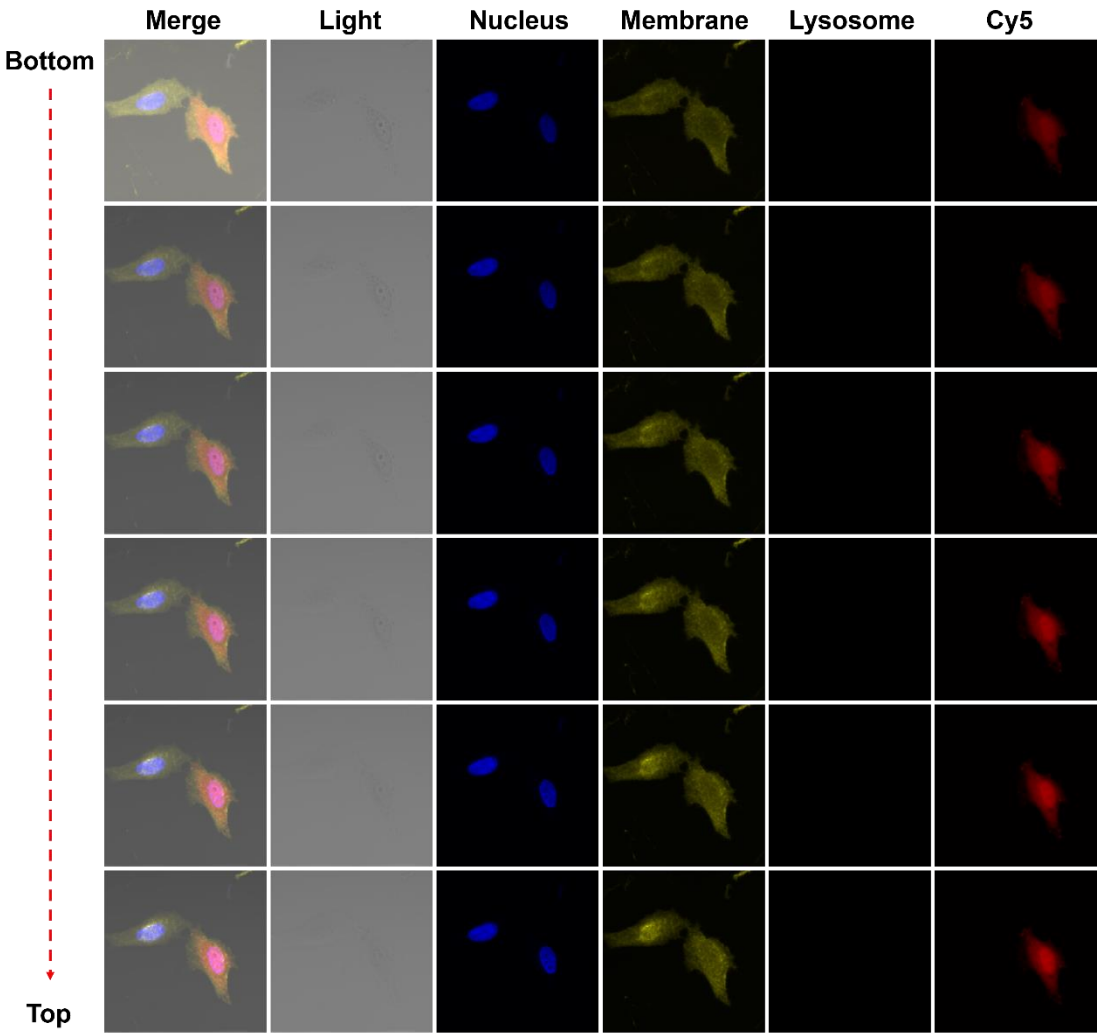


**Figure 18.** Images of nanoflare-exposed, Hoechst 33342, WGA Alexa fluor 488, and lysotracker green-stained HeLa cells. 30, 000 HeLa cells were added to a 2.5 cm petri dish with 2 mL of DMEM medium. The DMEM medium contained 0.1 nM nanoflare. These cells were incubated at 37 °C and 5% CO<sub>2</sub> for 18 h. Afterward, the cell medium was moved out and these cells were washed with PBS (0.01 M, pH 7.2~7.4) 3 times. After PBS washing, the cells were stained by Hoechst 33342, WGA@Alexa fluor 488, and lysotracker green, orderly. The stained cells were imaged by two-photon machine, for the Z-stack, the z-distances were set as 0.79 μm per layer imaging.



924

925 **Figure 19.** Images of nanoflare-injected, Hoechst 33342, and WGA Alexa fluor 488-stained HeLa  
926 cells. 30, 000 HeLa cells were added to a 2.5 cm petri dish with 2 mL of DMEM medium. These  
927 cells were incubated at 37 °C and 5% CO<sub>2</sub> for 18 h. Afterward, these cells were injected by 0.2 nM  
928 nanoflare (PBS buffer). Then, the injected HeLa cells were incubated 37 °C and 5% CO<sub>2</sub> for 2 h.  
929 After 2 h incubation, these cells were washed with PBS (0.01 M, pH 7.2~7.4) 3 times. The washed  
930 cells were further stained by Hoechst 33342 and WGA@Alexa fluor 488, orderly. The detail stain  
931 protocols can be found at ThermoFisher website. The stained cells were imaged by two-photon  
932 machine, for the Z-stack, the z-distances were set as 0.79 μm per layer imaging.

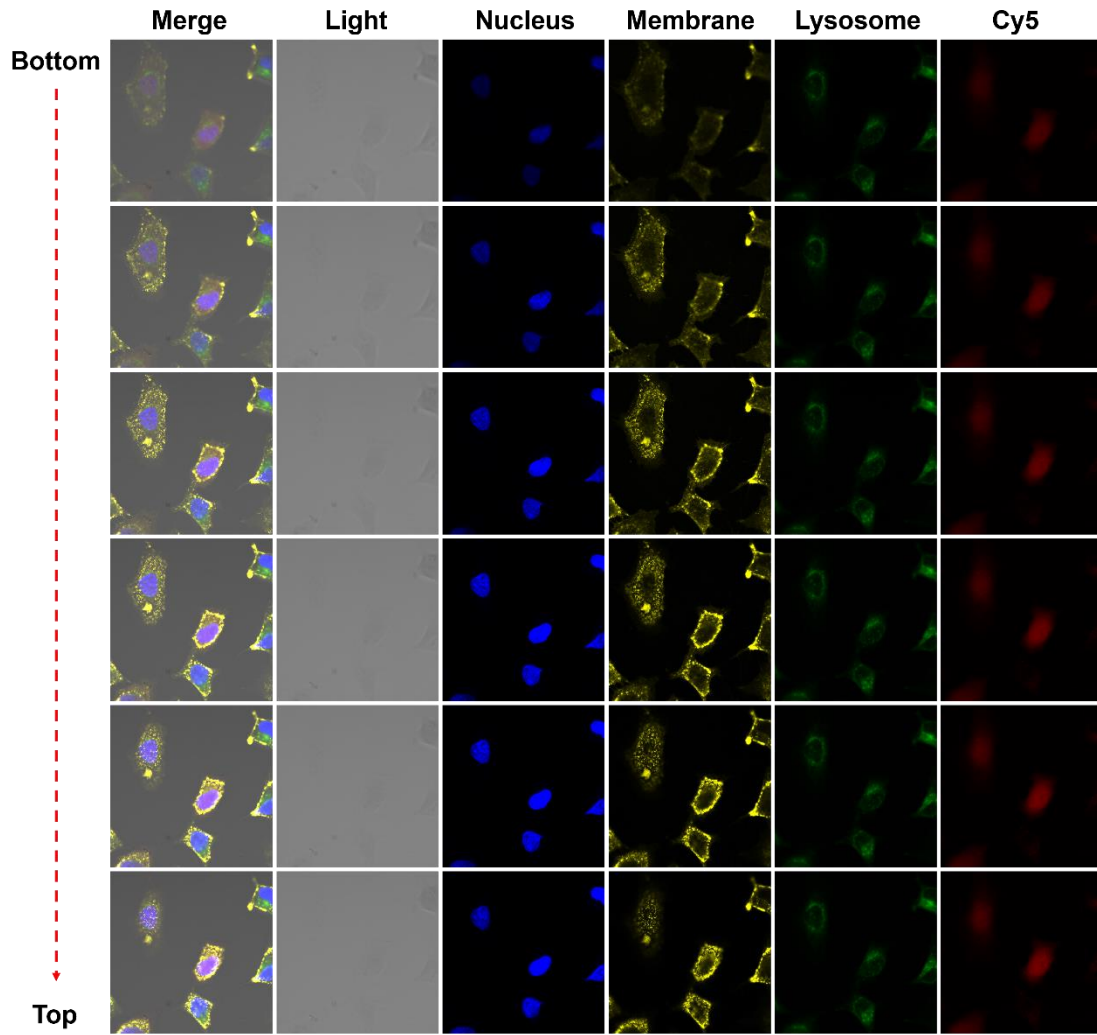


**Figure 20.** Images of nanoflare-injected, Hoechst 33342, WGA Alexa fluor 488, and lysotracker green-stained HeLa cells. 30,000 HeLa cells were added to a 2.5 cm petri dish with 2 mL of DMEM medium. These cells were incubated at 37 °C and 5% CO<sub>2</sub> for 18 h. Afterward, these cells were injected by 0.2 nM nanoflare (PBS buffer). Then, the injected HeLa cells were incubated 37 °C and 5% CO<sub>2</sub> for 2 h. After 2 h incubation, these cells were washed with PBS (0.01 M, pH 7.2~7.4) 3 times. The washed cells were further stained by Hoechst 33342, WGA@Alexa fluor 488, lysotracker green, orderly. The detail stain protocols can be found at ThermoFisher website. The stained cells were imaged by two-photon machine, for the Z-stack, the z-distances were set as 0.79 μm per layer imaging.

### 2.3.2 Comparison of nanoflare-based mRNA imaging by injection and incubation

On the basis of the above results, the pathways for nanoflare to enter HeLa cells could make a serious impact on mRNA imaging. In order to further estimate the difference of nanoflare imaging live cell mRNA between endocytosis and injection, we measured the intensities of cy5 fluorescent signal released from endocytosed and injected nanoflares. For achieving comparison, we used calcein as the contrast. Thus, the injection solution contained 0.5 mg/mL calcein and nanoflare. Similarly, we also injected 0.5 mg/mL calcein solution into nanoflare-exposed HeLa cells for ratiometric imaging. We first optimized detection time of injected nanoflare in HeLa cells. In the optimization, 0.2 nM nanoflare and 5 mg/mL calcein formed injection solution was injected HeLa cell through same injection condition mentioned on above. The results in **Figure 21A** indicated that the injected nanoflare could release the highest cy5 fluorescent signal after injection of 120 min. Thus, 120 min is the optimum detection time. After obtaining the optimum detection time, we further optimized the injection concentration. As shown in **Figure 21B**, the optimum injection concentration of nanoflare was 0.2 nM, at this condition, the fluorescent intensity of cy5 was  $1.3 \times 10^4$ . Meanwhile, we also measured the fluorescent intensity of cy5 from endocytosed nanoflare. For this, 30,000 HeLa cells were dispersed into 2 mL of DMEM cell medium and this medium contains 0.1 nM nanoflare. The nanoflare-exposed HeLa cells were incubated at 5% CO<sub>2</sub> and 37°C for 18 h. Afterward, these cells were injected with 0.5 mg/mL calcein and imaged after injection 10 min. The image in **Figure 21C** demonstrated that the cy5 fluorescent intensity of endocytosed nanoflare was approximately  $2.6 \times 10^3$ . In order to further evaluate whether the cy5 signal released by endocytosed nanoflare was derived from enzymatic degradation, we further prepared a control nanoflare. In theory, there is no mRNA can activate detection signal of control nanoflare. Subsequently, we exposed and injected control nanoflare into HeLa cells and the relevant fluorescent intensities of cy5 were also measured. Exposure and injection of controlled nanoflares were the same conditions as normal nanoflares. As summarized in **Figure 21C**, there were very weak cy5 signals could be detected in control nanoflare-treated HeLa cells. The ratios of cy5 and calcein were summarized in **Figure 21D**. The ratio of cy5 and calcein is approximately 0.35 for injected nanoflare, for endocytosis, the ratio is approximately 0.12. The results suggested that nanoflare by injection had relatively higher signal intensity than nanoflare by endocytosis and endocytosed nanoflare-released

cy5 signal came from the mRNA sensing. (The raw images are shown in [Figure 22 to 30](#)). In this section, all the cells were imaged by ZEISS LSM 880 mit Airyscan. The image conditions were calcein:  $\lambda_{\text{ex}} = 488 \text{ nm}$ ,  $\lambda_{\text{em}} = 493\text{-}556 \text{ nm}$ , master gain: 500; Cy3:  $\lambda_{\text{ex}} = 561 \text{ nm}$ ,  $\lambda_{\text{em}} = 562\text{-}624 \text{ nm}$ , master gain: 700; Cy5  $\lambda_{\text{ex}} = 633 \text{ nm}$ ,  $\lambda_{\text{em}} = 638\text{-}759 \text{ nm}$ , master gain: 700. The integration time was  $2.05 \mu\text{s}$ .

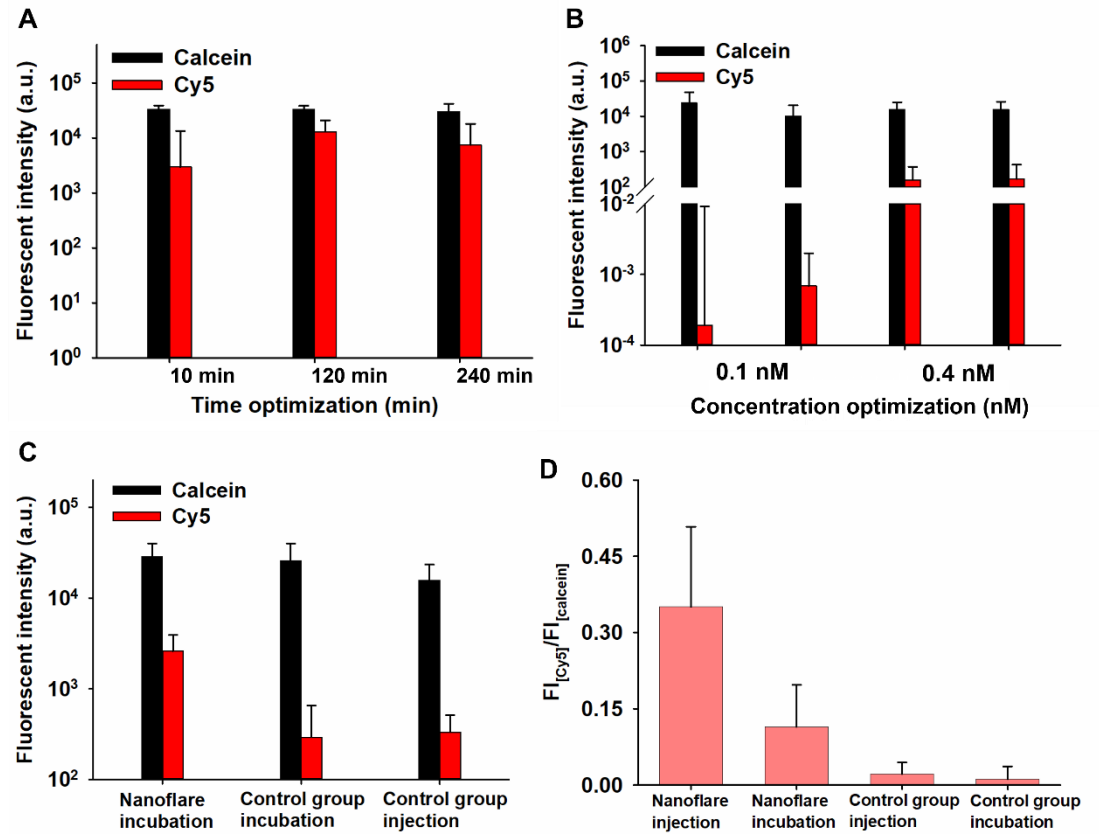


**Figure 21.** Fluorescent intensity analysis of nanoflare and control nanoflare-treated HeLa cells. A) 0.2 nM nanoflare and 0.5 mg/mL calcein co-injected HeLa cells. The fluorescent intensities of calcein and cy5 were measured after injection at 10 min, 120 min, and 240 min. B) 0.1 nM nanoflare and 0.4 nM nanoflare were respectively injected into HeLa cells. Both the two injection solution meantime contained nanoflare and 0.5 mg/mL calcein. The fluorescent intensities of calcein and cy5 were measured after injection at 10 min and 120 min. From left to right, the bars are 0.1 nM nanoflare injection after 10 min, 0.1 nM nanoflare injection after 120 min, 0.4 nM nanoflare injection after 10 min, and 0.4 nM nanoflare injection after 120 min. C) From left to right: fluorescent intensities of nanoflare-exposed and calcein-injected HeLa cells; control nanoflare-exposed and calcein-injection HeLa cells; control nanoflare and calcein co-injected HeLa cells. For

the control nanoflare, the exposure concentration was 0.1 nM, and the injection concentration was 0.2 nM. D) The ratios of cy5 and calcein of nanoflare and control nanoflare-treated HeLa cells. The error bars for the fluorescent intensities of nanoflare were calculated from 30 cells. The error bars for the fluorescent intensities of control nanoflare were calculated from 15 cells.

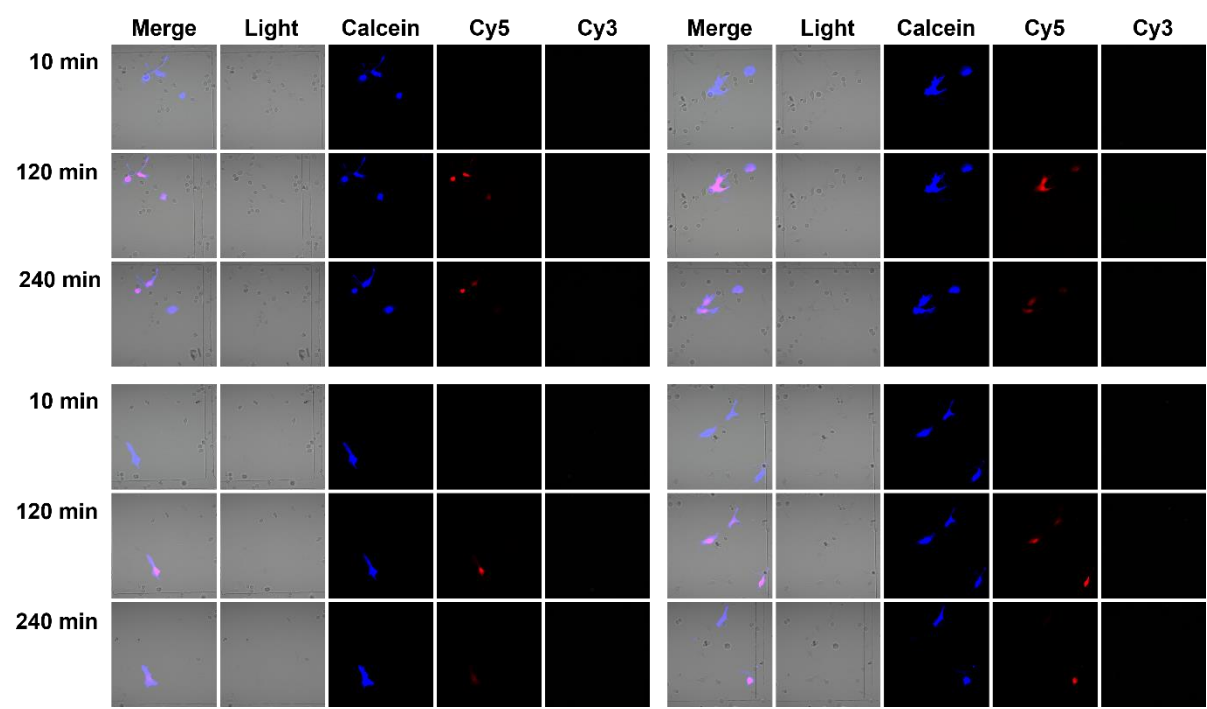


**Figure 22.** Images of injected HeLa cells, the injection solution contained 0.2 nM nanoflare and 5 mg/mL calcein.

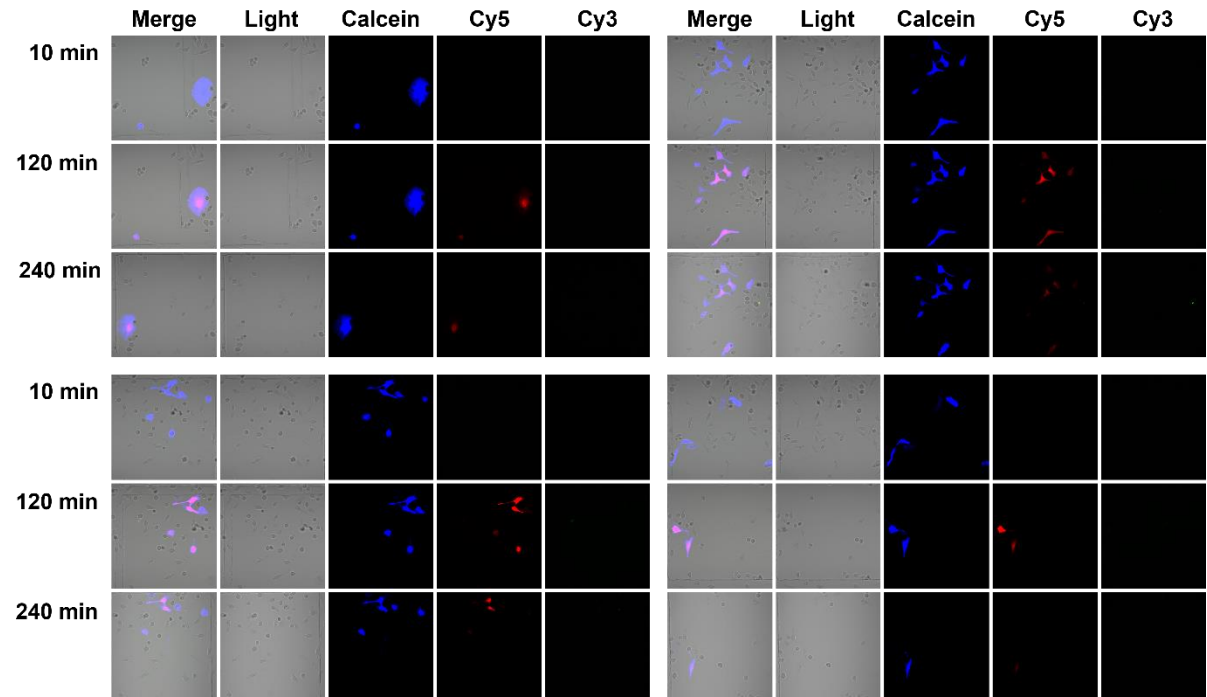




**Figure 23.** Images of injected HeLa cells, the injection solution contained 0.2 nM nanoflare and 5 mg/mL calcein.

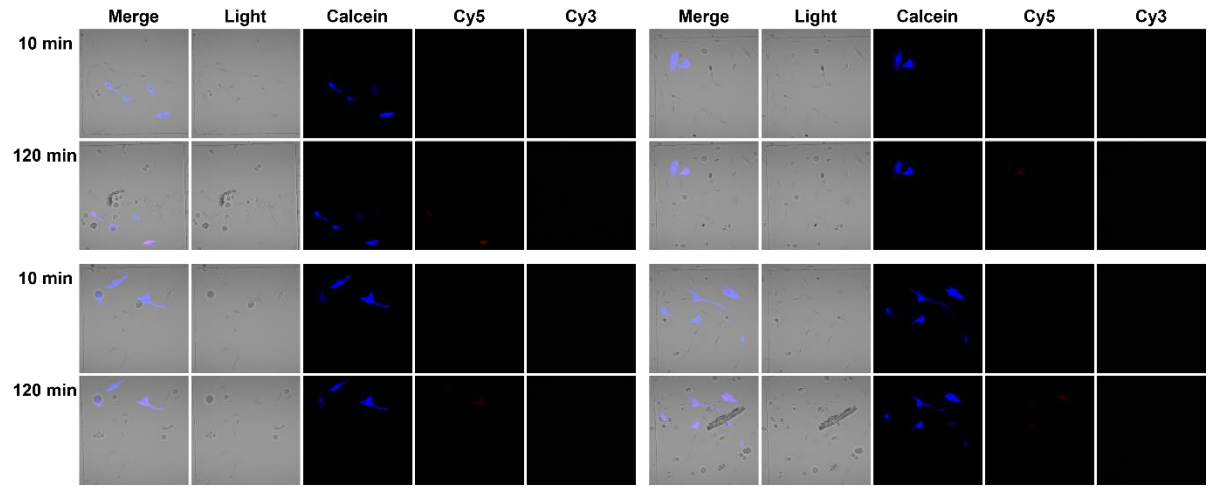


**Figure 24.** Images of injected HeLa cells, the injection solution contained 0.1 nM nanoflare and 5 mg/mL calcein.

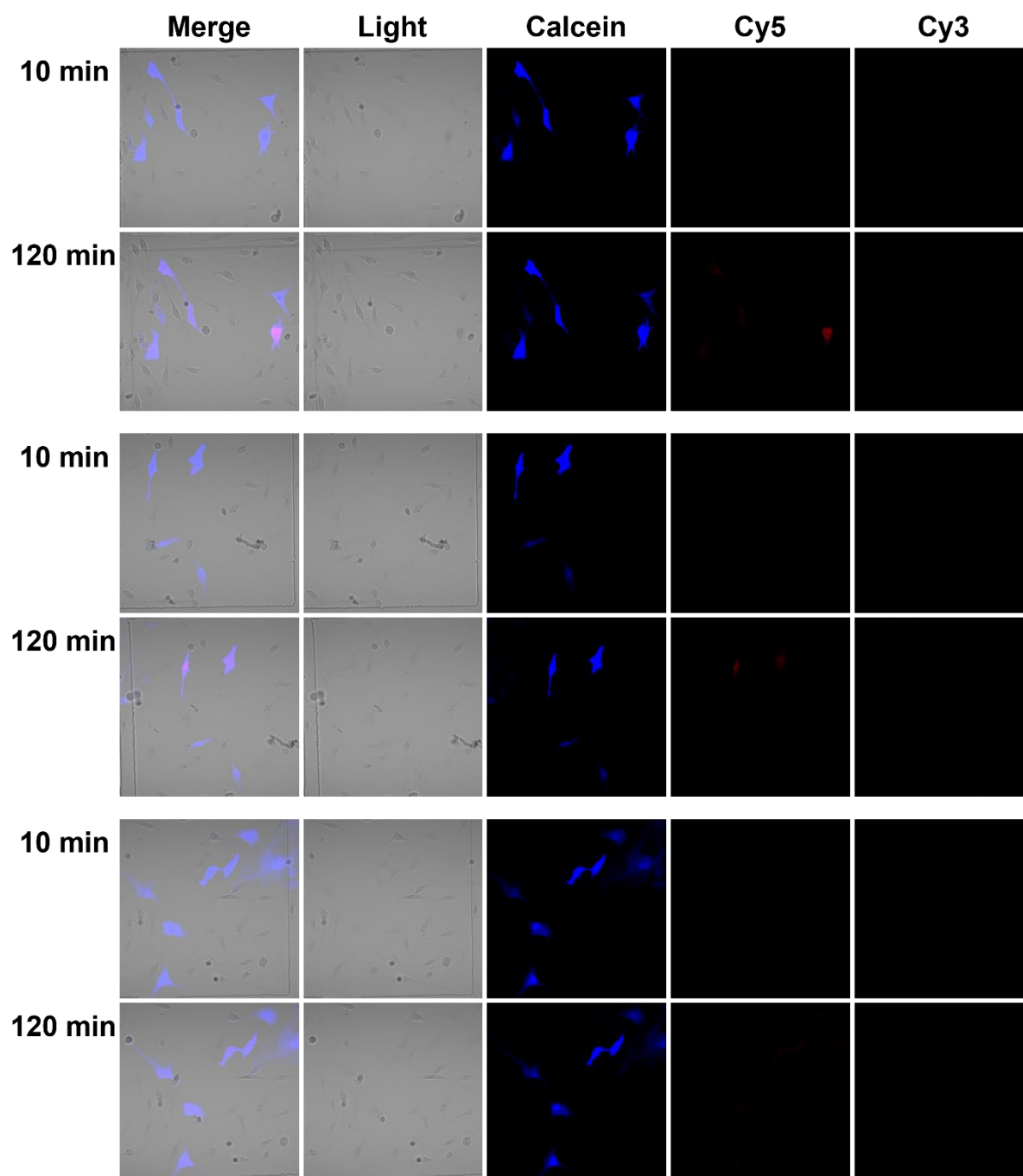


**Figure 25.** Images of injected HeLa cells, the injection solution contained 0.1 nM nanoflare and 5 mg/mL calcein.

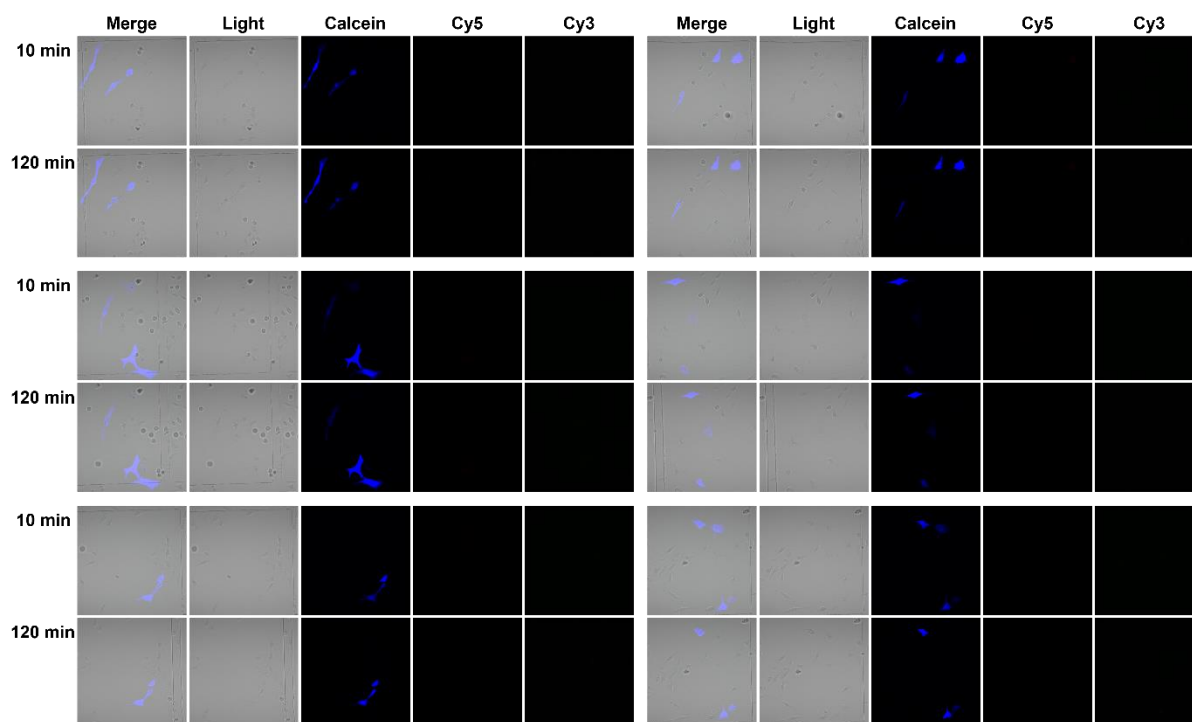


**Figure 26.** Images of injected HeLa cells, the injection solution contained 0.4 nM nanoflare and 5 mg/mL calcein.

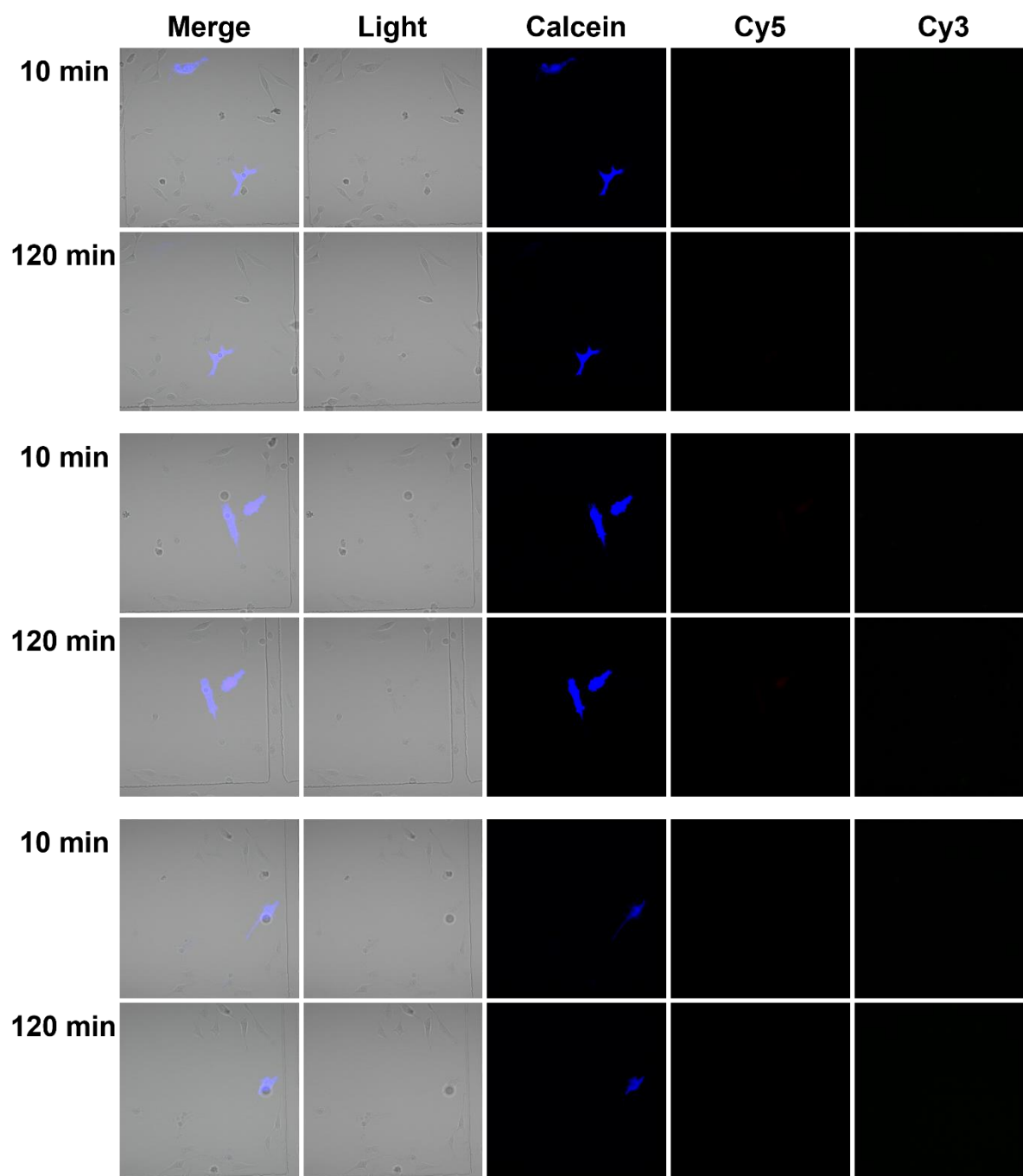


**Figure 27.** Images of injected HeLa cells, the injection solution contained 0.4 nM nanoflare and 5 mg/mL calcein.

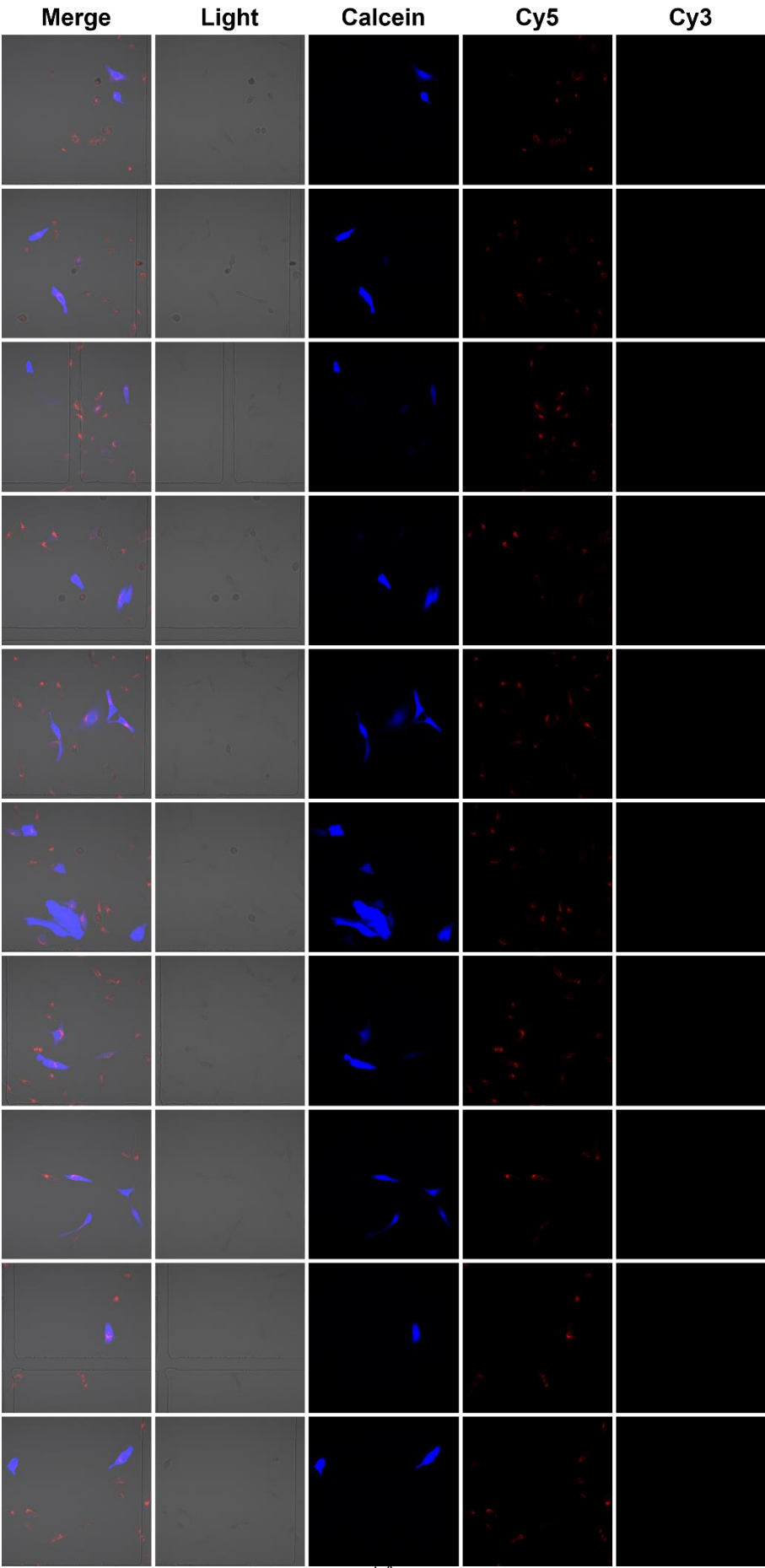


**Figure 28.** Images of HeLa cells, which first incubated with nanoflare, and then injected by calcein. The incubation concentration of nanoflare was 0.1 nM, the injection concentration of calcein was 5 mg/mL.

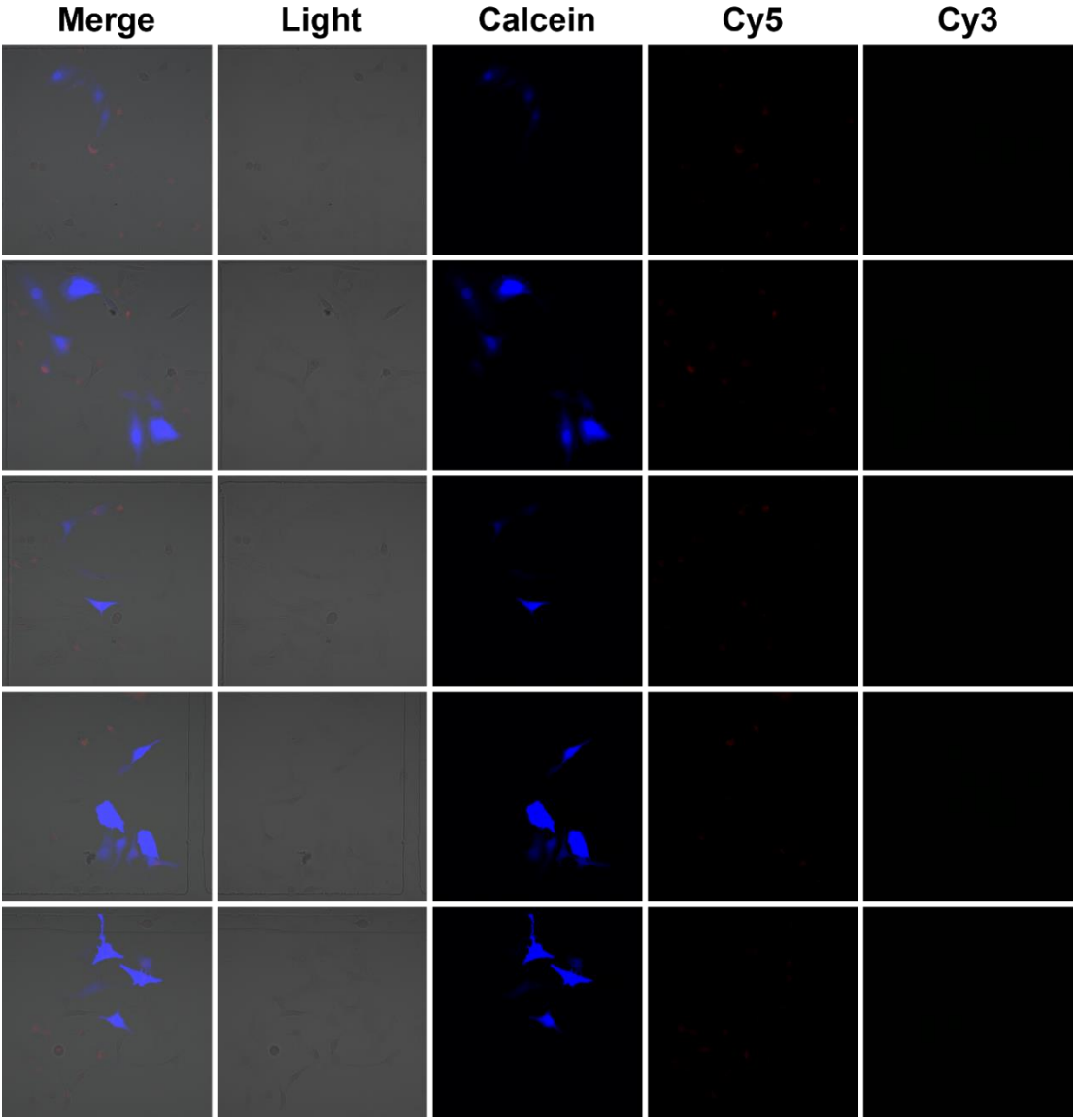


**Figure 29.** Images of HeLa cells, which first incubated with control nanoflare, and then injected by calcein. The incubation concentration of nanoflare was 0.1 nM, the injection concentration of calcein was 5 mg/mL.

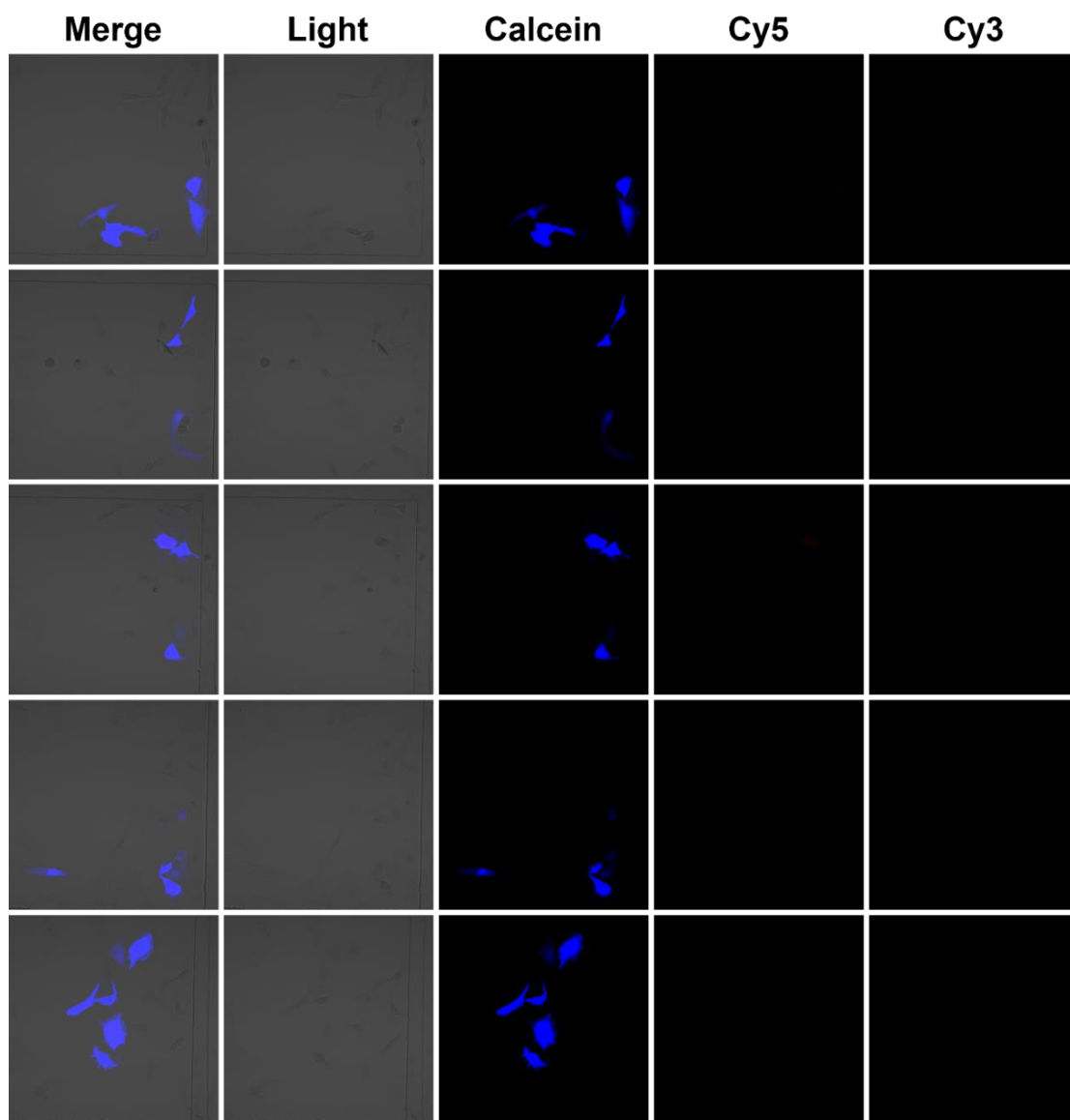


**Figure 30.** Images of injected HeLa cells, the injection solution contained 0.2 nM control nanoflare and 5 mg/mL calcein.

### 2.3.3 The amount of nanoflare in per cell by endocytosis

We first measured the Au mass in one nanoflare. 100  $\mu$ L of 6 nM, 3 nM, 1.5 nM, 0.75 nM, and 0.375 nM nanoflare solutions were prepared. Then, 200  $\mu$ L of freshly prepared aqua regia solutions were respectively added to these nanoflare solutions. After 24 h digestion, 1700  $\mu$ L of freshly prepared Milli-Q water was added to digested solution to a final volume of 2 mL. These samples were directly used to measure the total Au mass by ICP-MS (Agilent technologies 7700 series) without other treatments. The Au mass per nanoflare is calculated through the process:

1. The amount of nanoflare

$$q_{nanoflare} = v_{nanoflare} \times c_{nanoflare} \times NA$$

$q_{nanoflare}$  is the amount of nanoflare;

$v_{nanoflare}$  is the volume of nanoflare solution;

$c_{nanoflare}$  is the concentration of nanoflare solution;

NA is the avogadro's constant.

2. The total Au mass in nanoflare solutions

$$m_{Au} = c_{Au} \times v_{measurement}$$

$m_{Au}$  is the total Au mass in the nanoflares solution;

$c_{Au}$  is the Au concentration measured by ICP-MS;

$v_{measurement}$  is the measurement volume, in this experiment, this volume is 2 mL.

The Au mass of a single nanoflare ( $m_{Au/nanoflare}$ ) is obtained by dividing the total amount of nanoflare by the total Au mass.

**Table 4.** Calculation and summary

$C_{nanoflare}$ (nM)	6	3	1.5	0.75	0.375
$V_{nanoflare}$ (μL)	100				
Total mole of nanoflare (mole)	$0.6 \times 10^{-12}$	$0.3 \times 10^{-12}$	$1.5 \times 10^{-13}$	$0.75 \times 10^{-13}$	$3.75 \times 10^{-14}$
NA	$6.02 \times 10^{23}$				
$q_{nanoflare}$	$3.61 \times 10^{11}$	$1.81 \times 10^{11}$	$9.03 \times 10^{10}$	$4.52 \times 10^{10}$	$2.26 \times 10^{10}$
$c_{Au}$ (ng/mL)	548.72	292.13	138.78	62.31	29.91
$v_{measurement}$ (mL)	2				
$m_{Au}$ (ng)	1097.44	584.26	277.56	124.62	59.82
$m_{Au/nanoflare}$ (ng)	$3.04 \times 10^{-9}$	$3.22 \times 10^{-9}$	$3.07 \times 10^{-9}$	$2.76 \times 10^{-9}$	$2.65 \times 10^{-9}$
Mean (ng)	$2.81 \pm 0.24 \times 10^{-9}$				

For measurement of nanoflare in HeLa cells, 30, 000 HeLa cells were seeded into 2 mL of DMEM medium with 0.1 nM nanoflare. The seeded HeLa cells were cultured at 5% CO<sub>2</sub> and 37 °C



for 18 h. After 18 h incubation, the supernatant was collected and the volume was constant to 2 mL by DMEM. And then, 200 µL of the diluted supernatant was digested by 200 µL of aqua regia for 24 h. 1600 µL of Milli-Q water was added to the digested supernatant to 2 mL final volume. Finally, Au concentration in this solution was measured by ICP-MS. The adsorbent cells were treated by 300 µL of trypsin-EDTA (ThermoFisher, #25200056) for 3 min. The condition of cells was observed by common optical microscope (Carl Zeiss, primovert) to insure that all the cells left the bottom of the dish. Then 2 mL of DMEM was added to the dish to terminate the trypsin catalytic reaction. Afterward, the cells were collected by centrifugation and suspended into 200 µL of DMEM. The concentration of the cells was measured by cell counting method without modification. After obtained the cell concentration, 200 µL of aqua regia solution was added to the cell solution and digested for 24 h. 1600 µL of Milli-Q water was added to the digested solution to the final volume to 2 mL. This solution was then directly measured by ICP-MS without other treatment. This measurement was repeated 7 times. The amount of nanoflare in per HeLa cells is calculated through below process:

1. Calculating cell amount

$$q_{cell} = c_{cell} \times v_{cell}$$

$q_{cell}$  is the amount of cells;

$c_{cell}$  is the concentration of cell solution;

$v_{cell}$  is the volume of cell solution.

2. Calculating Au mass in cell solution

$$m_{Au(cell)} = c_{Au(cell)} \times v_{measurement}$$

$m_{Au(cell)}$  is the total Au mass in cell solution;

$c_{Au(cell)}$  is the Au concentration of the ICP-MS measured treated cell sample.

3. Amount of nanoflare in per cells

$$q_{nanoflare/cell} = m_{Au(cell)} \div m_{Au/nanoflare} \div q_{cell}$$

$q_{nanoflare/cell}$  is the amount of nanoflare in per cell.

**Table 5.** Calculation and summary

Group	1	2	3	4	5	6	7
Conc. (Au,	13.13	15.62	13.77	14.61	16.44	15.59	15.86

supernatant, ng/mL)							
$c_{\text{cell}}$ (/mL)	$2.7 \times 10^5$	$2.1 \times 10^5$	$2.1 \times 10^5$	$2.3 \times 10^5$	$2.6 \times 10^5$	$2.5 \times 10^5$	$2.2 \times 10^5$
$v_{\text{cell}}$ ( $\mu\text{L}$ )	200 $\mu\text{L}$						
$q_{\text{cell}}$	$5.4 \times 10^4$	$4.2 \times 10^4$	$4.2 \times 10^4$	$4.6 \times 10^4$	$5.2 \times 10^4$	$5.0 \times 10^4$	$4.4 \times 10^4$
$c_{\text{Au(cell)}}$ (ng/mL)	1.27	1.52	1.71	1.59	1.72	1.62	1.08
$V_{\text{measurement}}$ (mL)	2						
$m_{\text{Au(cell)}}$ (ng)	2.54	3.04	3.42	3.18	3.44	3.24	2.16
$q_{\text{nanoflare(cell)}}$	$0.90 \times 10^9$	$1.08 \times 10^9$	$1.22 \times 10^9$	$1.13 \times 10^9$	$1.22 \times 10^9$	$1.15 \times 10^9$	$0.77 \times 10^9$
$q_{\text{nanoflare/cell}}$	$1.7 \times 10^4$	$2.6 \times 10^4$	$2.9 \times 10^4$	$2.5 \times 10^4$	$2.3 \times 10^4$	$2.3 \times 10^4$	$1.8 \times 10^4$
Average and SD	$1.61 \pm 0.43 \times 10^4$						

Note: Au is undetectable in Aqua regia and Milli-Q water by ICP-MS.

### 2.3.4 Amount of nanoflare in HeLa cells by injection

#### Method 1

Except for the endocytosed amount of nanoflare, the amount of nanoflare in HeLa cells by injection was also evaluated. In order to evaluate the injection amount, we have to know the injection volume first. Therefore, we here used two methods to measure the volume per time injection. For method 1, we used calcein as the fluorescent mark to track the injection volume because calcein has a relative high fluorescence quantum yield and stable fluorescent intensity at PBS (0.01 M, pH 7.4). We need to establish a calibration curve of fluorescent intensity and concentration of calcein. We first prepared a series of standard calcein solutions, and then the fluorescence spectra of these standard calcein solutions were measured by Fluorolog-3 (Jobin Yvon Inc.) (Figure 31A). Subsequently, the fluorescent intensity at 525 nm of these spectra was used to establish calibration curve. As shown in Figure 31B, the calibration curve is  $y = 2136.8x - 32275$ ,  $R^2 = 0.9953$ . After

obtaining the calibration curve, a 100 mg/mL calcein solution (0.01 M, pH 7.4) was injected into 1 mL of PBS solution (0.01 M, pH 7.4) for 500 times. The injection condition as same as the injection of nanoflare. Afterward, the 1 mL of injected PBS solution was collected and used Fluorolog-3 to measure the fluorescence spectrum (Figure 31C). This injection was repeated six times, the repetitions were termed as batch 1 to 6. The fluorescent intensity at 525 nm of the injected solution was used to calculate the concentration of calcein in the injected PBS solution. Combing with the concentration of injection solution and injection times, the injection volume could be calculated. The injection volume per time injection is summarized in Figure 31D.

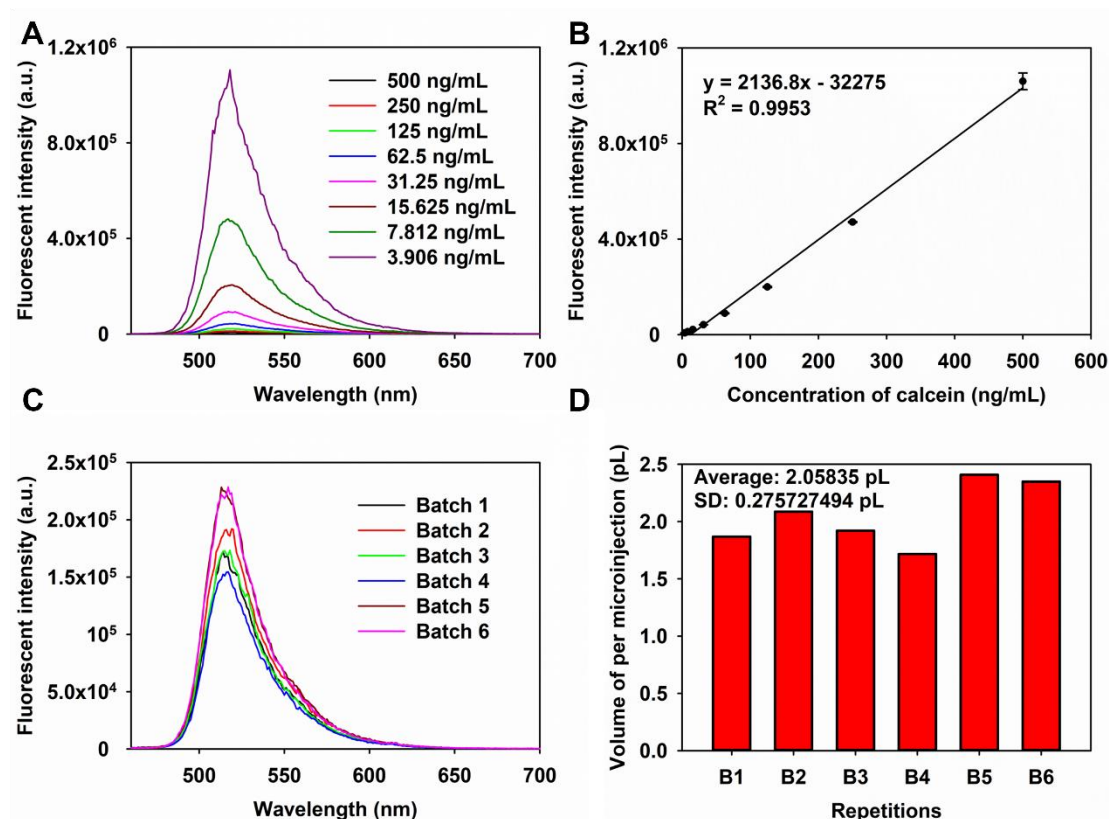


**Figure 31.** The measurements of injection volume by method 1. a) The fluorescence spectrum of standard calcein solution. b) The calibration curve of fluorescent and concentration of calcein, the fluorescent intensity at 515 nm was selected to establish the curve; c) The fluorescence spectrum of 100 mg/mL calcein injected PBS solution. d) The calculated volume per time injection. The measurement of injection volume.

## Method 2

Except for the indirect method, the injection volume could also be estimated by injecting water into mineral oil and then measuring the volume of water drop inside of oil. In this method, the shape of water drop was assumed as spherical. We first dropped a mineral oil on the glass plate. Then, the injection needle filled by water was sucked into the oil. After 100 times injections, we slowly moved the needle out of the water drop and waited for the droplet to reform into sphere. The diameters of the droplets could be measured by the scalebar in the image. The volume per injection droplet could be calculated by a typically calculation formula for sphere. The detailed injection condition is shown in [Figure 32A](#), the formed water drops were showed in [Figure 32B](#). For this method, we need to measure the length of bar, and then based on the bar measure the diameters of the water drops. Then, the volume could be calculated by volume formula of sphere. The calculated results as summarized in [Table 5](#), the injection volume measured by method 2 is  $0.74 \times 10^{-12}$  L.

Calculation process:

The volume of droplet based on the formula:

$$v_{droplet} = 4 \div 3 \times \pi \times R^3$$

$$R = L_{droplet} \div L_{bar} \times 20 \div 2$$

$v_{droplet}$  is the volume of per droplet;

R is the radius of the droplet;

$L_{droplet}$  is the length of droplet in the [Figure 32B](#);

$L_{bar}$  is the length of bar in the [Figure 32B](#).

**Table 6.** Calculation and summary.

Item	Droplet 1	Droplet 1	Droplet 1	Droplet 1	Droplet 1	Droplet 1
$L_{droplet}$	0.21	0.22	0.20	0.19	0.22	0.28
$L_{bar}$	0.86					
$V_{droplet}$	$6.09 \times 10^{-11}$	$7.01 \times 10^{-11}$	$5.27 \times 10^{-11}$	$4.51 \times 10^{-11}$	$7.01 \times 10^{-11}$	$12.49 \times 10^{-11}$
Injection time	100					
Injection volume	$0.61 \times 10^{-12}$	$0.70 \times 10^{-12}$	$0.53 \times 10^{-12}$	$0.45 \times 10^{-12}$	$0.70 \times 10^{-12}$	$1.25 \times 10^{-12}$
Average and SD (L)	$0.74 \pm 0.36 \times 10^{-12}$					

**Note:** The length of the bar and R of injection drop were measured by Powerpoint.

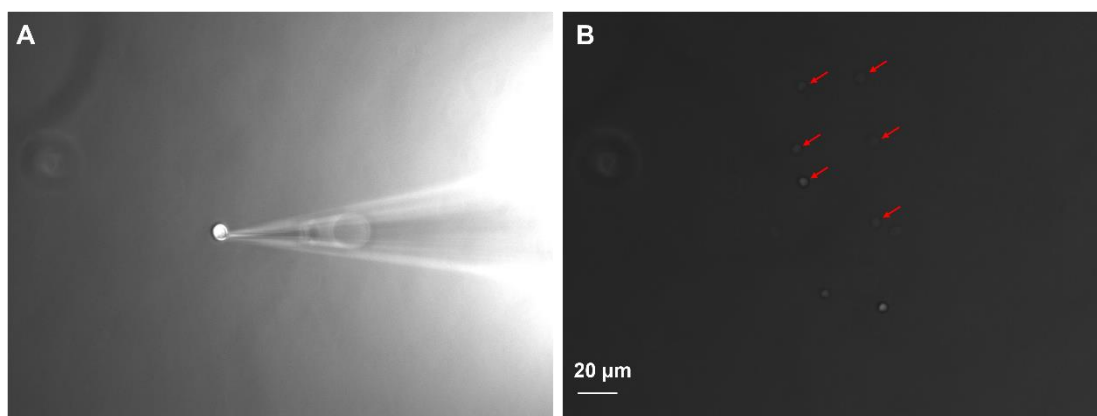


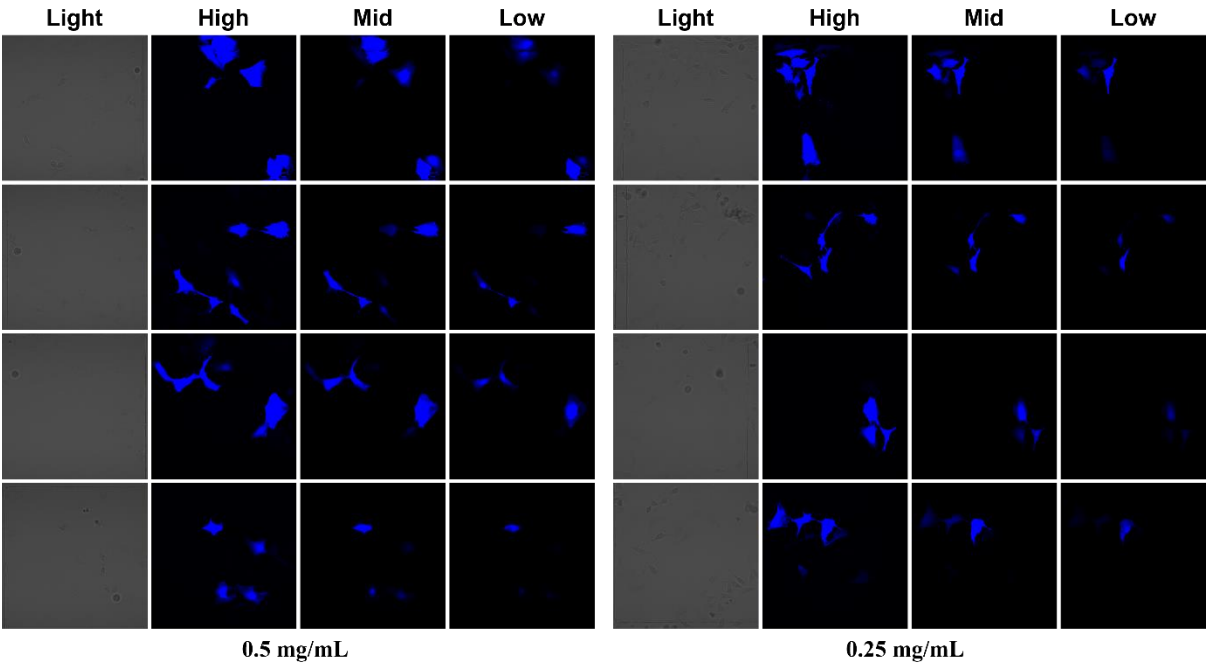
**Figure 32.** The measurements of injection volume by method 2. A) The real-time image during the injection. B) The injection droplets after removing injection needle. Red rolls were used for marking droplets out. Bar is 20  $\mu\text{m}$ .

After obtaining the volume per time injection, the amount of nanoflare in injected HeLa cells is estimated  $0.412 \pm 0.056 \times 10^{-21}$  and  $0.148 \pm 0.072 \times 10^{-21}$  mole. The number of smartflare per cell could calculate by plus the moles with Avogadro constant:  $2.48 \pm 0.33712 \times 10^2$  and  $0.89096 \pm 0.43344 \times 10^2$ .

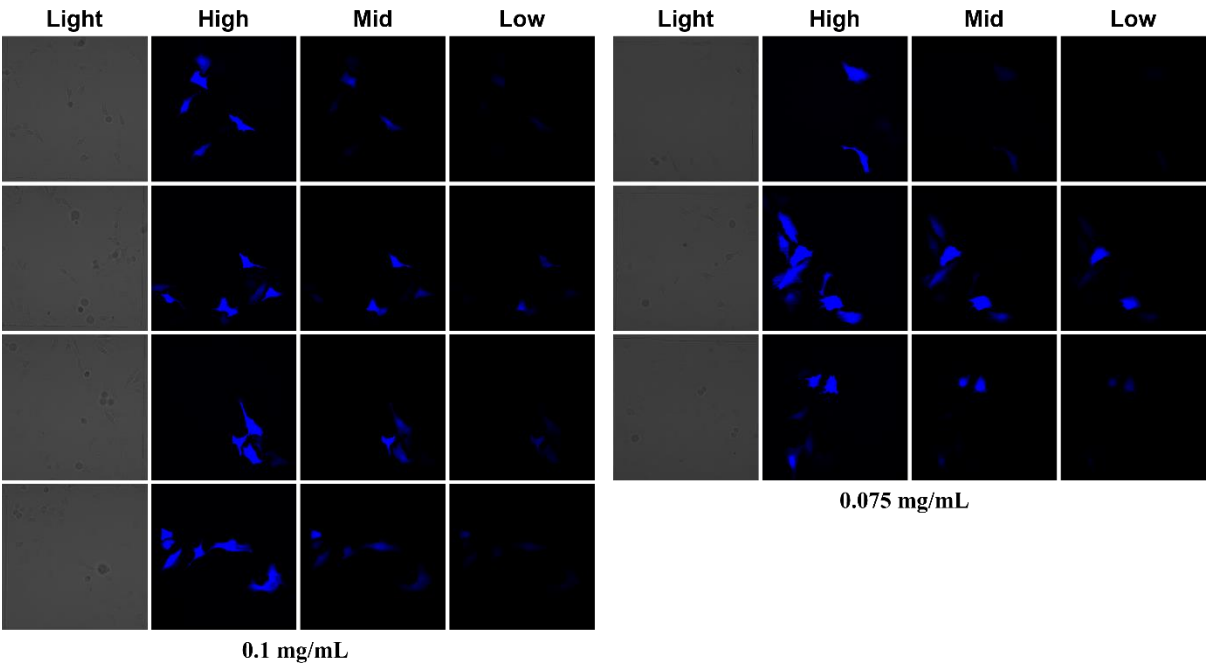
### 2.3.5 Calcein injection calibration curves

To further verify the hypothesis, we tried to test the limit of detection (LOD) of LSM 880. In brief, if the fluorescent signal of dyes in one cell could be detected, how many dye molecules are needed? Herein, we prepared a series of calcein standard solutions with 0.5, 0.25, 0.1, 0.075, 0.05, 0.025, 0.01, 0.0075, 0.005, 0.0025, 0.001, 0.00075, and 0.0005 mg/mL calcein. These calcein solutions were injected to Hela cells via microinjector with 110 hpa injection pressure, 54 holding pressure, and 0.2 s injection time. The injected cells were imaged after 10 min stabilizing. The imaging conditions were divided to high, mid, and low based on the integration time. Under the optical condition  $\lambda_{\text{ex}} = 488 \text{ nm}$  and  $\lambda_{\text{em}} = 493\text{-}556 \text{ nm}$ , master gain 500 and 2.05  $\mu\text{s}$  integration time was used to take low images; master gain 600 and 8.19  $\mu\text{s}$  integration time was used to take mid images; and master gain 800 a, d 65.5  $\mu\text{s}$  integration time and was used to take high images. The images of the calcein solution-injected HeLa cells as shown in [Figure 33](#) to [38](#). After obtaining these images, we further analyzed the fluorescent intensities of calcein in these cells, the results as summarized in [Figure 39](#). At high integration time, the LOD of LSM 880 is 0.0005 mg/mL.

1146 Combining the injection volume we measured and the molecular weight of calcein, the amount of  
 1147 calcein in HeLa cells at LOD concentration was  $5.94 \times 10^{-19}$  or  $16.54 \times 10^{-19}$  mol. The number of  
 1148 nanoflare per cell could calculate by plus the moles with Avogadro constant:  $3.58 \times 10^5$  and  $9.96 \times$   
 1149  $10^5$ .  
 1150



1151  
 1152 **Figure 33.** Images of HeLa cells, which injected by 0.5 mg/mL and 0.25 mg/mL calcein.



1153  
 1154 **Figure 34.** Images of HeLa cells, which injected by 0.1 mg/mL and 0.075 mg/mL calcein.

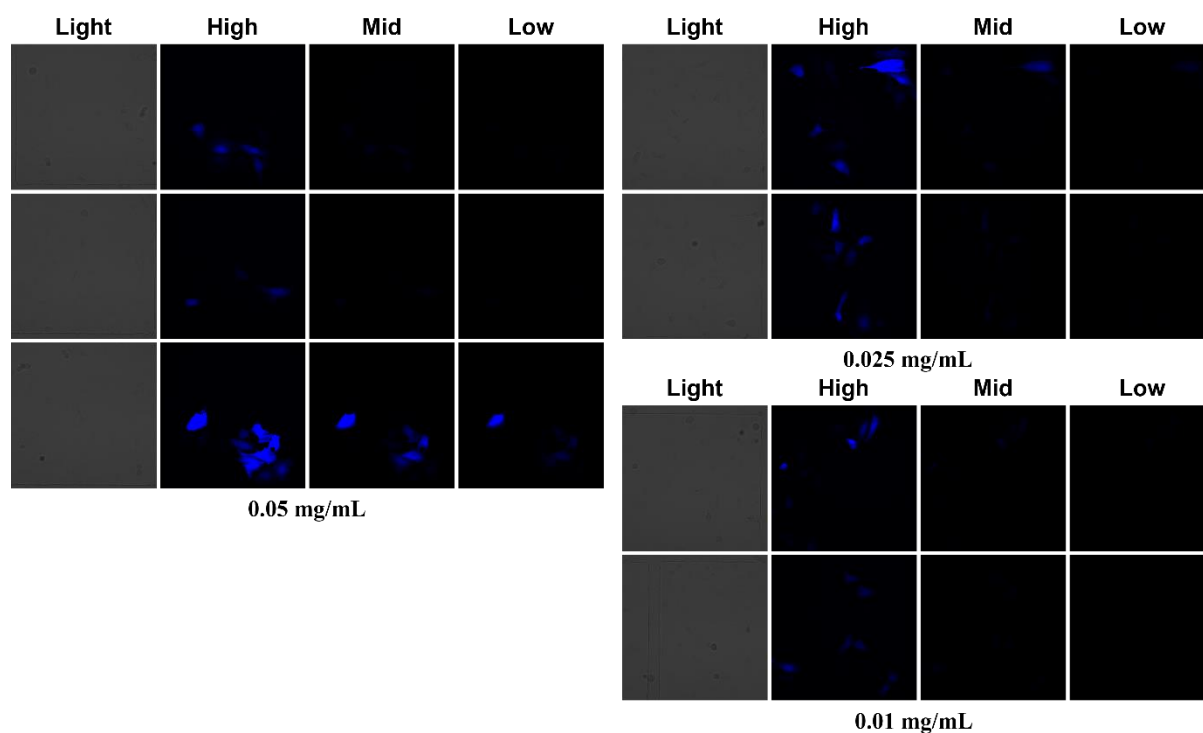


**Figure 35.** Images of HeLa cells, which injected by 0.05 mg/mL, 0.025 and 0.01 mg/mL calcein.

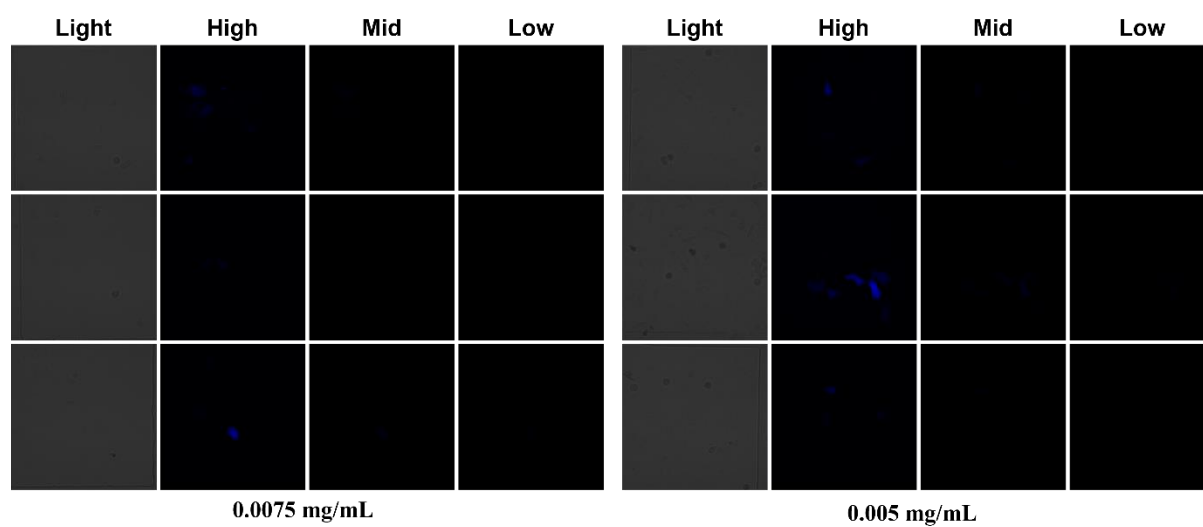


**Figure 36.** Images of HeLa cells, which injected by 0.0075 mg/mL and 0.005 mg/mL calcein.

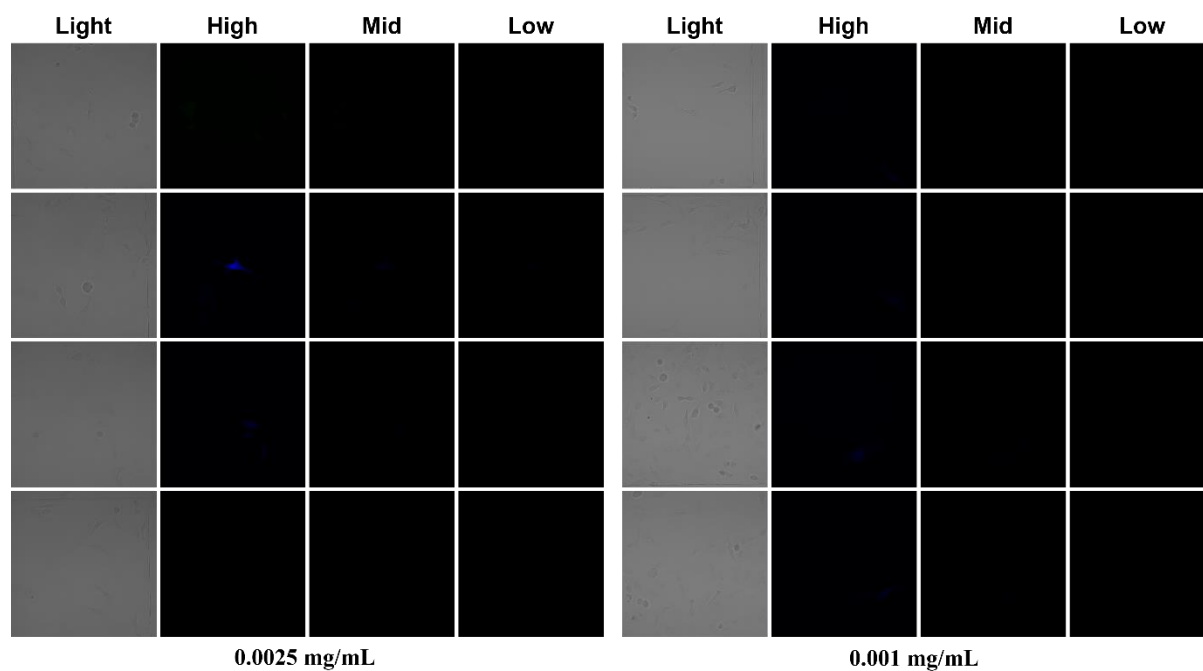


**Figure 37.** Images of HeLa cells, which injected by 0.0025 mg/mL and 0.001 mg/mL calcein.

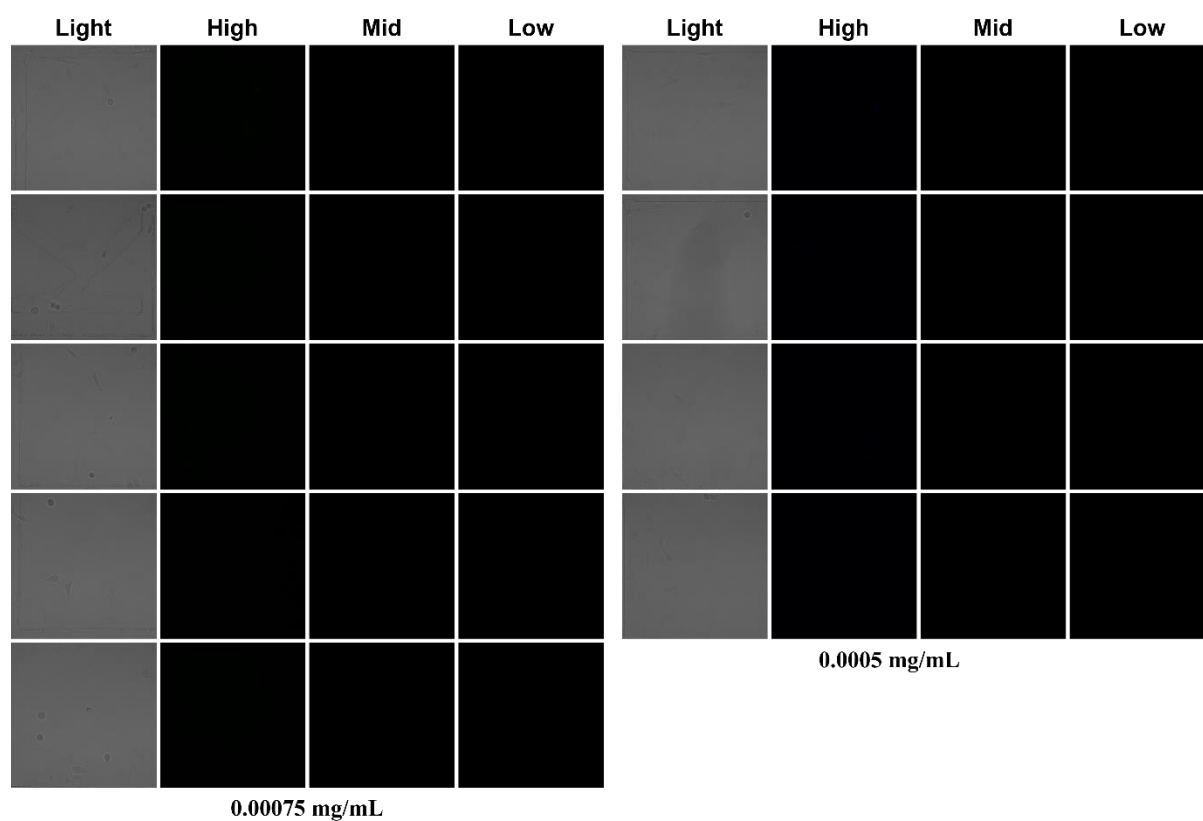


**Figure 38.** Images of HeLa cells, which injected by 0.00075 mg/mL and 0.0005 mg/mL calcein.



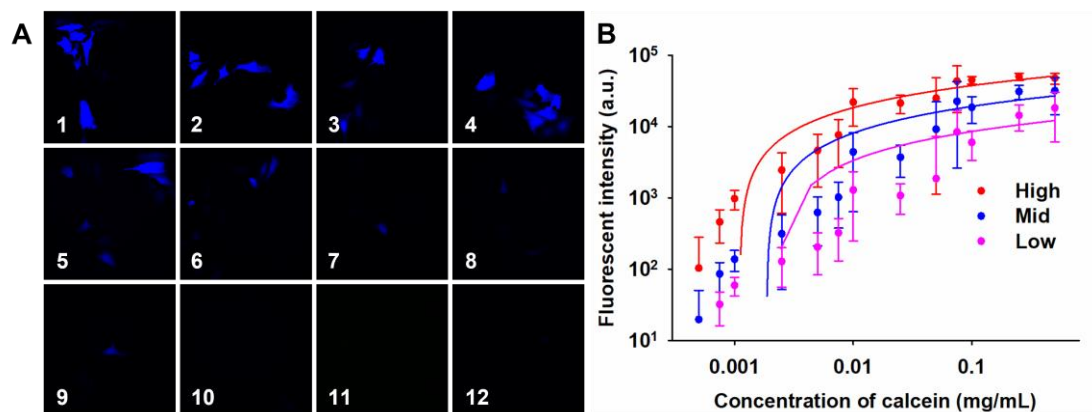


**Figure 39.** Calcein calibration curve. A) Images of calcein standard solutions injected HeLa cells under high imaging integration time. From 1 to 12, the concentrations of calcein are 0.25, 0.1, 0.075, 0.05, 0.025, 0.01, 0.0075, 0.005, 0.0025, 0.001, 0.00075, and 0.0005 mg/mL, respectively. B) The calibration curves of calcein-injected cells. The fluorescent intensity of injected HeLa cell was analyzed by ImageJ, the fluorescent intensity against calcein concentration was used to establish calibration curve. The error bars for the fluorescent intensities of calcein were calculated from 15 cells.

## 2.4 Conclusion

Real-time and in situ mRNA imaging in live cells is key to enhancing the development of drug discovery<sup>[77]</sup>, disease diagnosis<sup>[78]</sup>, cancer therapy<sup>[79]</sup>, and gene engineering<sup>[80]</sup>. Despite a great number of nanosensors having been developed for intracellular mRNA imaging<sup>[81]</sup>, some crucial technique bottlenecks still choke the translation of these nanosensors from lab to market. The central questions that need to be addressed are: increasing understanding of the underlying working mechanisms of nanosensors in cells, increasing the imaging sensitivity without incidental biohazard, and establishing nanosensors for simultaneous imaging of multiple mRNAs in one cell. Foremost among these questions is understanding how nanosensors work inside cells, as this is the basis for accelerating subsequent designing of nanosensors. Among numerous nanosensors, nanoflares have attracted extensive research interest due to their inherent weak cytotoxicity, high endocytosis amount, simple fabrication process, and low preparation cost<sup>[76, 82]</sup>. However, doubts about whether nanoflares can image mRNA in living cells have always existed because nanoflares can not escape endo/lysosome encapsulation theoretically<sup>[72b]</sup>. The relatively high concentration of nucleases in lysosomes raises concerns that nanoflare may non-specific release detection signals leading to false positive results<sup>[83]</sup>. Indeed, cellular internalization of nanoflare could impact the biodistribution of nanoflare in living cells. Inspired by this, we here used microinjection technique to direct inject nanoflare into cytoplasm for avoiding endo/lysosome encapsulation. The results of colocalization imaging revealed that the signals released by endocytosed nanoflares were distributed around cell nucleus and had an obvious overlap with lysosomes. Conversely, the detection signal released by injected nanoflare was more concentrated in cell nucleus and a small part of the signals diffuses outside the cell nucleus. The analysis results of the fluorescence intensity showed that the detection signals released by the endocytosed nanoflares and the injected nanoflares were very close. We also prepared another nanoflare, termed as control nanoflare, the target mRNA for control nanoflare is not present in HeLa cells. The investigation of control nanoflare exhibited that control nanoflare could not release detection signals in HeLa cells whether via microinjection or incubation. Thus, nanoflare worked in HeLa cells, and the released detection signal was not triggered by enzyme degradation. The internalization amount of nanoflare showed that the amount of nanoflare

1201 internalized by endocytosis was higher than the nanoflare internalized by injection, which means  
1202 that the working efficiency of endocytosed nanoflare is far lower than injected nanoflare.  
1203

## **3. The development of Cl<sup>-</sup> microsensor for investigating proton sponge effect**

### **3.1 Introduction**

Owing to their unique physical, chemical, and size properties, micro/nanomaterials have drawn incredible research interest in drug delivery field<sup>[84]</sup>. Generally, micro/nanomaterials construct micro/nanomedicine by encapsulating small molecule therapeutics and achieve the purpose of improved drug delivery through improving drug water solubility and stability and increasing delivery targeting<sup>[85]</sup>. With the development of nanotechnology, micro/nanomedicine as the carrier for therapeutics delivery has allowed to remotely controlled drug release by using micro/nanomaterials responsive to external energy fields and biological microenvironmental factors<sup>[86]</sup>. In the past decades, a large number of micro/nanomedicines have been developed and used for cancer therapy<sup>[87]</sup>. These micro/nanomedicine could enter cancer cells to release therapeutics for killing cancer cells once they accumulated at tumor region<sup>[88]</sup>. The enter pathway recognized as endocytosis, which implies that the endocytosed micro/nanomedicine will be placed at endo/lysosome<sup>[89]</sup>. Although most of these micro/nanomedicines have been designed to respond to acidity or degradable by enzymes, the modest success has forced scientists to continue to find strategies of endosomal escape. Some cationic polymers, especially polyethyleneimine (PEI), were observed to significantly increase gene transfection efficiency and assist nanomedicine to achieve endosomal escape<sup>[90]</sup>. Although the underlying mechanism for this result has not been fully explored, a plausible hypothesis for explaining this has been proposed called proton sponge effect<sup>[91]</sup>.

The proton sponge effect proposes that cationic polymers with buffering capacity inhibit the drop in endosomal pH value during acidification of the endosome, which triggers the continuous work of the proton pump to reach the desired pH value<sup>[92]</sup>. During the operation of the proton pump, a large amount of Cl<sup>-</sup> influx into the endosome at the same time, which causes the osmotic pressure of the endosome to increase and is accompanied by the influx of water. As the influx of Cl<sup>-</sup> and water increases, the internal pressure of the endosome gradually increases leading to the cleavage

of the endosome. Although the proton sponge effect has been used as the standard model for explaining endosome escape in the past few decades, the lack of sufficient correlation between endosome escape efficiency and the pH buffering capacity and molecular weight of cationic polymers greatly limits the application of this model<sup>[93]</sup>. As drug delivery systems with improved pH buffering capacity have been developed over the past decades, however, the results achieved have been very limited, raising doubts about the importance of the pH buffering capacity of cationic polymers for endosomal escape<sup>[93a, 94]</sup>. At the same pH buffering capacity, the molecules of cationic polymers can also affect the endosomal escape efficiency<sup>[95]</sup>. More importantly, a large number of studies have shown that the classic endosome escape aid material PEI can assist the target to achieve endosome escape without co-internalization with the target<sup>[91, 96]</sup>. The inconsistency of the measurement results of lysosomal pH further increased the suspicion of the proton sponge effect.

Although some methods have been used to achieve endosome escape such as membrane fusion, nanoparticle swelling, and membrane destabilization, the mainstream research scheme is still focusing on the proton sponge effect. Therefore, it is very necessary to further reveal the working accuracy and efficiency of the proton sponge effect. Most studies on the proton sponge effect focus on the effect of cationic polymers on endosomal pH value, however, the main factor triggering the increase in endosomal osmotic pressure is the accumulation of Cl<sup>-</sup>. Limited by the complex biological environment of endosomes, cationic polymers may not exhibit real pH buffering capacity in endosomes, which means that the efficiency of endosome escape should be determined by the perturbation of Cl<sup>-</sup> in endosomes. Here we try to construct a microsensor for imaging and detecting endosomal Cl<sup>-</sup> concentration, especially before and after the introduction of PEI. The subject structure of this microsensor is polyelectrolyte capsule, because the inherent hollow structure and semi-permeable properties of polyelectrolyte capsule can minimize the impact on the inner body space and ensure the working efficiency of the sensing unit<sup>[31, 97]</sup>. In addition, PEI as a polyelectrolyte can be easily assembled on the surface of polyelectrolyte capsule<sup>[98]</sup>. The sensing unit here is composed of BSA modified with PCQ. We first synthesized 6-phenyl-N-(6-carboxyhexyl) quinolinium (PCQ) according to a previously reported protocol<sup>[99]</sup>, and coupled it to BSA by a covalent method<sup>[100]</sup>. The extracellular test results showed that PCQ and PCQ@BSA had satisfactory Cl<sup>-</sup> sensing sensitivity. To achieve ratiometric detection, we further modified Cy5 on

1259 BSA, which has only a very weak overlap with PCQ. Nevertheless, in the final test we found that  
1260 PCQ@BSA@Cy5-loaded polyelectrolyte capsules could not detect chloride ions because the  
1261 inherent blue background of polyelectrolyte capsules affected the work of infected PCQ.  
1262

## 3.2 Experimental section

### 3.2.1 Materials

6-phenylquinolinium, 6-bromohexanoic acid, polystyrene sodium sulfonate (PSS,  $M_w$ : 70000), polyallylamine hydrochloride (PAH,  $M_w$ : 15000), bovine serum albumin (BSA), 1-Ethyl-3-(3-dimethylaminopropyl) carbodiimid•hydrochlorid (EDC•HCl), ethylenediaminetetraacetic acid•2Na (EDTA•2Na),  $\text{NaH}_2\text{PO}_4\cdot\text{H}_2\text{O}$ ,  $\text{Na}_2\text{HPO}_4\cdot\text{H}_2\text{O}$ ,  $\text{CaCl}_2$ ,  $\text{Na}_2\text{CO}_3$ , acetone, and methanol were purchased from Sigma Aldrich. Cy5 carboxylic acid was purchased from Lumiprobe Limited (Asia&Pacific).

### 3.2.1 Preparation of PCQ

The PCQ ( $\text{C}_{21}\text{H}_{17}\text{O}_2\text{N}$ ) was synthesized according to a previously reported method<sup>[99]</sup>. In brief, 2.05 g of 6-phenylquinolinium and 2.34 g of 6-bromohexanoic acid were mixed and heated to 110 °C for 4 hours. The obtained solid was washed with acetone for four times. Subsequently, the washed solid was recrystallized at methanol. The PCQ was collected by centrifugation (5000 rpm/10 min). The extra methanol was removed by vacuum drying. The prepared PCQ was stored at dark condition for further use. The reaction equation as shown in [Figure 40](#).

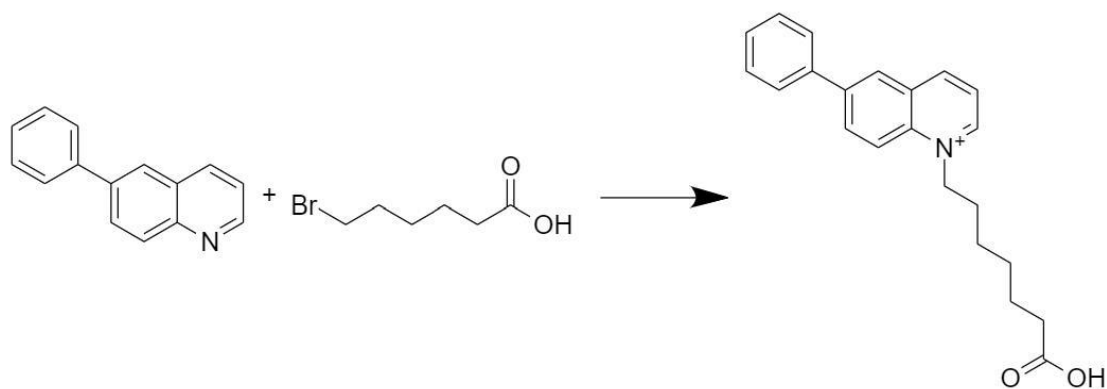


**Figure 40.** The reaction equation of the preparation of PCQ.

### 3.2.2 Preparation of PCQ-conjugated BSA and Cy5-conjugated BSA

PCQ-conjugated BSA were obtained by coupling the carboxyl of PCQ with amino group of BSA through active ester method<sup>[101]</sup>. The conjugation ratio of PCQ and BSA was 10 PCQ : 1 BSA. Briefly, 0.315 mg of PCQ was dissolved into 500  $\mu$ L of Milli-Q water and then 1 mg of EDC•HCl was dissolved into 500  $\mu$ L of Milli-Q water, the mole ratio of EDC•HCl and PCQ was 5 EDC•HCl : 1 PCQ. Subsequently, the PCQ and EDC solutions were mixed at flask and reacted under 600 rpm stirring for 15 min. Afterward, 1 mL of 66 mg/mL BSA solution was dropwise added to the mixture of PCQ and EDC with gentle stirring and reacted at room temperature for another 2 h. The obtained PCQ@BSA was purified with three days dialysis. The final concentration of PCQ@BSA solution was assumed 33 mg/mL. The conjugation of cy5 and BSA were through a similarly process of the synthesis of PCQ@BSA. The conjugation ratio of cy5 and BSA was 10 cy5 : 1 BSA.

### 3.2.3 Preparation of PCQ@BSA and Cy5@BSA co-loaded PCs

PCQ@BSA and Cy5@BSA co-loaded PCs was synthesized by coprecipitation method<sup>[102]</sup>. Firstly, PCQ@BSA-loaded 4.5-5.0  $\mu$ m spherical porous CaCO<sub>3</sub> cores were synthesized according to a previously reported method. 20  $\mu$ L of 10 mg/mL PCQ@BSA and 20  $\mu$ L of 10 mg/mL Cy5@BSA were added to 630  $\mu$ L of 0.33 M CaCl<sub>2</sub>•2H<sub>2</sub>O solution with stirring for 2 min. Then, 630  $\mu$ L of 0.33 M Na<sub>2</sub>CO<sub>3</sub> solution was rapidly added to the solution with 1000 rpm for 30 s. After 30 s stirring, stop the stirring and remained the mixture at undisturbed for 90 s. The cores were collected by 3000 rpm centrifugation for 10 s. The cores were washed with Milli-Q water three times to remove extra CaCl<sub>2</sub>, Na<sub>2</sub>CO<sub>3</sub>, unencapsulated PCQ@BSA and Cy5@BSA.

After obtained the CaCO<sub>3</sub> core, 4.5-5.0  $\mu$ m polyelectrolyte capsule was prepared by depositing alternating polyelectrolyte layers of negatively charged PSS and positively charged PAH. The deposition was achieved by a layer-by-layer process. In brief, the prepared CaCO<sub>3</sub> cores were first resuspended in 1 mL of PSS solution (Mw = 70 kDa, 10 mg/mL, 0.05 M NaCl, and pH 6.5), sonicated for 3 min, and shaken for 10 min. And then, the PSS-coated CaCO<sub>3</sub> particles were collected by 3000 rpm centrifugation for 10 s. The collected PSS-coated CaCO<sub>3</sub> particles were washed with Milli-Q water three times. Subsequently, the particles were resuspended in 1 mL of PAH solution (Mw = 56 kDa, 10 mg/mL, 0.05 M NaCl, and pH 6.5), sonicated for 3 min, and shaken



for 10 min. The particles were collected and washed with same processes. The coating of following PSS and PAH was performed by same method. We here coated two layers of PSS and two layers of PAH on  $\text{CaCO}_3$  cores.

To remove the  $\text{CaCO}_3$  core, the collected particles were suspended in 1 mL of 0.2 M EDTA•2Na aqueous solution. The hollow PCs were centrifuged at 3000 rpm for 5 min and the supernatant was removed. 1 mL of Milli-Q water was added to wash the collected hollow PCs. The washing steps was repeated three times. The prepared PCQ@BSA and Cy5@BSA co-loaded PCs were suspended in pH 6.0 PB and stored at 4 °C for further use.

### 3.3 Results and discussion

#### 3.3.1 Synthesis and characterization of PCQ

Owing to the specific acidic environment in endo/lysosome, the fluorescent dye used for sensing endo/lysosome  $\text{Cl}^-$  is required to be insensitive to pH variation<sup>[103]</sup>. Therefore, we first evaluated pH impact on the fluorescent signal of the PCQ by measuring the fluorescent intensities of PCQ in different pH value PB. The concentration of PB is 0.01 M, the pH value of PB from 5.0 to 8.0 were adjusted according to the buffer reference center published in Sigma-Aldrich. The pH 2.6, 3.0, and 4.0 PBs were prepared by using 0.01 M  $\text{HNO}_3$  to adjust pH value of pH 5.0 PB. After prepared the PBs, 10  $\mu\text{L}$  of 1 mg/mL PCQ solutions were respectively added to the PBs to prepare 10  $\mu\text{g/mL}$  PCQ solution. After 10 min stabilizing, the fluorescent spectra of these PCQ solutions were recorded by Fluorolog-3 (Jobin Yvon Inc.). The results are summarized in Figure 41. The results suggested that there have no fluorescent signal could be detected when PCQ dissolved in PB with pH 2.6, 3.0, 4.0, and 5.0. The fluorescent intensity of PCQ obviously decreased when the pH value reach to 9.0. Subsequently, we tested the  $\text{Cl}^-$  sensing ability of the prepared PCQ. We first prepared a variety of NaCl standard solutions via pH 6.0 PB. And then, 2  $\mu\text{L}$  of 1 mg/mL PCQ solutions was added to 1 mL of NaCl standard solution. After 15 min stabilizing, the emissions of these mixed solutions were recorded. The results as shown in Figure 42, the fluorescent intensity of PCQ decreased with the increase of the concentration of NaCl. There had obviously fluorescent intensity changes between 0 mM and 1 mM NaCl, which suggested the prepared PCQ is sensitive to detect  $\text{Cl}^-$  in PB.

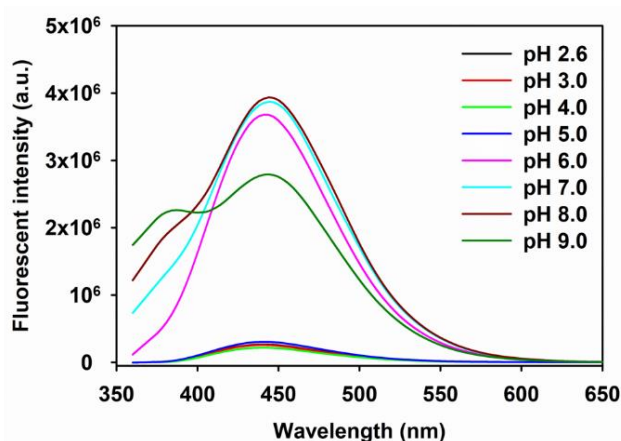


**Figure 41.** Fluorescence spectra of 10  $\mu\text{g/mL}$  PCQ solution at different pH PB. The excitation was 380 nm. This image was recorded by Robbert Schütt.

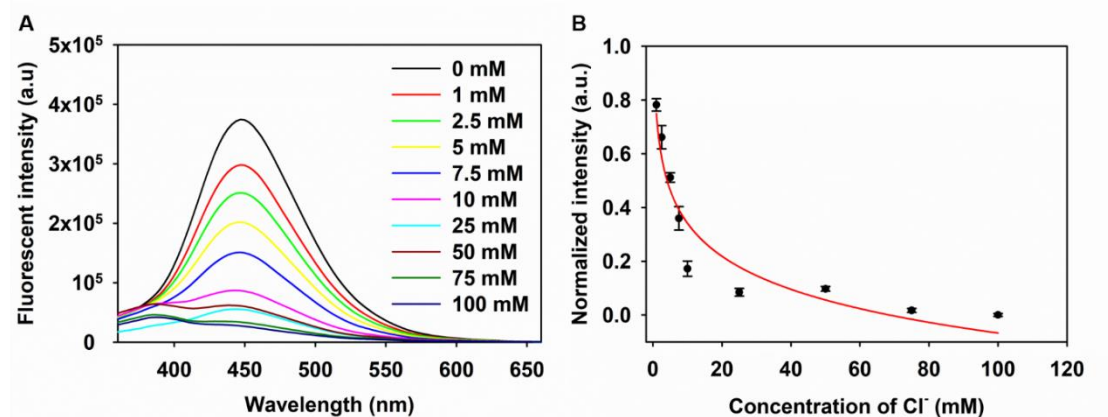


**Figure 42.** A) Under 380 excitation, the fluorescent spectra of 2  $\mu\text{g/mL}$  PCQ solution in different NaCl concentration PB. B) Calibration curve of fluorescent intensity of PCQ against the concentration of NaCl. The emission of PCQ at 450 nm was selected as the fluorescent intensity value. The error bars were calculated from three repetitions. This image was recorded by Robbert Schütt.

### 3.3.2 Synthesis and characterization of PCQ@BSA

We assumed that the the carboxyl of PCQ impacts the solubility of PCQ in acidic environment and thus affect the fluorescent intensity of PCQ in acidic environment. This effect maybe weaken after the coupling with BSA. Thus, after obtaining the PCQ@BSA, we then evaluated the pH influence on the fluorescent intensity of the PCQ@BSA. In the test, 10  $\mu\text{L}$  of PCQ@BSA (6 mg/mL) was respective added to the PB with different pH value. Afterward, recorded the fluorescent spectra of these diluted PCQ@BSA solution (Figure 43). As we hypothesized, the acidic influence on PCQ is weakened after conjugating PCQ with BSA. Therefore, we further examined the  $\text{Cl}^-$  performance of the prepared PCQ@BSA. As same as above mentioned method, 2  $\mu\text{L}$  of PCQ@BSA (6 mg/mL) was respective added to PB solutions with different concentrations of NaCl. The results in Figure 44 suggested that the prepared PCQ@BSA could be used for the detection of  $\text{Cl}^-$  in PB.

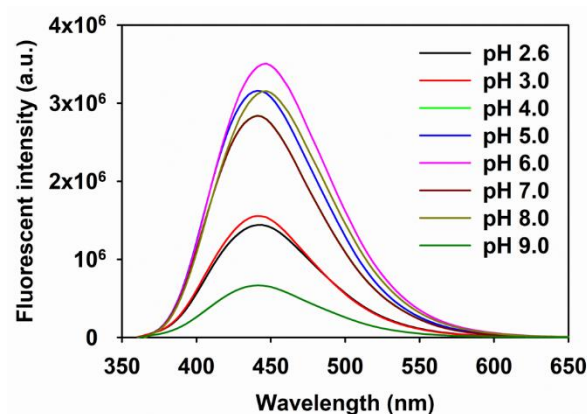


**Figure 43.** 10  $\mu\text{L}$  of PCQ@BSA solutions (6 mg/mL) were respective added to PB solutions with different pH values. The fluorescent spectra was recorded under the 380 nm excitation. This image was recorded by Robbert Schütt

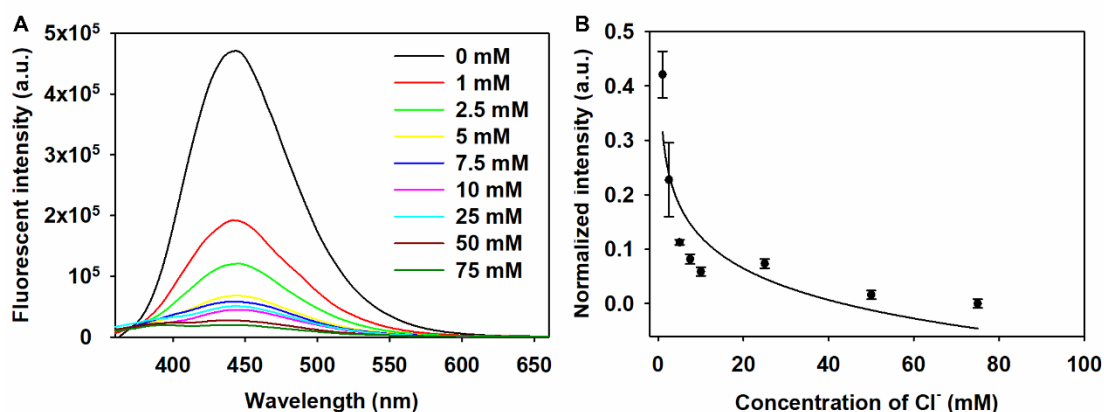


**Figure 44.** For the sensing ability testing, 2  $\mu\text{L}$  of 6 mg/mL PCQ-BSA solutions were respective added to 1 mL of NaCl standard solutions. A) Under 380 nm excitation, the fluorescent spectra of the mixture was recorded. B) is the calibration curve for the detection of  $\text{Cl}^-$  using the PCQ@BSA. The fluorescent intensity is the emission of PCQ@BSA at 450 nm. This image was recorded by Robbert Schütt.

### 3.3.3 $\text{Cl}^-$ sensibility examination of Cy5

We here plan to develop a microsensor for detecting  $\text{Cl}^-$  in endo/lysosome. In order to increase the detection accuracy, we introduced Cy5 as a reference fluorochrome in this microsensor for ratiometric sensing. As the premise, we first need to ensure that the fluorescent signal of Cy5 is not

sensitive to  $\text{Cl}^-$ . therefore, we prepared Cy5-conjugated BSA (Cy5@BSA), and the fluorescent spectra of Cy5@BSA in PB (0.01 M, pH 6.0) and Cy5@BSA in PBS (0.01 M, pH 6.0, 200 mM NaCl) were recorded (Figure 45). The results in Figure 45 implied that the prepared Cy5@BSA is unsensitive to NaCl and thus could be used as the reference dye for ratiometric sensing.

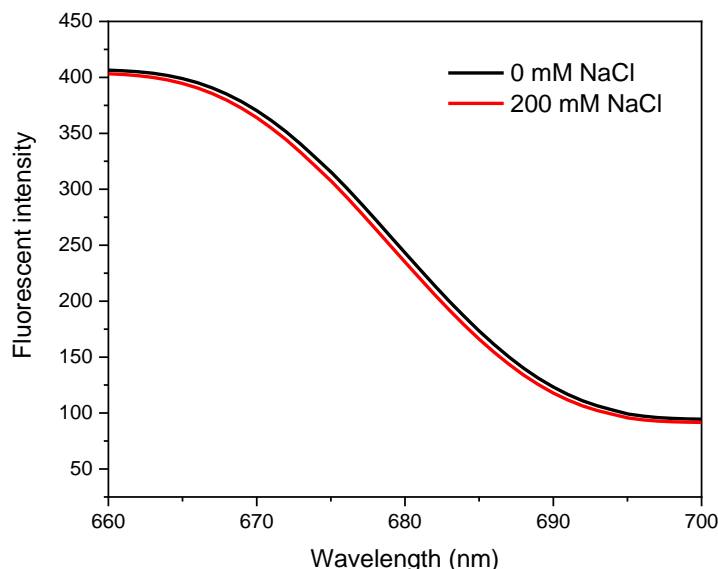


**Figure 45.** Fluorescent spectrums of Cy5@BSA at PB solutions. The black line is the spectrum of 5  $\mu\text{g/mL}$  Cy5@BSA in pH 6.0 PB. The red line is the spectrum of 5  $\mu\text{g/mL}$  Cy5@BSA in pH 6.0 PB with 200 mM NaCl.

### 3.3.4 Preparation and characterization of PCQ@BSA and Cy5@BSA co-loaded PCs

After obtained the PCQ@BSA and Cy5@BSA co-loaded PCs, the concentration of the PCs were measured by cell counting method. The concentration of PCs was measured for times. First time, 10  $\mu\text{L}$  of 100-times diluted PCs solution was added into cell counting plate. The amount of PCs in the grids of cell counting plate was counted under common optical microscope (Carl Zeiss, primovert). The concentration of first time measurement recorded as  $c_1 = 5.4 \times 10^7/\text{mL}$ . Second time, adding 10  $\mu\text{L}$  of 200-times diluted PCs solution into cell counting plate and counting the number of PCs in the grids. The concentration of second time measurement termed as  $c_2 = 6.6 \times 10^7/\text{mL}$ . For third time, 10  $\mu\text{L}$  of 400-times diluted PCs solution was added to the cell counting plate and calculating the PCs number in the grids. The concentration of the third measurement is  $c_3 = 4.9 \times 10^7/\text{mL}$ . By taking the average, the concentration of PCs was estimated as  $5.6 \times 10^7/\text{mL}$ . The

size, morphology, and fluorescent properties of the prepared PCQ@BSA and Cy5@BSA co-loaded PCs were characterized by ZEISS LSM 880 mit Airyscan. We first prepared the image sample by adding 10  $\mu$ L of PCs stock solution into 3 mL of PB solution (pH 6.0), and the prepared sample solution was moved to a petri dish for imaging. The image conditions were PCQ:  $\lambda_{\text{ex}} = 405$  nm,  $\lambda_{\text{em}} = 410$ -514; Cy5:  $\lambda_{\text{ex}} = 633$  nm,  $\lambda_{\text{em}} = 638$ -755 nm, the master gain was 600. As shown in **Figure 46**, the prepared PCs had a spherical structure and co-loading of PCQ@BSA and Cy5@BSA was successful.

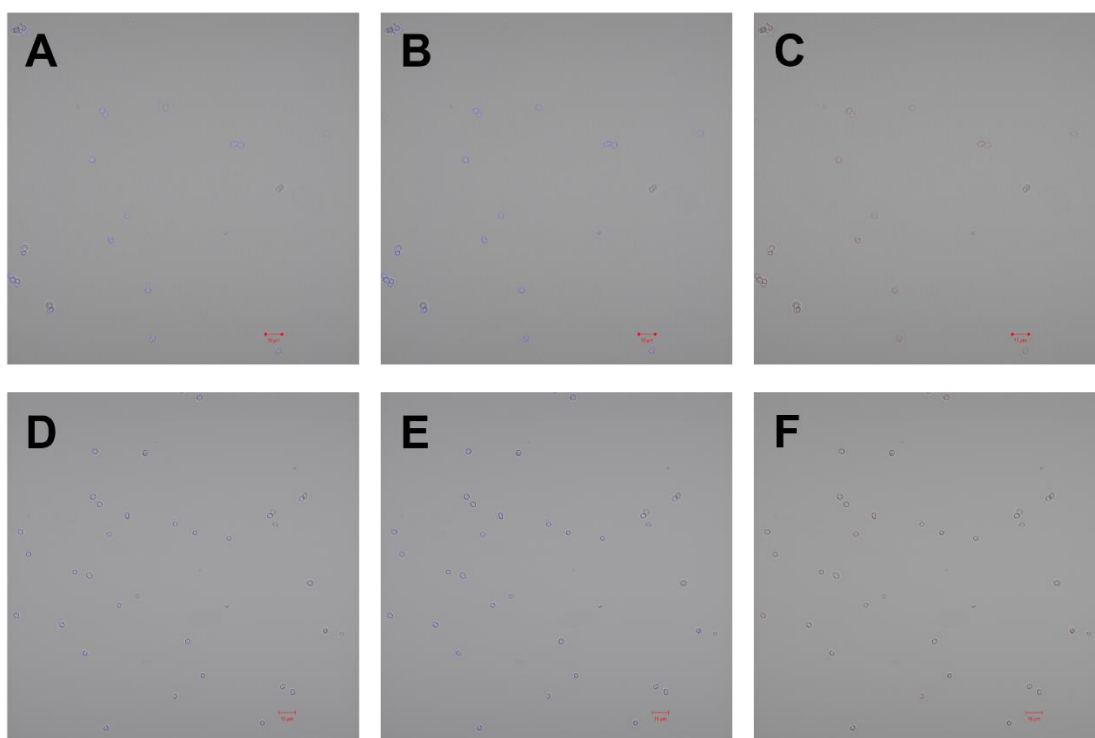
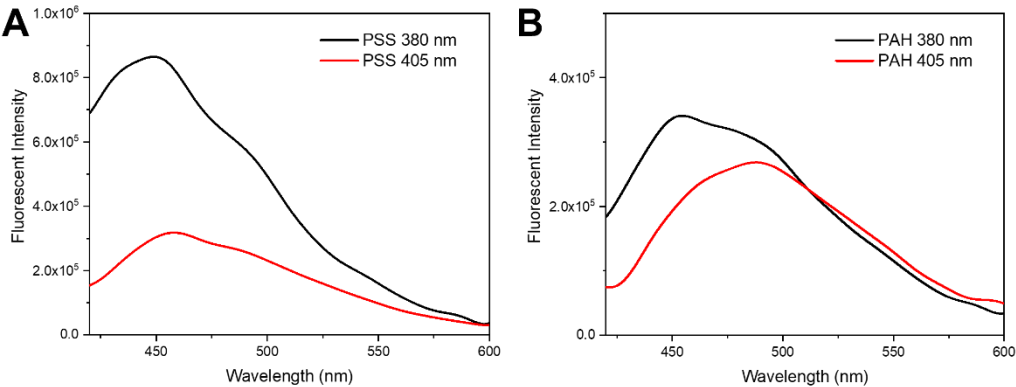


**Figure 46.** Images of the PCQ@BSA and Cy5@BSA co-loaded PCs. Among them, A, B, and C is the batch 1, D, E, and F is the batch 2. A) is the merge of light, PCQ, and Cy5 fields. B) is the merge of light and PCQ fields. C) is the merge of light and Cy5 fields. D) is the merge of light, PCQ, and Cy5 fields, E) is the merge of light and PCQ field. F) is the merge of light and Cy5 fields. This image was recorded by Robbert Schütt.

### 3.3.5 Fluorescent properties of PSS and PAH

By chance, we found that PSS and PAH also have blue fluorescence, which may interfere with the subsequent  $\text{Cl}^-$  detection. We therefore measured the fluorescence spectra of PSS and PAH. 1 mg/mL PSS and PAH solutions were prepared by direct dissolving PSS and PAH power into Milli-

1411 Q water. Under 380 and 405 nm excitation, the fluorescence spectra of PSS and PAH are shown in  
1412 **Figure 47**, which suggested that there have very strong overlaps between PSS, PAH, and PCQ.



1413  
1414 **Figure 47.** Fluorescence spectra of PSS and PAH at excitations used for PCQ excitation (380 nm,  
1415 405 nm). this image was recorded by Robbert Schütt.  
1416

### 1417 **3.4 Conclusion**

1418        In this project, we tried to fabricate a microsensor for sensing  $\text{Cl}^-$ . We adopted PCs as the carrier  
1419 to deliver PCQ@BSA and Cy5@BSA for ratiometric  $\text{Cl}^-$  sensing. However, the design failed to  
1420 detect  $\text{Cl}^-$  due to the blue background fluorescence of PCs.

1421



## Reference

- [1] a)N. F. Silva, J. M. Magalhães, C. Freire, C. Delerue-Matos, *Biosensors and Bioelectronics* **2018**, 99, 667; b)Y. Lin, Q. Zhou, D. Tang, R. Niessner, D. Knopp, *Analytical Chemistry* **2017**, 89, 5637.
- [2] a)B. Liu, J. Zhuang, G. Wei, *Environmental Science: Nano* **2020**, 7, 2195; b)C. Dincer, R. Bruch, E. Costa-Rama, M. T. Fernández-Abedul, A. Merkoçi, A. Manz, G. A. Urban, F. Güder, *Advanced Materials* **2019**, 31, 1806739.
- [3] a)Y. Liu, L. Teng, C. Xu, H.-W. Liu, S. Xu, H. Guo, L. Yuan, X.-B. Zhang, *Chemical science* **2019**, 10, 10931; b)P. Wang, F. Zhou, C. Zhang, S.-Y. Yin, L. Teng, L. Chen, X.-X. Hu, H.-W. Liu, X. Yin, X.-B. Zhang, *Chemical science* **2018**, 9, 8402.
- [4] W.-L. Li, T. Head-Gordon, *ACS central science* **2020**, 7, 72.
- [5] N. Srivastava, A. Mohammad, R. Singh, M. Srivastava, A. Syed, D. B. Pal, A. M. Elgorban, P. Mishra, V. K. Gupta, *Bioresource Technology* **2021**, 342, 126015.
- [6] M. S. Kim, J. Lee, H. S. Kim, A. Cho, K. H. Shim, T. N. Le, S. S. A. An, J. W. Han, M. I. Kim, J. Lee, *Advanced Functional Materials* **2020**, 30, 1905410.
- [7] F. Geu-Flores, N. H. Sherden, V. Courdavault, V. Burlat, W. S. Glenn, C. Wu, E. Nims, Y. Cui, S. E. O'Connor, *Nature* **2012**, 492, 138.
- [8] a)H. Wang, K. Wan, X. Shi, *Advanced materials* **2019**, 31, 1805368; b)D. Jiang, D. Ni, Z. T. Rosenkrans, P. Huang, X. Yan, W. Cai, *Chemical Society Reviews* **2019**, 48, 3683.
- [9] C. Garcia-Galan, Á. Berenguer-Murcia, R. Fernandez-Lafuente, R. C. Rodrigues, *Advanced Synthesis & Catalysis* **2011**, 353, 2885.
- [10] K. A. Mahmoud, K. B. Male, S. Hrapovic, J. H. Luong, *ACS applied materials & interfaces* **2009**, 1, 1383.
- [11] H. Vaghari, H. Jafarizadeh-Malmiri, M. Mohammadlou, A. Berenjian, N. Anarjan, N. Jafari, S. Nasiri, *Biotechnology letters* **2016**, 38, 223.
- [12] W. Feng, P. Ji, *Biotechnology advances* **2011**, 29, 889.
- [13] M. Hasanzadeh, N. Shadjou, M. Eskandani, M. de la Guardia, *TrAC Trends in Analytical Chemistry* **2012**, 40, 106.

- 1450 [14] S. Ramanavicius, A. Ramanavicius, *Nanomaterials* **2021**, 11, 371.
- 1451 [15] M. B. Spano, B. H. Tran, S. Majumdar, G. A. Weiss, *The Journal of organic chemistry* **2020**,  
 1452 85, 8480.
- 1453 [16] A. Erfani, P. Zarrintaj, J. Seaberg, J. D. Ramsey, C. P. Aichele, *Journal of Applied Polymer*  
 1454 *Science* **2021**, 138, 50545.
- 1455 [17] L. Zhou, X. Luo, J. Li, L. Ma, Y. He, Y. Jiang, L. Yin, L. Gao, *Biochemical Engineering Journal*  
 1456 **2019**, 146, 60.
- 1457 [18] B. Thangaraj, P. R. Solomon, *ChemBioEng Reviews* **2019**, 6, 157.
- 1458 [19] M. Li, S. Qiao, Y. Zheng, Y. H. Andaloussi, X. Li, Z. Zhang, A. Li, P. Cheng, S. Ma, Y. Chen,  
 1459 *Journal of the American Chemical Society* **2020**, 142, 6675.
- 1460 [20] a)B. G. De Geest, N. N. Sanders, G. B. Sukhorukov, J. Demeester, S. C. De Smedt, *Chemical*  
 1461 *Society Reviews* **2007**, 36, 636; b)A. G. Skirtach, A. M. Yashchenok, H. Möhwald, *Chemical*  
 1462 *Communications* **2011**, 47, 12736; c)L. Loretta, P. Rivera-Gil, A. Z. Abbasi, M. Ochs, C. Ganas, I.  
 1463 Zins, C. Sönnichsen, W. J. Parak, *Nanoscale* **2010**, 2, 458.
- 1464 [21] A. A. Antipov, D. Shchukin, Y. Fedutik, A. I. Petrov, G. B. Sukhorukov, H. Möhwald, *Colloids*  
 1465 *and surfaces A: physicochemical and engineering aspects* **2003**, 224, 175.
- 1466 [22] D. G. Shchukin, I. L. Radtchenko, G. B. Sukhorukov, *The Journal of Physical Chemistry B*  
 1467 **2003**, 107, 86.
- 1468 [23] G. Sukhorukov, L. Dähne, J. Hartmann, E. Donath, H. Möhwald, *Advanced Materials* **2000**,  
 1469 12, 112.
- 1470 [24] W.-F. Dong, J. K. Ferri, T. Adalsteinsson, M. Schönhoff, G. B. Sukhorukov, H. Möhwald,  
 1471 *Chemistry of materials* **2005**, 17, 2603.
- 1472 [25] L. I. Kazakova, L. I. Shabarchina, S. Anastasova, A. M. Pavlov, P. Vadgama, A. G. Skirtach,  
 1473 G. B. Sukhorukov, *Analytical and bioanalytical chemistry* **2013**, 405, 1559.
- 1474 [26] a)H. Ai, *Advanced drug delivery reviews* **2011**, 63, 772; b)R. Mouras, M. R. Noor, L. Pastorino,  
 1475 E. Bagnoli, A. Mani, E. Durack, A. Antipov, F. D’Autilia, P. Bianchini, A. Diaspro, *ACS omega*  
 1476 **2018**, 3, 6143.
- 1477 [27] P. Rivera-Gil, S. De Koker, B. G. De Geest, W. J. Parak, *Nano letters* **2009**, 9, 4398.
- 1478 [28] T. Mauser, C. Déjugnat, G. B. Sukhorukov, *The Journal of Physical Chemistry B* **2006**, 110,

1479 20246.

1480 [29] R. Cheng, F. Feng, F. Meng, C. Deng, J. Feijen, Z. Zhong, *Journal of controlled release* **2011**,

1481 152, 2.

1482 [30] A. S. Angelatos, B. Radt, F. Caruso, *The Journal of Physical Chemistry B* **2005**, 109, 3071.

1483 [31] P. R. Gil, L. Loretta, A. Muñoz\_Javier, W. J. Parak, *Nano Today* **2008**, 3, 12.

1484 [32] C. Gao, X. Liu, J. Shen, H. Möhwald, *Chemical Communications* **2002**, 1928.

1485 [33] E. W. Stein, D. V. Volodkin, M. J. McShane, G. B. Sukhorukov, *Biomacromolecules* **2006**, 7,

1486 710.

1487 [34] F. Caruso, D. Trau, H. Möhwald, R. Renneberg, *Langmuir* **2000**, 16, 1485.

1488 [35] L. Xu, M. Luo, L. Yang, X. Wei, X. Lin, H. Liu, *Journal of industrial microbiology and*

1489 *biotechnology* **2011**, 38, 1709.

1490 [36] M. Ochs, S. Carregal-Romero, J. Rejman, K. Braeckmans, S. C. De Smedt, W. J. Parak,

1491 *Angewandte Chemie International Edition* **2013**, 52, 695.

1492 [37] P. K. Harimech, R. Hartmann, J. Rejman, P. Del Pino, P. Rivera-Gil, W. J. Parak, *Journal of*

1493 *Materials Chemistry B* **2015**, 3, 2801.

1494 [38] R. R. Costa, J. F. Mano, *Chemical Society Reviews* **2014**, 43, 3453.

1495 [39] C. S. Karamitros, A. M. Yashchenok, H. Möhwald, A. G. Skirtach, M. Konrad,

1496 *Biomacromolecules* **2013**, 14, 4398.

1497 [40] R. Ghan, T. Shutava, A. Patel, V. T. John, Y. Lvov, *Macromolecules* **2004**, 37, 4519.

1498 [41] A. Yu, Y. Wang, E. Barlow, F. Caruso, *Advanced Materials* **2005**, 17, 1737.

1499 [42] O. Shimon, Y. Yan, Y. Wang, F. Caruso, *ACS nano* **2013**, 7, 522.

1500 [43] Y. Zhang, S. Tsitkov, H. Hess, *Nature communications* **2016**, 7, 1.

1501 [44] Y. Shao, H. Duan, S. Zhou, T. Ma, L. Guo, X. Huang, Y. Xiong, *Journal of agricultural and*

1502 *food chemistry* **2019**, 67, 9022.

1503 [45] X. Zan, A. Garapaty, J. A. Champion, *Langmuir* **2015**, 31, 7601.

1504 [46] C. Zhang, X. Wang, M. Hou, X. Li, X. Wu, J. Ge, *ACS applied materials & interfaces* **2017**, 9,

1505 13831.

1506 [47] a)W. Xu, L. Jiao, Y. Wu, L. Hu, W. Gu, C. Zhu, *Advanced Materials* **2021**, 33, 2005172; b)X.

1507 Cai, L. Jiao, H. Yan, Y. Wu, W. Gu, D. Du, Y. Lin, C. Zhu, *Materials Today* **2021**, 44, 211.

1508 [48] a)Y. Chen, M. Yuan, Y. Zhang, S. Liu, X. Yang, K. Wang, J. Liu, *Chemical science* **2020**, 11,  
1509 8617; b)Y. Weng, Z. Song, C.-H. Chen, H. Tan, *Chemical Engineering Journal* **2021**, 425, 131482.  
1510 [49] Y. Xiong, Y. Leng, X. Li, X. Huang, Y. Xiong, *TrAC Trends in Analytical Chemistry* **2020**, 126,  
1511 115861.  
1512 [50] Y. Xiong, K. Pei, Y. Wu, H. Duan, W. Lai, Y. Xiong, *Sensors and Actuators B: Chemical* **2018**,  
1513 267, 320.  
1514 [51] Y. Wu, W. Guo, W. Peng, Q. Zhao, J. Piao, B. Zhang, X. Wu, H. Wang, X. Gong, J. Chang,  
1515 *ACS Applied Materials & Interfaces* **2017**, 9, 9369.  
1516 [52] N. Zhu, Y. Zou, M. Huang, S. Dong, X. Wu, G. Liang, Z. Han, Z. Zhang, *Talanta* **2018**, 186,  
1517 104.  
1518 [53] S. Zhan, H. Fang, J. Fu, W. Lai, Y. Leng, X. Huang, Y. Xiong, *Journal of agricultural and food*  
1519 *chemistry* **2019**, 67, 9104.  
1520 [54] K. R. Maynard, L. Collado-Torres, L. M. Weber, C. Uytingco, B. K. Barry, S. R. Williams, J.  
1521 L. Catallini, M. N. Tran, Z. Besich, M. Tippani, *Nature neuroscience* **2021**, 24, 425.  
1522 [55] H. Y. Kim, F. Li, J. Y. Park, D. Kim, J. H. Park, H. S. Han, J. W. Byun, Y.-S. Lee, J. M. Jeong,  
1523 K. Char, *Biomaterials* **2017**, 121, 144.  
1524 [56] J. Vamathevan, D. Clark, P. Czodrowski, I. Dunham, E. Ferran, G. Lee, B. Li, A. Madabhushi,  
1525 P. Shah, M. Spitzer, *Nature reviews Drug discovery* **2019**, 18, 463.  
1526 [57] K. E. Lindsay, S. M. Bhosle, C. Zurla, J. Beyersdorf, K. A. Rogers, D. Vanover, P. Xiao, M.  
1527 Araínga, L. M. Shirreff, B. Pitard, *Nature biomedical engineering* **2019**, 3, 371.  
1528 [58] a)J. C. Darnell, K. B. Jensen, P. Jin, V. Brown, S. T. Warren, R. B. Darnell, *Cell* **2001**, 107, 489;  
1529 b)H. Wu, D. Becker, H. Krebber, *Cell reports* **2014**, 8, 1630; c)E. Huntzinger, E. Izaurralde, *Nature*  
1530 *Reviews Genetics* **2011**, 12, 99.  
1531 [59] V. P. Mauro, G. M. Edelman, *Proceedings of the National Academy of Sciences* **2002**, 99, 12031.  
1532 [60] a)G. A. Calin, C. M. Croce, *Nature reviews cancer* **2006**, 6, 857; b)S. Maas, S. Patt, M. Schrey,  
1533 A. Rich, *Proceedings of the National Academy of Sciences* **2001**, 98, 14687; c)R. Tenchov, R. Bird,  
1534 A. E. Curtze, Q. Zhou, *ACS nano* **2021**, 15, 16982.  
1535 [61] a)L.-S. Lin, Z.-X. Cong, J.-B. Cao, K.-M. Ke, Q.-L. Peng, J. Gao, H.-H. Yang, G. Liu, X. Chen,  
1536 *ACS nano* **2014**, 8, 3876; b)H.-M. Meng, H. Liu, H. Kuai, R. Peng, L. Mo, X.-B. Zhang, *Chemical*

1537 *Society Reviews* **2016**, 45, 2583.

1538 [62] a)H. M. Choi, J. Y. Chang, L. A. Trinh, J. E. Padilla, S. E. Fraser, N. A. Pierce, *Nature*  
1539 *biotechnology* **2010**, 28, 1208; b)S. Tyagi, *natuRe methods* **2009**, 6, 331; c)A. R. Buxbaum, G.  
1540 Haimovich, R. H. Singer, *Nature reviews Molecular cell biology* **2015**, 16, 95.

1541 [63] D. P. Bratu, B.-J. Cha, M. M. Mhlanga, F. R. Kramer, S. Tyagi, *Proceedings of the National*  
1542 *Academy of Sciences* **2003**, 100, 13308.

1543 [64] a)K. Wang, Z. Tang, C. J. Yang, Y. Kim, X. Fang, W. Li, Y. Wu, C. D. Medley, Z. Cao, J. Li,  
1544 *Angewandte Chemie International Edition* **2009**, 48, 856; b)L. Qiu, C. Wu, M. You, D. Han, T. Chen,  
1545 G. Zhu, J. Jiang, R. Yu, W. Tan, *Journal of the American Chemical Society* **2013**, 135, 12952.

1546 [65] a)Q. Ding, Q. Zhan, X. Zhou, T. Zhang, D. Xing, *Small* **2016**, 12, 5944; b)Y. Ma, G. Mao, W.  
1547 Huang, G. Wu, W. Yin, X. Ji, Z. Deng, Z. Cai, X.-E. Zhang, Z. He, *Journal of the American*  
1548 *Chemical Society* **2019**, 141, 13454.

1549 [66] a)J. Li, J. Wang, S. Liu, N. Xie, K. Quan, Y. Yang, X. Yang, J. Huang, K. Wang, *Angewandte*  
1550 *Chemie* **2020**, 132, 20279; b)J. Shi, M. Zhou, A. Gong, Q. Li, Q. Wu, G. J. Cheng, M. Yang, Y. Sun,  
1551 *Analytical chemistry* **2016**, 88, 1979.

1552 [67] a)S. B. Ebrahimi, D. Samanta, C. A. Mirkin, *Journal of the American Chemical Society* **2020**,  
1553 142, 11343; b)D. Samanta, S. B. Ebrahimi, C. A. Mirkin, *Advanced Materials* **2020**, 32, 1901743.

1554 [68] D. S. Seferos, D. A. Giljohann, H. D. Hill, A. E. Prigodich, C. A. Mirkin, *Journal of the*  
1555 *American Chemical Society* **2007**, 129, 15477.

1556 [69] J. I. Cutler, E. Auyeung, C. A. Mirkin, *Journal of the American Chemical Society* **2012**, 134,  
1557 1376.

1558 [70] X.-J. Yang, K. Zhang, T.-T. Zhang, J.-J. Xu, H.-Y. Chen, *Analytical chemistry* **2017**, 89, 4216.

1559 [71] S. Budik, W. Tschulenck, S. Kummer, I. Walter, C. Aurich, *Reproduction, Fertility and*  
1560 *Development* **2017**, 29, 2157.

1561 [72] a)R. Yan, J. Chen, J. Wang, J. Rao, X. Du, Y. Liu, L. Zhang, L. Qiu, B. Liu, Y. D. Zhao, *Small*  
1562 **2018**, 14, 1802745; b)D. S. Lee, H. Qian, C. Y. Tay, D. T. Leong, *Chemical Society Reviews* **2016**,  
1563 45, 4199.

1564 [73] a)M. Czarnek, J. Bereta, *Scientific reports* **2017**, 7, 1; b)D. Mason, J. Comenge, G. Carolan, S.  
1565 Cowman, *ScienceOpen Research* **2015**.

1566 [74] D. Zhu, H. Yan, Z. Zhou, J. Tang, X. Liu, R. Hartmann, W. J. Parak, N. Feliu, Y. Shen,  
 1567 *Biomaterials science* **2018**, 6, 1800.

1568 [75] a)S. M. Hartig, *Current protocols in molecular biology* **2013**, 102, 14.15. 1; b)E. T. Arena, C.  
 1569 T. Rueden, M. C. Hiner, S. Wang, M. Yuan, K. W. Eliceiri, *Wiley Interdisciplinary Reviews:*  
 1570 *Developmental Biology* **2017**, 6, e260.

1571 [76] Z. Qing, G. Luo, S. Xing, Z. Zou, Y. Lei, J. Liu, R. Yang, *Angewandte Chemie International*  
 1572 *Edition* **2020**, 59, 14044.

1573 [77] Z. Zhuo, Y. Wan, D. Guan, S. Ni, L. Wang, Z. Zhang, J. Liu, C. Liang, Y. Yu, A. Lu, *Advanced*  
 1574 *Science* **2020**, 7, 1903451.

1575 [78] T. Chen, C. S. Wu, E. Jimenez, Z. Zhu, J. G. Dajac, M. You, D. Han, X. Zhang, W. Tan,  
 1576 *Angewandte Chemie International Edition* **2013**, 52, 2012.

1577 [79] S. Yu, Y. Zhou, Y. Sun, S. Wu, T. Xu, Y. C. Chang, S. Bi, L. P. Jiang, J. J. Zhu, *Angewandte*  
 1578 *Chemie* **2021**, 133, 6013.

1579 [80] C. Wu, S. Cansiz, L. Zhang, I.-T. Teng, L. Qiu, J. Li, Y. Liu, C. Zhou, R. Hu, T. Zhang, *Journal*  
 1580 *of the American Chemical Society* **2015**, 137, 4900.

1581 [81] C. Zhang, X. Dong, S. Y. Ong, S. Q. Yao, *Analytical Chemistry* **2021**, 93, 12081.

1582 [82] Y. Yang, J. Huang, X. Yang, K. Quan, H. Wang, L. Ying, N. Xie, M. Ou, K. Wang, *Journal of*  
 1583 *the American Chemical Society* **2015**, 137, 8340.

1584 [83] M.-E. Kyriazi, A. H. El-Sagheer, I. L. Medintz, T. Brown, A. G. Kanaras, *Bioconjugate*  
 1585 *Chemistry* **2022**, 33, 219.

1586 [84] a)V. Biju, *Chemical Society Reviews* **2014**, 43, 744; b)S. Goenka, V. Sant, S. Sant, *Journal of*  
 1587 *Controlled Release* **2014**, 173, 75; c)C. S. Kumar, F. Mohammad, *Advanced drug delivery reviews*  
 1588 **2011**, 63, 789.

1589 [85] a)N. Rabiee, M. Bagherzadeh, A. M. Ghadiri, Y. Fatahi, A. Aldhafer, P. Makvandi, R.  
 1590 Dinarvand, M. Jouyandeh, M. R. Saeb, M. Mozafari, *ACS Applied Bio Materials* **2021**, 4, 5336;  
 1591 b)Q. Hu, P. S. Katti, Z. Gu, *Nanoscale* **2014**, 6, 12273; c)Y. Xu, C. Wang, T. Wu, G. Ran, Q. Song,  
 1592 *ACS Applied Materials & Interfaces* **2022**, 14, 21310.

1593 [86] a)R. Mo, Z. Gu, *Materials Today* **2016**, 19, 274; b)Y. Wang, A. V. Pisapati, X. F. Zhang, X.  
 1594 Cheng, *Advanced healthcare materials* **2021**, 10, 2002196; c)G. Yang, Y. Liu, J. Chen, J. Ding, X.

- Chen, *Accounts of Materials Research* **2022**, 3, 1232.
- [87] a)Z. Liu, J. T. Robinson, S. M. Tabakman, K. Yang, H. Dai, *Materials today* **2011**, 14, 316; b)Y. Zhang, F. Fang, L. Li, J. Zhang, *ACS Biomaterials Science & Engineering* **2020**, 6, 4816.
- [88] a)A. K. Singh, T. P. Yadav, B. Pandey, V. Gupta, S. P. Singh, *Applications of targeted nano drugs and delivery systems* **2019**, 411; b)R. De La Rica, D. Aili, M. M. Stevens, *Advanced drug delivery reviews* **2012**, 64, 967.
- [89] J. J. Rennick, A. P. Johnston, R. G. Parton, *Nature nanotechnology* **2021**, 16, 266.
- [90] a)D. Pei, M. Buyanova, *Bioconjugate chemistry* **2018**, 30, 273; b)T. F. Martens, K. Remaut, J. Demeester, S. C. De Smedt, K. Braeckmans, *Nano Today* **2014**, 9, 344.
- [91] A. Akinc, M. Thomas, A. M. Klibanov, R. Langer, *The Journal of Gene Medicine: A cross-disciplinary journal for research on the science of gene transfer and its clinical applications* **2005**, 7, 657.
- [92] S. A. Smith, L. I. Selby, A. P. Johnston, G. K. Such, *Bioconjugate chemistry* **2018**, 30, 263.
- [93] a)A. M. Funhoff, C. F. van Nostrum, G. A. Koning, N. M. Schuurmans-Nieuwenbroek, D. J. Crommelin, W. E. Hennink, *Biomacromolecules* **2004**, 5, 32; b)A. Ahmad, J. M. Khan, S. Haque, *Biochimie* **2019**, 160, 61; c)F. Richter, L. Martin, K. Leer, E. Moek, F. Hausig, J. C. Brendel, A. Traeger, *Journal of Materials Chemistry B* **2020**, 8, 5026.
- [94] R. V. Benjaminsen, M. A. Matthebjerg, J. R. Henriksen, S. M. Moghimi, T. L. Andresen, *Molecular Therapy* **2013**, 21, 149.
- [95] M. Wojnilowicz, A. Glab, A. Bertucci, F. Caruso, F. Cavalieri, *ACS nano* **2018**, 13, 187.
- [96] L. M. Vermeulen, S. C. De Smedt, K. Remaut, K. Braeckmans, *European Journal of Pharmaceutics and Biopharmaceutics* **2018**, 129, 184.
- [97] M. Schönhoff, *Current opinion in colloid & interface science* **2003**, 8, 86.
- [98] S. Roy, D. Zhu, W. J. Parak, N. Feliu, *ACS nano* **2020**, 14, 8012.
- [99] S. Jayaraman, Y. Song, L. Vetrivel, L. Shankar, A. Verkman, *The Journal of clinical investigation* **2001**, 107, 317.
- [100] Y. Zhou, X. Huang, W. Zhang, Y. Ji, R. Chen, Y. Xiong, *Biosensors and Bioelectronics* **2018**, 102, 9.
- [101] Y. Zhou, S. Xiong, K. Zhang, L. Feng, X. Chen, Y. Wu, X. Huang, Y. Xiong, *Journal of*

1624 *dairy science* **2019**, 102, 3985.

1625 [102] S. Roy, N. M. Elbaz, W. J. Parak, N. Feliu, *ACS Applied Bio Materials* **2019**, 2, 3245.

1626 [103] C. Settembre, A. Fraldi, D. L. Medina, A. Ballabio, *Nature reviews Molecular cell biology*







1627 **2013**, 14, 283.





1628







1629














1630 **List of hazardous substances**

Substance	GHS pictograms	Hazard sentences	Precaution sentences
CaCl <sub>2</sub>	 Warning	H319	P264+P265, P280, P305+P351+P338, and P337+P317
Na <sub>2</sub> CO <sub>3</sub>	 Warning	H319	P264+P265, P280, P305+P351+P338, and P337+P317
Polystyrene sodium sulfonate	 Warning	H332	P261, P271, P304+P340, and P317
Polyallylamine hydrochloride	 Warning	H302 and H317	P261, P264, P270, P272, P280, P301+P317, P302+P352, P321, P330, P333+P313, P362+P364, and P501
Ethylenediaminetetraacetic acid•2Na	  Warning	H302, H312, H315, H319, H332, H335, H373, and H412	P260, P261, P264, P264+P265, P270, P271, P273, P280, P301+P317, P302+P352, P304+P340, P305+P351+P338, P317, P319, P321, P330, P332+P317,

			P337+P317, P362+P364, P403+P233, P405, and P501
H <sub>2</sub> O <sub>2</sub>	   Danger	H271, H302, H314, and H332	P210, P220, P260, P261, P264, P270, P271, P280, P283, P301+P317, P301+P330+P331, P302+P361+P354, P304+P340, P305+P354+P338, P306+P360, P316, P317, P321, P330, P363, P370+P378, P371+P380+P375, P405, P420, and P501
3,3',5,5'- tetramethylbenzidine	 Warning	H302, H315, H319, and H335	P261, P264, P264+P265, P270, P271, P280, P301+P317, P302+P352, P304+P340, P305+P351+P338, P319, P321, P330, P332+P317, P337+P317, P362+P364,

			P403+P233, P405, and P501
Sulfo-NHS-biotin	 Warning 	H302, H312, H315, H319, H332, H335, and H361	P203, P261, P264, P264+P265, P270, P271, P280, P301+P317, P302+P352, P304+P340, P305+P351+P338, P317, P318, P319, P321, P330, P332+P317, P337+P317, P362+P364, P403+P233, P405, and P501
Fluorescein isothiocyanate	 Danger 	H317 and H334	P261, P272, P280, P284, P302+P352, P304+P340, P321, P333+P313, P342+P316, P362+P364, and P501
Na <sub>2</sub> HPO <sub>4</sub> •12H <sub>2</sub> O	 Warning	H319	P264+P265, P280, P305+P351+P338, and P337+P317
NaH <sub>2</sub> PO <sub>4</sub> •2H <sub>2</sub> O	 Warning	H319	P264+P265, P280, P305+P351+P338, and P337+P317

Penicillin	 Danger	H302, H312, H315, H317, H319, H332, H334, and H335	P261, P264, P264+P265, P270, P271, P272, P280, P284, P301+P317, P302+P352, P304+P340, P305+P351+P338, P317, P319, P321, P330, P332+P317, P333+P313, P337+P317, P342+P316, P362+P364, P403+P233, P405, and P501
Streptomycin	 Warning	H351 and H361	P203, P280, P318, P405, and P501
Hoechst 33342	 Warning	H302, H315, H335, and H341	P203, P261, P264, P270, P271, P280, P281, P301+P317, P302+P352, P304+P340, P318, P319, P321, P330, P332+P317, P362+P364, P403+P233, P405, and P501

6-Phenylquinoline	  Danger	H302, H318, and H413	P264, P264+P265, P270, P273, P280, P301+P317, P305+P354+P338, P317, P330, and P501
6-Bromohexanoic acid	 Danger	H314	P260, P264, P280, P301+P330+P331, P302+P361+P354, P304+P340, P305+P354+P338, P316, P321, P363, P405, and P501
EDC•HCl	     Danger	H302, H311, H315, H317, H318, H319, H335, H373, H400, and H410	P260, P261, P264, P264+P265, P270, P271, P272, P273, P280, P301+P317, P302+P352, P304+P340, P305+P351+P338, P305+P354+P338, P316, P317, P319, P321, P330, P332+P317, P333+P313, P337+P317, P361+P364, P362+P364, P391, P403+P233, P405,

			and P501
Cy5 carboxylic acid	Not hazardous substance		
Cy 3	Not hazardous substance		
Cy 5	Not hazardous substance		
Alexa fluor 488	Not hazardous substance		
Lysotracker green	Not hazardous substance		
Glucose	Not hazardous substance		
Dulbecco's Modified Eagles Medium	Not hazardous substance		

1631

1632

## Acknowledgements

Firstly, sincere thanks will be given to China Scholarship Council (CSC). Apparently, I can not live and study in Germany without financial support of CSC.

Secondly, I would like to say thank you very much to Prof. Dr. Wolfgang J. Parak. In the past three and half years, I learned a lot from Wolfgang. In my master, I worked a lot on how to use nanomaterials for establishing high performance nanosensors for the detection of biomarkers. My original Ph.D. plan was to learn how to use nanomaterials for cancer therapy. In this way, combined with the diagnostic technology I learned during my master's degree, my future research direction can be toward the integration of diagnosis and therapy for cancer. This view was completely changed because I knew the importance of fundamental research in Wolfgang's group. During my Ph.D. learning, Wolfgang taught me that although nanomaterials have shown sufficient advantages in tumor diagnosis and treatment, understanding the tumor microenvironment and tumor physiological processes can provide a theoretical basis for designing nanomaterials for diagnosis and treatment of cancer. This not only makes my doctoral research more attractive, but also greatly promotes the development of my future research path. Again, thank you very much, Prof. Dr. Wolfgang J. Parak.

Thirdly, I would like to thank Dr. Neus Feliu. I always remember our first discussion, my English is bad. But, you patiently answered all my questions. Your patience allowed me to bravely use English to discuss with colleagues during my Ph.D. period, which greatly promoted the progress of my doctoral projects. Thank you very much for your guidance, because it let me understand how to study and prepare polyelectrolyte capsule systematically.

Forth, thanks a lot for the data and experimental support of Prof. Dr. Yu Ding and Prof. Dr. Antonios G. Kanaras.

Finally, Thank you very much, Robbert Schuett, thanks for your help in my thesis writing. I also want to show my thanks to Dr. Dingcheng Zhu, Dr. Lili Feng, Dr. Florian Schulz Dr. Huijie Yan, Dr. Yang Liu, Dr. Yanan Kang, Dr. Yuan Zeng, Dr. Lizhen Chen, Dr. Leroy Nack, Dr. Bing Qi, Dr. Gerwin Chilla, Marvin Skiba, Ferdinand Otto, Saad Megahed, Hessam Hosseinkazemi, Miao Feng, Chenxi Yang, Kaiwei Lin, Jili Han, and Marten Rittner.

**Declaration on Oath**

I hereby declare on oath that this doctoral dissertation is written independently and solely by my own based on the original work of my PhD and has not been used other than the acknowledged resources and aids.

Signature: *YaofengZhou*

Date: 06-02-2023